University of Alberta

Patterning Self-Assembled Monolayers on Gold Using a Laser Beam

by

Mohammad Reza Shadnam ©

A thesis submitted to the Faculty of Graduate Studies and Research
in partial fulfillment of the requirements for the degree of

Doctor of Philosophy

Department of Mechanical Engineering

Edmonton, Alberta
Spring 2007

Library and
Archives Canada

Published Heritage
Branch

395 Wellington Street
Ottawa ON K1A 0N4
Canada

Bibliothèque et
Archives Canada

Direction du
Patrimoine de l'édition

395, rue Wellington
Ottawa ON K1A 0N4
Canada

Your file Votre référence
ISBN: 978-0-494-29738-4
Our file Notre référence
ISBN: 978-0-494-29738-4

NOTICE:
The author has granted a non-exclusive license allowing Library and Archives Canada to reproduce, publish, archive, preserve, conserve, communicate to the public by telecommunication or on the Internet, loan, distribute and sell theses worldwide, for commercial or non-commercial purposes, in microform, paper, electronic and/or any other formats.

The author retains copyright ownership and moral rights in this thesis. Neither the thesis nor substantial extracts from it may be printed or otherwise reproduced without the author's permission.

AVIS:
L'auteur a accordé une licence non exclusive permettant à la Bibliothèque et Archives Canada de reproduire, publier, archiver, sauvegarder, conserver, transmettre au public par télécommunication ou par l'Internet, prêter, distribuer et vendre des thèses partout dans le monde, à des fins commerciales ou autres, sur support microforme, papier, électronique et/ou autres formats.

L'auteur conserve la propriété du droit d'auteur et des droits moraux qui protège cette thèse. Ni la thèse ni des extraits substantiels de celle-ci ne doivent être imprimés ou autrement reproduits sans son autorisation.

In compliance with the Canadian Privacy Act some supporting forms may have been removed from this thesis.

While these forms may be included in the document page count, their removal does not represent any loss of content from the thesis.

Conformément à la loi canadienne sur la protection de la vie privée, quelques formulaires secondaires ont été enlevés de cette thèse.

Bien que ces formulaires aient inclus dans la pagination, il n'y aura aucun contenu manquant.

Canada

Abstract

One of the unique properties of self-assembled monolayers (SAMs) is that SAMs can systematically modify certain properties of substrates, e.g. wettability and adhesion, depending on their tail group. Therefore, SAMs have been patterned using several methods. A "Direct Laser Patterning" (DLP) methodology has been developed to manipulate surface wetting properties using a SAM on gold film (alkanethiol type). In DLP a focused Argon laser beam causes the SAM to thermally desorb in desired regions and leave bare substrate behind, which is subsequently backfilled with another alkanethiol of interest through solution deposition. The kinetics of SAM desorption into gaseous media under ambient pressure is also considered using curve fitting of experimentally measured SAM coverage data at different temperatures to the Eyring equation. It was found that the thermal SAM desorption is a 2-step process: a fast regime followed by a slow regime. Activation energy of SAM desorption is calculated to be 30 kcal/mol in air. This information is used in a thermokinetics model, which describes laser induced desorption of SAMs through combining SAM desorption kinetics equation with heat propagation equations in DLP methodology. It was found that contrast plots of experimental scanning electron microscopy (SEM) images, which are correlated to surface coverage of SAMs desorbed after laser irradiation, agreed with the predicted surface composition of SAMs. The surface composition of SAM was then interpreted in terms of the wetting property of the resulting surface. The effect of incident laser beam power and size on final spatial coverage of SAMs on the surface and feature sizes was investigated both experimentally and theoretically. Considering the correlation of the theoretical and experimental results we concluded that the feature sizes are controllable in

a predictable way (using the developed thermal-kinetics model) through varying laser beam power and beam size. It is shown that DLP can be used as a free-hand pattern generating method and is capable of making various types of geometrical patterns including curvilinear paths and various junction types, e.g. cusp angles and crosses. It was found that within the range of parameters in our experiments resulting features are symmetric with respect to centerline of the heating trajectory and there were no broadening of feature size in crosses and near vertices of angles.

ACKNOWLEDGMENT

I am deeply indebted to my supervisor Dr. Alidad Amirfazli for his patience, kind advice and support. I would like to thank Sean Kirkwood, Dr. Robert Fedosejevs, Dr. Larry Kostiuk and Dr. Subir Bhattacharjee for their encouragement and fruitful discussions. I would like to thank Javed Ally for substrate preparation and the design of the Environmental Process Chamber and a special to Dr. David Wilson for providing access to his Argon ion laser during the earlier stages of this work. I thank Andew Luu and Daniel Raso, as well, for assisting me with parts of experiments. This work was supported by the Natural Sciences and Engineering Research Council of Canada (NSERC). I would like to take the opportunity to acknowledge financial support from Alberta Ingenuity, as well.

Table of Contents

Chapter 1- Introduction....1
  Background....1
  Objective and Scope....8
  Proof of Concept Experiments....9
  Modeling of Laser Heating....11
  Chemical Reaction Kinetics....12
  Nonlinear Patterns....14
  References....18
Chapter 2- Direct Patterning of Self Assembled Monolayers on Gold Using a Laser Beam....22
  Introduction....22
  Sample Preparation and Experimental Setup....25
  Patterning Procedure....27
  Experimental Results....28
  Theoretical Formulation....31
    Model Definition....31
    Formulation of the Governing Equation....32
    Definition of Governing Equation Coefficients....36
    Temperature profiles....39
  Results and Discussion....40
    Comparison of Theoretical and Experimental Results....41
    Feasibility of Laser Patterning....44

Summary and Conclusions..47
References..62
Chapter 3- Thermo-Kinetics Study of Laser Induced Desorption of Self Assembled Monolayer from Gold: Case of Laser Micropatterning...66
Introduction..66
Procedure...68
Experimental Results..70
Thermal-Kinetic Model for SAM Desorption...71
Discussion...77
Summary and Conclusions...82
References...97
Chapter 4- Kinetics of Alkanethiol Monolayer Desorption from Gold in Air............100
Introduction..100
Experimental Procedure...100
Results and Discussion...102
Summary and Conclusions..109
References..113
Chapter 5- Using Laser to Fabricate Miniaturized Network of Open Channels: Curvilinear Paths and Various Junction Types...114
Introduction..114
Experimental Procedures and Materials...116
Experimental Results...118
Surface Temperature Profile Induced by the Laser Beam.................................119

Formulation of Thermal Model..........120

Discussion..........126

Summary and Conclusions..........131

References..........147

Chapter 6- Summary, Conclusions and Future Directions..........150

Future Directions and Recommendations..........152

References..........154

Appendix 1- Details of Experimental Methods..........155

Cleaning of Glassware..........155

Sample Preparation..........155

Calibration of Laser Power..........155

Focusing of Laser Beam..........156

Appendix 2-Details of the Thermo-kinetic Model..........158

Maple Code..........158

Appendix 3- Curvilinear Calculations..........161

Maple Code..........161

Appendix 4- Other Experimental Results..........177

Appendix 5- Kinetic Plots..........179

List of Tables

Table 1-1. The properties that can be manipulated on SAM surfaces........................16

Table 1-2. Patterning Techniques for alkanethiol SAMs.......................................17

Table 2-1. The numerical values of the parameters in equations..............................49

Table 3-1. Thermal and process parameters..84

Table A1-1. Power calibration chart...158

List of Figures

Figure 2-1. Schematic of the experimental setup for laser patterning of a surface..........50

Figure 2-2. Patterned and damaged surfaces under microscope..................................51

Figure 2-3. Scaling of replaced monolayer line width with laser power......................52

Figure 2-4. Cartesian coordinate system used to define directions...........................53

Figure 2-5. Thermal conductivity of the available data for soda lime glasses...............54

Figure 2-6. Contour plot of transient temperature constant lines in the X-Y plane.........55

Figure 2-7. Sensitivity of the SAM feature line widths to variations in temperature........56

Figure 2-8. The *e* versus 1-hexadecanethiol SAM removal temperature.......................57

Figure 2-9. Comparison of the experimental results with the theoretical predictions.....58

Figure 2-10. The *e* vs. desorption temperature and conductivity behavior of sample.....59

Figure 2-11. Optimum line width-incident power diagram for +10 cm lens.................60

Figure 2-12. Optimum line width-incident power diagram for +25 cm lens.................61

Figure 3-1. Steps of direct laser patterning procedure...85

Figure 3-2. The SEM image of a scanned sample at different laser powers..................86

Figure 3-3. Contrast plots of SEM image vs. composition of the surface (73 mW).........87

Figure 3-4. Contrast plots of SEM image vs. composition of the surface (49 mW).......88

Figure 3-5. Contrast plots of SEM image vs. composition of the surface (24 mW).......89

Figure 3-6. Define the line width at certain fraction of HDT left on the surface..........90

Figure 3-7. Variation of the replaced monolayer line width with laser power.............92

Figure 3-8. Normalized profile of laser beam, temperature, and monolayer desorbed...93

Figure 3-9. Correlation of AES signal with SEM pixel intensities..........................94

Figure 3-10. Correlation of AES signal with SEM pixel intensities........................95

Figure 3-11. Correlation of AES signal with SEM pixel intensities..........................96

Figure 4-1. XPS spectra for S2p and C1s of HDT before and after heating..............110

Figure 4-2. Thermal desorption profiles of HDT SAMs from gold surface...............111

Figure 4-3. A sample of fitted curves to experimental desorption data at 160°C..112

Figure 5-1. Steps of direct laser patterning procedure......................................132

Figure 5-2. Liquid delimited on a hydrophilic pattern (MHA surrounded by HDT)....133

Figure 5-3. Sample holder and micropositioners that control movement of sample....134

Figure 5-4. Schematic of optical setup for DLP system.......................................135

Figure 5-5. Light microscope images of features..136

Figure 5-6. The SEM images of crosses and tee junctions....................................137

Figure 5-7. The SEM image of a cusp angle written with a 18 mW laser beam..........138

Figure 5-8. SEM images of circle features...139

Figure 5-9. SEM image of the letters "U of A" patterned on HAD background..........140

Figure 5-10. Heating on a circular curve..141

Figure 5-11 Variation of $w_{80\%}$ due to scanning laser beam moving on a circular-arc...142

Figure 5-12. The effect of heating trajectory curvature, and speed of moving heat source..143

Figure 5-13. Peak surface temperature versus radius of curvature of heating trajectory..144

Figure 5-14. Variation of maximum surface temperature with scanning speed..........145

Figure 5-15. Temporal temperature profile induced at centerline of heating.............146

Figure A1-1. Power calibration setup..159

Figure A1-2. Focusing setup..160

Figure A4-1. Liquid confinement on patterned surface 177

Figure A5-1. Semilogarithmic plots of thermal desorption of HDT 181

Figure A5-2. Desorption of HDT as inverse of coverage versus time 183

List of Acronyms and Symbols

CW	Continuous wave
DLP	Direct laser patterning
EPC	Environmental Process Chamber
HDT	1-hexadecanethiol
MEMS	Microelectromechanical Systems
MHA	16-mercaptohexadecanoic acid
PDE	Partial differential equation
SAM	Self-assembled monolayer
SEM	Scanning electron microscope
UV	ultraviolet
XPS	X-ray photoelectron spectroscopy
ΔG	Gibbs activation free energy
Θ	Linearized temperature change
α	Angular component of observation point
κ	Thermal conductivity
κ_0	Thermal conductivity at T_0
ρ	Radial component of observation point
A	Optical absorption
C	Surface coverage of SAM
C_0	Initial SAM coverage on surface
D	Thermal diffusivity
G	Green’s function

P	Laser power
Q	Heat source function
R	Gas universal constant
T	Temperature
T_0	Initial temperature
e	Sum of absolute values of the difference between the experimental and theoretical laser incident powers at constant line width value
h	Plank's Constant
k	Rate constant
k_0	Conductivity at 298 K
k_1	Slope of linear increase of conductivity with temperature
k_B	Boltzmann's constant
r	Radius in spherical coordinates
t	Time
t_c	Transition time
v	Speed of sample movement
w	Angular speed
w_0	2 e-folding intensity radius of the laser beam
$w_{80\%}$	width of the area that experiences temperatures equal or higher than 80% of the peak temperature
x	Spatial coordinate in the direction of laser movement
y	Spatial coordinate on the surface perpendicular to the direction of laser movement

z	Spatial coordinates perpendicular to the surface
$\underline{x}(t), \underline{y}(t)$	Parametric equations defining trajectory on surface

Chapter 1- Introduction

Background

The ability to engineer surface properties (e.g. wettability, adhesion) at micoscopic scale is the key in the emerging technologically important areas such as bio-sensors, tissue engineering, microelectromechanical systems (MEMS), and controlled delivery of liquids in microfluidics. The ability to control/define surface properties is also important to fundamental studies in surface sciences and physics (e.g. wetting). Alkanethiols ($HS(CH_2)_nX$) provide a means to engineer surface properties. Alkanethiols chemisorb on some metallic surfaces, e.g. gold, silver and copper, through metal-sulfur bonds, spontaneously, through the following reversible chemical reaction:

$$M + HS(CH_2)_nX = M\text{-} S(CH_2)_nX + \tfrac{1}{2} H_2 \qquad M = \text{Au, Ag, Cu, etc.}$$

The alkanethiols make a very stable well-packed one-molecular layer called self-assembled monolayer (SAM) on gold, and based on their end groups (X) can show various surface characteristics. For example, a methyl end group ($X=CH_3$) shows hydrophobic properties and a carboxylic acid end group ($X=COOH$) shows hydrophilic properties. The packed and crystalline structure of SAMs can mask certain properties of the substrate, e.g. biocompatibility, wettability and adhesion.[1,2] Thus, the SAMs provide a means to systematically modify surface properties.

Often for technological reasons a surface is required to have different properties at neighboring regions, e.g. wettability, adhesion and different chemical functionalities. Such a surface is called a patterned surface. Using patterned SAM surfaces a broad range of surface properties can be modulated. The properties of SAM coated surfaces that can be systematically altered are presented in Table 1-1.

There exists several ways for "patterning" a SAM surface (see Table 1-2). Examples of SAM patterning technologies include micro-machining, photolithography, microcontact elastomeric stamping, dip-pen writing, nanoshaving, e-beam lithography procedures, and ion beam lithography (see recent reviews in refs [3,4] for a complete account). The SAM patterning methods can be categorized into pparallel and sequential techniques. In parallel techniques the whole pattern or a large part of it is made at once. Parallel techniques are good for fast processing of large areas and mass production, but require a master of the desired pattern, e.g. a mask or stamp. Examples of parallel techniques are standard photolithographic techniques and micro contact printing. In contrast, in sequential techniques, such as e-beam lithography, patterns are made one after the other. Sequential techniques are more flexible and are particularly useful where patterns of various shapes are required, e.g. in R&D prototyping, mask fabrication or research. However, all of these techniques with the exception of micro-machining and dip-pen writing directly or indirectly use lithography (e.g. for making masters). Multiple lithographic steps entail problems associated with multiple mask alignments and loss of biological activity where bioactive agents are involved.[5] Micro-machining has very limited application as it damages the substrate.[6] The only method that do not have multiple lithography steps is dip-pen lithography, which is a slow method for creating miniaturized patterns (~10 nm) on small areas (<mm^2) serially.[4] There is a need for an alternative fast method for patterning larger areas, which is the aim of this research.

Self-assembled monolayers on gold are easy to prepare, stable, densely packed, extensively characterized and studied, and available with different terminal groups.[7] As such, in this thesis we have focused our studies on SAMs over gold substrate.

It is known that elevated temperature causes the thiolate sulfur-gold bond to become unstable.[10] So, it is perceived that localized heating of the SAM surface can breakup the sulfur-gold bond and produce bare regions of gold through thermal desorption. These bare gold regions can be covered with a second alkanethiol with a different terminal group (X) and/or chain length through solution deposition to alter surface properties in those regions. A laser beam is a means for precise localized heating. An argon laser is used to produce bare gold regions. The desired pattern can be formed by the relative movement of laser beam and the sample. The present thesis has examined this idea in practice.

As result, a promising and economical alternative for SAM patterning using CW argon laser, the so-called Direct Laser Patterning (DLP), has been developed. The DLP works on the principle that focused laser beams is scanned on the surface of an initial SAM and through thermal desorption creates bare regions in the wake of the scanned beam. The bare regions are then backfilled by solution deposition with a second type of SAM species. This procedure can be repeated to place more SAM species on the surface. Thus, DLP is capable of patterning several terminal groups on a single substrate. The DLP approach is unique in that it eliminates the need for photolithography (which requires at least 18 processing steps as mentioned in ref [11]) and does not require clean room or AFM facilities. It is non-contact, and can be extended to other systems such as SAMs on silicon wafers. The DLP can be used freehand to make curvilinear features and various junction types. [12] Patterns down to 4 μm can be fabricated using DLP with CW argon laser; [13] and last minute changes can be introduced without a major difficulty; it is capable of being implemented in high-speed manufacturing and benefits from simplicity and low cost. The latter three points are the advantages of direct laser patterning over the dip-pen writing method; when it is used to produce features of the order of 4 μm or larger.

The idea of direct use of laser for patterning in ambient conditions has recently been extended to SAMs on silicon substrate, as well.[14,15] The 514 nm line of an argon laser has been used to prepare hydrophilic/hydrophobic patterns with feature sizes close to 0.1 μm.[15] The procedure has the same advantages that DLP have over alternatives, e.g. simplicity.

In order to make a mathematical model to predict resulting feature sizes, surface temperature field induced by the laser beam should be determined. It is shown that when the laser pulse duration is much longer than the electron-phonon thermal relaxation time, which is on the order of picoseconds, the laser heating can be modeled by the conventional heat diffusion mechanism.[16] When coefficients are constant the heat diffusion equation associated with the moving heat source problem is a linear differential equation and classical solutions are available.[17] When coefficients, such as thermal conductivity and thermal diffusivity, are temperature dependent the nonlinear partial differential equation is nonautonomus and admits no classical integral. Lax[18] showed that the nonlinearity due to the temperature dependence of conductivity in the governing heat conduction equation can be removed by employing the Kirchhoff transformation. This transformation can yield a linear partial differential equation, if the diffusivity is not temperature-dependent (since conductivity and diffusivity are interrelated through heat capacity and density of material, it means heat capacity times density should be temperature dependent). In this study, it was shown that the temperature dependence of the sample thermal diffusivity could be neglected for our set of experimental parameters. Then, the Kirchhoff transformation was used to linearize the heat diffusion equation. In this research, the calculations are based on the Moody and Hendel[19] steady-state solution of heat diffusion equation in the moving coordinate system, which uses the same transformation. The Ferrieu and Auvert[20] transient solution was also used for comparison and verification of the results. Both of the references formulated the resulting temperature profile using Green functions for the linearized equations.

Fabrication of nonlinear features using laser patterning requires heating on nonlinear trajectories. Thus, the question arises as how and to what extent the geometry of patterns (e.g. curvature of the heating trajectory) may affect the induced temperature profiles and the dependent feature size. Although classical analytical solutions as well as recent numerical solutions exist for the problem of moving heat source along a straight line,[19,21-23] there is no consideration of the heating on more complex geometries (e.g. curvilinear trajectories) in literature. Therefore, study of the effect of heating trajectory curvature, as well as angle and cross pattern geometries on induced temperature field in a substrate is part of this thesis; further, the effect of scanning velocity for trajectories of various curvatures is also considered.

In relation to stability of SAMs at elevated temperatures, it is known that the gold-sulfur bond becomes unstable, if SAM experience elevated temperatures for a suitable time period it will desorb from the gold surface.[24] It is shown that long-chain aliphatic alkanethiol SAMs and ω-substituted alkanethiol SAMs regardless of their origin (either alkanethiol or dithiol) desorb as dimmer molecules from surface.[24,26] Thermal stability and kinetics of SAM desorption in solvents have already been investigated using ellipsometry;[24,27] it is shown that the desorption energetics (e.g. activation desorption energy reported as 28±1 kcal/mol) does not change with chain length and terminal groups, e.g. methyl, carboxylic acid and amide, for chemisorbed alkanethiol SAMs on gold, unless terminal group impose steric hindrance, e.g. aromatic groups.[28,29] Kinetics of SAM desorption in gaseous media under high vacuum is also reported;[30] it is shown that activation energy of desorption is higher than that of liquid media (i.e. 30-35 kcal/mol), which essentially shows the lack of solvatation of resulting species. Kinetics of SAM desorption under atmospheric pressure is not yet reported in literature. Thus, to extract energetics of long chain alkanethiol SAM desorption relevant to DLP,[30] desorption kinetics into gaseous media was needed to be investigated under ambient pressure. The coverage of SAMs in the present study was characterized through X-ray Photoelectron Spectroscopy (XPS), which is better than ellipsometry for quantitative analysis; wetting was also used for observation.

Temperature programmed desorption experiments have shown that energetics of desorption for chemisorbed alkanethiol SAMs changes by less than 0.5 kcal/mol with chain length[28] and terminal groups, e.g. methyl, carboxylic acid and amide.[29]

As part of this research, the kinetics of thermal desorption of SAMs into gaseous media has been experimentally investigated, and a representative mathematical model for the process has been developed.[32] The kinetics results have been used in a thermo-kinetics model to predict size and edge quality of resulting patterns.[33]

The results of these investigations have provided a firm experimental and theoretical basis for DLP.[34]

Objective and Scope

Development of a methodology to manipulate surface wetting properties of a SAM on a gold film using direct laser patterning was the objective of this research. In laser patterning, localized regions of a homogenous SAM surface is desorbed as result of elevated substrate temperature through scanning the focal spot of a continuous wave (CW) laser beam leaving bare regions behind. Then, another SAM (with different characteristics) is let to backfill the bare gold regions through solution deposition. It is intended to produce bare gold regions in the shape of a straight line (in the micrometer range) as well as various shapes that could be of interest in certain applications.

The aim and scope of this research were: (1) providing proof of concept for feasibility of the proposed patterning methodology at the experimental level; (2) modeling of laser heating process to predict the feature size within the proposed methodology at the theoretical level; (3) studying of SAM desorption kinetics and using results in modeling to predict results; (4) providing patterns of various shapes.

Proof of Concept Experiments

Regarding the first objective, development of a methodology to manipulate surface properties of a SAM of alkanethiol on a gold film using direct laser patterning is the discussed in Chapter 2. This chapter demonstrates proof of concept for the feasibility of laser patterning monolayers and outlines theoretical modeling of the process in order to predict the resulting feature size. It has shown that the laser patterning approach is unique in that it eliminates the need for photolithography, is non-contact, and can be extended to other systems. A homogenous SAM made of 1-hexadecanethiol was formed on a 300 Å sputtered film of gold (supported by a soda lime glass substrate through a 50 Å Titanium adhesion layer). The SAM on localized regions were desorbed by scanning the focal spot of a CW argon laser (488 nm) under 97% pure nitrogen atmosphere. The laser was used in TEM_{00} mode and the sample was moved at constant speed of 200 μm/s relative to the stationary laser beam to make straight-line features. The desorption occurred as result of high local substrate temperature produced by the moving laser beam with a Gaussian spatial profile. The last step was immersion of the completely processed sample in the 1mM ethanolic solution of 16-mercaptohexadecanoic acid. In this way, a hydrophilic pattern on a hydrophobic background was made. The resultant lines were viewed and line widths were measured using both wetting with tridecane under light microscope and SEM. The contrast in SEM pictures indicated presence of different SAMs. A Capillary fingering effect (as result of competition between the evaporation and capillary effect) was also observed under an optical microscope when ethanol drops was placed on the surface of the sample (before and after backfilling with the hydrophilic monolayer) that further showed the existence of different wettability properties on the patterned surface. Using direct laser patterning method, we have produced straight line patterns with widths of 4 to 170 µm. Details of the experimental setup used and the procedure for direct Laser patterning of SAMs are described in Chapter 2.

It was found that the threshold for removal of 1-hexadecanethiol monolayer was 1.9-2.5 kW/cm^2 when a +10-cm lens was used and 1.18-1.22 kW/cm^2 when a +25-cm lens was used. The threshold of damage of the gold substrate was found to be 5.9 kW/cm^2 when a +25-cm lens was used. Patterns of different wettability in the shape of a straight line with widths in the 28 to 170 µm range were made.

For making finer features (< 30 µm) a 10X microscope objective was used to further focus the laser beam (in air). For the 10X objective a safe working range, i.e. range of incident laser powers for which the monolayer would remove while keeping the sample undamaged, was defined. Effect of different incident laser powers was examined and width of the features was measured to establish the incident power-feature size relation. The scope of the laser patterning methodology was extended to curvilinear features, tee junctions and crossings, which are of interest in microfluidics applications.

Modeling of Laser Heating

Control of feature size is important for practical applications. Therefore, the second objective (i.e. modeling of laser heating process to predict the feature size) was to construct a thermal model to predict the line width of the desorbed monolayer. We examined the hypothesis of existence of a temperature threshold controlling the feature size. It was found that this temperature threshold is independent of scanning velocity (within range of our experimental speeds, i.e. 0-200 μm/sec as experienced in producing various patterns). Since the laser was used in CW regime, i.e. the pulse length was physically infinite, the rapid photon-electron and electron-phonon interactions (whose time scale is of the order of picoseconds) do not have to be considered in detail and heat diffusion equation was used as governing equation of the temperature field.

The diffusion equation in this model was a nonlinear 3-dimensional parabolic partial differential equation (PDE) because of temperature dependence of thermal properties of the sample. The Kirchhoff transformation (proposed by Lax)[18] was used to linearize the heat diffusion equation. In this research, the calculations are based on the Moody and Hendel[19] steady-state solution of heat diffusion equation in the moving coordinate system, which uses the same transformation. The Ferrieu and Auvert[20] transient solution was also used for comparison and verification of the results. Both of the references formulated the resulting temperature profile using Green functions for the linearized equations.

The effect of the laser power, beam waist was considered. It has been shown that the theoretical predictions are in good agreement with the experimental results and thus the model can effectively be used to predict experimental results.

Laser induced desorption of SAMs from gold surfaces within the context of the DLP methodology was investigated through combining results of a heat diffusion thermal model with desorption kinetics of alkanethiol SAMs in Chapter 3. It was found that contrast plots of experimental SEM images, which is correlated to surface coverage of SAMs desorbed after laser irradiation, agreed with the theoretically predicted surface composition of SAMs. The surface composition of SAM was then interpreted in terms of wetting property of resulting surface. The effect of incident laser beam power and size on final spatial coverage of SAMs on surface and feature sizes was investigated both experimentally and by modeling. Theoretical modeling and experimental evidence showed that the resulting feature sizes are wider when the surface is heated by a laser of higher power; and increasing the laser beam size results in broadening of feature sizes. Considering the correlation of the theoretical and experimental results we concluded that the feature sizes are controllable in a predictable way (using the presented thermal-kinetics model) through varying laser beam power and beam size.

Chemical Reaction Kinetics

The third objective of the present thesis was the study of SAM desorption reaction. The chemical reactions of adsorption, desorption and exchange of SAMs on gold surface are involved in the direct laser patterning of SAMs. Adsorption and exchange at room temperature in solvent medium and desorption at elevated temperatures in gaseous medium are important in this patterning technique. Based on the reported data from literature, we have shown that the favorable chemical reactions involved in the laser patterning procedure are feasible both thermodynamically and kinetically (see Chapter 2).

Thermal stability and kinetics of SAM desorption in solvents have already been investigated using ellipsometry.[24,27] Kinetics of SAM desorption in gaseous media in ambient pressure, which is important for DLP was not discussed in literature; thus we experimentally investigated the kinetics of SAM desorption in gaseous medium in Chapter 4. The SAM was thermally desorbed in an oven of constant temperature for different known times and then the amount of SAM left on surface was examined by X-ray Photoelecton Spectroscopy (XPS). The rates of gas phase thermal desorption of HDT SAM were observed to strongly increase with increase in temperature. Comparison of the desorption profiles of SAMs in different media showed that the rate of desorption in gaseous media is slower than that of liquid media. The resultant kinetics of SAM desorption in air at different temperatures were modeled using the Eyring equation. Activation energy of desorption for HDT is calculated to be 30.5 kcal/mol in air, i.e. 15% higher than pervious results reported for desorption in liquid media. A two consecutive first order kinetics regimes (fast and slow) suggested in literature[27] was also examined and shown to better represent our results.

The experimental data of kinetics of SAM desorption in gaseous media was coupled with heat diffusion equation modeling. The results were used to better predict the chemical composition of the surface along and around the processed region. Calculation of the fraction of SAM remaining on gold surface after being scanned by the laser beam and determining the feature size based on chemical composition of the surface is also presented in Chapter 4. A comparison of the resulting theoretically predicted SAM fractions with experimentally measured final SAM profiles is also provided.

Nonlinear Patterns

In chapter 5 it is shown that the DLP method can be used as a free-hand pattern generating method and is capable of making various types of geometrical patterns including curvilinear paths and various junction types. In context of making curvilinear features, the effect of curvature of heating trajectory and heat source velocity on the induced temperature field is considered in terms of peak temperature and resulting feature size in Chapter 5. The results were compared with those of heating along straight line to show the effect of curvature. The effect of making certain geometrical patterns (crosses and angles) as well as the effect of heating trajectory's radius of curvature and heating spot's velocity on resulting surface temperature was considered. It was experimentally observed and theoretically demonstrated that within the range of parameters used for this study, the induced surface temperature profiles are symmetric. Experiments showed that channel width broadening will not happen at the cross junctions and near vertex of angular patterns. The observations were also theoretically discussed within a mathematical model. Temperature profile calculations showed that an order of magnitude increase in curvature at scanning velocity of 0.1 mm/s for a beam of 44 μm waist reduces the maximum induced surface temperatures by 7 K or 21 K at 1 mm/s. The theoretical findings and the model are also applicable for other temperature sensitive processes as well.

Table 1-1. The properties that can be manipulated on SAM surfaces.

Surface Property	Surface Manipulation Approach
Chemical functionality, including acidity/basic, oxidative/reductive, complex ligands	Removal of SAM in particular region and forming a second SAM with desired functionality in its place [6, 9, 13-15, 31, 35, 36]
Morphology and roughness	Ablation of a nanolayers of gold substrate with a femtosecond laser or pre-texturing of gold substrate followed by forming SAM, Roughness can be changed through roughening of substrate (which is measurable and controllable) followed by placing the SAMs on top [35]
Charge	SAMs with positive and negative charges on their tail groups can be patterned, e.g. carboxylic acid group versus amine group [6, 9, 13-15, 31, 35]
Surface energy	High energy tail groups (e.g. OH, COOH) or low energy tail groups (e.g. methyl) can be attached to surface [6, 9, 13-15, 31, 35]
Adhesion	SAMs with Adhesive or non-adhesive tail groups can be formed [6, 9, 13-15, 31, 35]
Wettability	SAMs with hydrophilic or hydrophobic tail groups can be formed [6, 9, 13-15, 31, 35]
Friction	Roughness and surface energy affect friction of surface; so, above mentioned strategies (combination of rows 2 and 4) can be used to manipulate surface friction [6, 9, 13-15, 31, 35]
Topology of surface	Patterning SAMs on curved or even flexible substrates can be attempted [36]

Table 1-2. Patterning Techniques for alkanethiol SAMs

Patterning Technique	Minimum Feature Sizes Achieved (Not typical values)	Substrate	Reference
UV lithegraphy	1 μm	Gold	[8]
Microcontact printing	50 nm	Gold	[3]
	2 μm	Silver	[1]
Dip-pen lithography	25 nm	Gold	[37]
Nanoshaving	400 nm	Gold	[1, 38]
Electron beam lithography	300 nm	Gold	[1]
Particle beam lithography	50 nm	Gold	[9,3]

References

(1) Senaratne, W.; Andruzzi, L.; Ober, C.K. *Biomacromolecules* **2005**, *6*, 2427-2448.

(2) Schreiber, F. *Prog. Surf. Sci.* **2000**, *65*, 151-257.

(3) Love, J.C. ; Estroff, L.A. ; Kriebel, J.K. ; Nuzzo, R.G.; Whitesides, G.M. *Chem. Rev.* **2005**, *105*, 1103-1169.

(4) Smith, R.K.; Lewis, P.A.; Weiss, P.S. *Prog. Surf. Sci.* **2004**, *75*, 1-68.

(5) Tender, L.M.; Worley, R.L.; Fan, H.; Lopez, G.P. *Langmuir* **1996**, *12*, 5515-5518.

(6) Xia, Y.; Whitesides, G.M. *Angew. Chem. Int. Ed.* **1998**, *37*, 550-575.

(7) Yang, Z.; Wolfgang, F.; Oliver, T.; Chilkoti, A. *Langmiur* **2000**, *16*, 1751-1758.

(8) Behm, J.M.; Lykke, K.R.; Pellin, M.J.; Hemminger, J.C. *Langmuir* **1996**, *12*, 2121-2124.

(9) Chabinyc, M.L.; Love, J.C.; Thywissen, J.H.; Cervello, F.; Prentiss, M.G.; Whitesides, G.M. *Langmuir* **2003**, *19*, 2201-2205.

(10) Delamarche, E.; Michel, B.; Kang, H.; Gerber, C. *Langmuir* **1994**; *10*, 4103-4108.

(11) Dulcey, C.S.; Georger, J.H.; Krauthamer, V.; Stenger, D.A.; Fare, T.L.; Calvert, J.M. *Science* **1991**, *252*, 551-554.

(12) Shadnam, M.R.; Amirfazli, A. The 8th Int. Conf. on Laser Ablation, Banff, Canada, 2005.

(13) Shadnam, M.R.; Luu, A.; Kirkwood, S.E.; Fedosejevs, R.; Amirfazli, A. The 230th ACS Nat. Meeting, Washington DC, 2005.

(14) Balgar, T.; Franzka, S.; Hasselbrink, E.; Hartmann, N. *Appl. Phys. A* **2006**, *82*, 15-18.

(15) Balgar, T.; Franzka, S.; Hartmann, N. *Appl. Phys. A* **2006**, *82*, 689-695.

(16) Qiu, T. Q.; Tien, C. L. *Int. J. Heat Mass Transfer* **1992**, *35*, 719-725.

(17) Schneider, P. J. *Conduction Heat Transfer*; Addison-Wesley: Cambridge, 1957; Chapter 1.

(18) Lax, M. *J. Appl. Phys.* **1977**, *48*, 3919-3924.

(19) Moody, J. E.; Hendel, R. H. *J. Appl. Phys.* **1982**, *53*, 4364-4371.

(20) Ferrieu, F.; Auvert, G. *J. Appl. Phys.* **1983**, *54*, 2646-2649.

(21) Ascough, J. *Opt. Laser Eng.* **1985**, *6*, 137-143.

(22) Waechter, D.; Schvan, P.; Thomas, R.E.; Tarr, N.G. *J. Appl. Phys.* **1986** *59*, 371-3374.

(23) Conde, J.C.; Lusquinos, F.; Gonzalez, P.; Leon, B.; Perez-Amor, M. *Vacuum* **2002**, *64*, 359-366.

(24) Shon, Y. S.; Lee, T. R. *J. Phys. Chem. B* **2000**, *104*, 8192-8200.

(25) Trevor, J.L; Lykke, K.R.; Pellin, M.J.; Hanley, L. *Langmuir* **1998**, *14*, 1664-1673.

(26) Nishida, N.; Hara, M; Sasabe, H.; Knoll, W. *Jpn. J. Appl. Phys.* **1996**, *35*, 799-802.

(27) Garg, N.; Carrasquillo-Molina, E.; Lee, T.R. *Langmuir* **2002**, *18*, 2717-2726.

(28) Wetterer, S.E. *Ph.D. Thesis Submitted to Princeton University*, NJ (Princeton) **1998**, Chap. 4.

(29) Nuzzo, R.G.; Dubios, L.H.; Allara, D. *J. Am. Chem. Soc.* **1990**, *112*, 558-569.

(30) Nuzzo, R.G.; Fusco, F.A.; Allara, D.L. *J. Am. Chem. Soc.* **1987**, *109*, 2358-2368.

(31) Shadnam, M.R.; Kirkwood, S.E.; Fedosejevs, R.; Amirfazli, A. *Langmuir* **2004**, *20*, 2667-2676.

(32) Shadnam, M.R.; Amirfazli, A. *Chem. Comm.* **2005**, *38*, 4869-4871.

(33) Shadnam, M.R.; Kirkwood, S.E.; Fedosejevs, R.; Amirfazli, A. *J. Phys. Chem. B* **2005**, *109*, 11996-12002.

(34) Shadnam, M.R.; Amirfazli, A. The 79th ACS Coll. Surf. Sci. Symp., Potsdam, New York, 2005.

(35) Kirkwood, S.E.; Shadnam, M.R.; Amirfazli, A.; Fedosejevs, R. *J. Phys.* in press.

(36) Jackman, R.J.; Wilbur, J.L.; Whitesides, G.M. *Science* **1995**, *269*, 664-666.

(37) Seo, K; Borguet, E. *Langmuir* **2006**, *22*, 1388-1391.

(38) Nuraje, N.; Banerjee, I.A.; MacCuspie, R.I.; Yu, L.; Matsui, H. *J. Am. Chem. Soc.* **2004**, *126*, 8088-8089.

Chapter 2- Direct Patterning of Self-Assembled Monolayers on Gold Using a Laser Beam*

Introduction

A self-assembled monolayer (SAM) forms when organic molecules, e.g. thiols and silanes, spontaneously adsorb on a surface, e.g. noble metals and silica.[1] Self-assembled monolayers are of significant importance for scientific and technological reasons. The most widely studied SAMs are those of alkanethiols, $HS(CH_2)_nX$, on gold films where X can be any of CH_3, COOH, NH_2, etc., see for example references [2-4]. Often for technological reasons a surface is required to have different properties at different regions, e.g. wettability, adhesion and different chemical functionalities. By changing the terminal group (X) and/or the length of the alkane chain (n), the surface characteristics, e.g. wettability or adhesion, can be manipulated in a SAM surface. Therefore, this capability can be exploited in fabrication of surfaces with different chemical and/or physical properties in neighboring regions. Such a surface is called a patterned surface. Self assembled monolayers on gold provide an excellent means for fabrication of patterned surfaces because SAMs on gold are easy to prepare, stable, densely packed, extensively characterized and studied, and available with different terminal groups.[5]

In a typical SAM system of alkanethiol on gold, strong chemisorption of alkanethiol molecules with more than 3 carbon atoms occurs as the result of the sulfur atom reacting with gold surface (see [1,6,7] and references therein). It is known that the gold-sulfur (Au-S) bond becomes unstable at elevated temperatures causing the SAM to desorb from the gold substrate.[1] Mass spectroscopic analysis of thermal desorption of alkanethiol SAMs on gold surface (deposited from ethanolic solution) show the SAMs desorb as dimer dialkyl disulfide molecules (2 Au- $S(CH_2)_nX$ = 2Au + $X(CH_2)_nS$- $S(CH_2)_nX$).[6] It is reported that in the resulting desorption mass spectra the signal associated with the dialkyl disulfide increased in magnitude as temperature increased during linear heating at rate of 0.3 K/s.[6] The desorption of SAM from the gold surface is thus shown to be a temperature enhanced reaction and the activation energy is reported to be 32 kcal/mol.[6] Therefore, it is expected that localized heating of the SAM surface can breakup the Au-S bond and produce bare regions of gold through thermal desorption. These bare gold regions can then be covered with a second alkanethiol with a different terminal group (X) and/or chain length (n) through solution deposition to alter the surface properties in those regions.

---

* A version of this chapter has been published. *Shadnam, Kirkwood, Fedosejevs, Amirfazli 2004. Langmuir. 20: 2667-2676.*

There are several ways for patterning a SAM coated surface; for example, micromachining,[8] microwriting,[9] photolithography/oxidative patterning using ultra violet (UV) light,[10] micro contact printing,[11] electrochemical stripping,[12] and dip-pen lithography.[13] However, all of these techniques with the exception of micro-machining, dip-pen and electrochemical stripping methods directly or indirectly use multiple lithographic steps which could entail problems associated with multiple mask alignments and loss of biological activity where bioactive agents are involved.[12] Micro-machining has limited application as it damages the substrate. In this article, we yet suggest another approach that uses a laser beam. A laser beam is an excellent means for precise localized heating. It can cause activation and/or acceleration of endothermic chemical reactions.[14]

For instance, by comparing cyclic voltammograms (2 mM $Fe(CN)_6^{3-}$ and 0.1 M KCl), it is shown that SAMs exposed to a laser beam in ultraviolet/visible wavelengths has been desorbed from gold surfaces.[15] The approach of "direct patterning" eliminates the need for photolithography directly or indirectly (the desired pattern can be formed by the relative movement of laser beam and the sample); it is non-contact, and also flexible, meaning that several terminal groups can be used in a single substrate. It also can be applied to other systems such as SAMs on silicon or potentially polymeric substrates. This method has potential to produce complex patterns; and last minute changes can be introduced without a major difficulty; it is fast; and it is a simple procedure. The latter three points are the advantages of direct laser patterning over the dip-pen lithography method, when it is used to produce features of the order of 1 μm or larger.

In this study, an argon laser at 488 nm is used to produce patterns of different wettability in the shape of a straight line with widths in the micrometer range. A 1-hexadecanethiol monolayer (hydrophobic) is desorbed by laser irradiation from the gold substrate producing bare gold regions. Then, 16-mercaptohexadecanoic acid (hydrophilic) self assembles on the produced bare regions through solution deposition. Using direct laser patterning method, we have produced straight line patterns with widths of 28 to 170 μm. In this way, laser is used to engineer wetting properties of a surface at microscale lengths.

The aim and scope of this manuscript are: Firstly, provide proof of concept for feasibility of the proposed methodology to manipulate properties of a surface composed of self assembled molecules (SAM) chemisorbed on an ultra thin gold film, based on thermal desorption of SAMs by means of a focused laser beam. Secondly, theoretical modeling of laser heating process to predict the feature size using the proposed methodology. A critical discussion of feasibility of the method in terms of the chemical reactions involved from both thermodynamic and kinetic points of view is also presented.

Sample Preparation and Experimental Setup

The samples were prepared using a 1 mm thick soda-lime Premium Microscope slide from Fisher Scientific Co. (Erie Electroverre). Standard methods were used to clean the slides to ensure surface cleanliness before forming the gold film. Surfaces were prepared by sequentially sputtering a 50 Å titanium adhesion layer and a 300 Å gold film layer in an ultra-high vacuum chamber on top of glass substrate (see further details in Appendix 1). After removal from the chamber, the slides were immediately placed in a 1 mM ethanolic (200 Proof Specialty Denatured Ethanol, Brenntag Canada Inc.) solution of 1-hexadecanethiol (Fluka) for more than 2 hours to form a monolayer of 1-hexadecanethiol molecules. The samples were rinsed with absolute ethanol and blown dry with nitrogen before being placed into the Environmental Process Chamber (EPC).

The optical setup used is shown in Fig. 2-1. A continuous-wave (CW) argon ion (Ar^+) laser beam (Coherent Innova 70-4) operating at the 488 nm line was focused onto the surface of the gold film which was moved at 200 μm/s. It increased the temperature to a level that desorbed the hydrophobic monolayer (1-hexadecanethiol). The output of the laser in TEM_{00} mode, i.e. having a circular Gaussian profile, was scanned across the sample by a mechanical stage. The laser was focused through a BK7 lens mounted on a translation stage to set the focal spot on the gold surface, two focal length plano-convex lenses were employed, +10 cm and +25 cm, to produce different scanning spot sizes. The focal beam spots were measured with a charge-coupled device camera imaging system (COHU 6612 CCD camera with Spiricon beam-analysis software). The measurements yielded the radii at $1/e^2$ peak intensity (2e-folding intensity radii) of 22 and 52 μm for the +10 and +25-cm focal-length lenses, respectively. Depending on the operating conditions of the old laser used, the beam sizes were found to vary from day to day leading to an uncertainty in the beam size of ±20%.

The focused beam was directed into EPC through a 1/16-inch thick BK7 glass window. This chamber when filled with nitrogen provided a non-reactive atmosphere to mitigate the effects of undesired species, e.g. water vapor and hydrocarbons, before immersion into the 16-mecaptohexadecanoic acid solution. The chamber was made of clear plexiglass with a removable wall for mounting components inside on a steel plate. A shower head style nozzle directed pure nitrogen (99.9998%) from the top into the chamber. With the nitrogen pressure set at 4 psig, the air was purged through a hole at the side of the chamber creating a 97% nitrogen atmosphere after 7 minutes. The EPC was designed to hold a 2D *x-y* controllable translation stage (Oriel stages with Encoder Mikes, 0.1 μm resolution) and a specially designed Teflon coated sample holder to move it transverse to the laser beam.

To calibrate the laser, the beam was aligned through the two apertures using the aluminum mirrors with the EPC and lens removed from the optical path. After alignment, the photometer used to measure beam energy was calibrated against a calibrated power meter (Newport 1815-C set in Low Power with Attenuator Mode; a Model 818-SL Head and Model 883-SL OD 3.0 filter) placed after the 2°-wedge quartz plate. The small attenuation due to the lens and entrance window in the EPC was calibrated by separate measurements and used to calculate the actual power at the sample position.

After calibration, the focusing lens was aligned in the system by examining the transmitted beam on the second aperture and the reflections from the two glass boundaries on the lens on the first aperture. The EPC was placed in the optical path and the back reflection of the coupling window was aligned with the first aperture. A gold-coated slide without a monolayer was mounted in the sample holder with the power set to minimum and the slide position was adjusted such that the back reflection was centered on the first aperture.

Patterning Procedure

The laser patterning procedure is a simple three step process: Initial formation of a homogeneous SAM surface; subsequent removal of SAM at desired locations by the laser; finally, solution deposition of another SAM with different terminal group in the irradiated bare regions. The last two steps can be repeated to pattern the surface with multiple SAM species.

The first step was described in sample preparation. After full alignment, the sample was mounted in the Teflon holder. The EPC was sealed and the nitrogen flow started; after 7 minutes, patterning of the monolayers began.

The second step of the laser patterning procedure involved laser irradiation while moving the sample by the micromanipulators to produce line shaped bare gold regions. Random triplicates of incident power values were used to minimize systematic errors and examine experimental error. The translation of the sample relative to the laser beam at constant speed uncovers a line of bare gold on the sample. The focused beam was scanned at 200 µm/s to draw 6 mm long lines. To ensure a minimum line width, which results from exposure to the focal point of the Gaussian beam, the lens was scanned through its confocal range during the 6 mm scan. The incident power was monitored before and after each scan (it had been noted that the power of the Ar^+ laser could drift).

The third step was immersion of the processed slide in 1 mM ethanolic solution of 16-mercaptohexadecanoic acid (Aldrich). The chamber was opened and the sample was removed. After a two-minute immersion, the sample was rinsed with ethanol, blown dry with nitrogen, and placed in a fresh container with absolute ethanol for storage.

Experimental Results

The results consist of evidence for existence of different wetting and electron absorption properties that confirmed the effectiveness of the laser patterning method; we also report laser power threshold for substrate damage and the minimum laser power to remove monolayers. The latter two laser thresholds provide the range of laser powers within which the laser patterning method can be used. The governing scaling relationship, i.e. how the width of the line pattern produced scales with the applied laser power, was also established. The scaling relationship provides a mean for prediction of laser power needed to make a hydrophilic feature of known width.

The existence of different wetting properties on the surface can be observed by noting that liquid tends to spread on the hydrophilic lines. The samples were imaged by optical microscopy within one day of the experiment. Placing a small drop of tridecane from a syringe, and drawing the drop along the hydrophilic lines creates fluidic lines as shown in Fig. 2-2a. The line widths of 16-mercaptohexadecanoic acid monolayer were measured using the image of the fluidic lines under the light microscope. A Capillary fingering effect[16] as result of competition between the evaporation and capillary effect is also observed under an optical microscope when ethanol is placed on the surface of the sample that further shows the existence of different wetting properties on the patterned surface. The width of the lines and presence of different SAM species was also verified with SEM images (Fig. 2-2d).

It was observed that a 500 mW beam focused with a +25 cm lens can damage the gold surface (Fig. 2-2b). The average intensity of the beam using 2e-folding intensity beam radius is 5.9 kW/cm^2. This intensity serves as an upper bound for the range of applicable laser powers in patterning, for the +25 cm lens.

Establishing the threshold for monolayer desorption involved gradually reducing the incident power from the damage threshold of the gold film until no desorption occurred. The surfaces were examined using SEM. Figures 2-2c and 2-2d show an unsuccessful and a successful patterning of the surface, respectively. The experimental results for the case where +10 cm lens is used show no monolayer removal for 30 mW laser incident power, while it shows removal for 39 mW laser incident power. It means that the removal threshold is between 30 mW and 39 mW (average intensity 1.9-2.5 kW/cm^2) where the +10 cm lens was used.[17] Similarly, the experimental results for the case where +25 cm lens was used show no monolayer removal for 100 mW laser incident power, while it showed removal for 104 mW laser incident power. Hence, the removal threshold is between 100 mW and 104 mW (average intensity 1.18-1.22 kW/cm^2) where the +25 cm lens is used. The calculated removal threshold average intensity for the case where +25 cm lens is used is less than that of the case where +10 cm lens is used by a factor of 2. It suggests that the energy transfer to SAM is not photochemically regulated (i.e. the individual or multiple photons or field components of the laser beam do not directly excite bonds and thereby initiate the desorption pathway). Theoretically, energy of photons at 488 nm, i.e. 2.54 eV is enough for breaking Au-S bond energy, i.e. 1.6 eV, however, chances of photons hitting the Au-S bonds that are buried in the well-packed structure of the SAM is slim. The alternative energy transfer is the thermally controlled mechanism, i.e. energy is absorbed by the substrate and provides localized high temperature and the resulting temperature field then cause desorption of the SAM.[18]

The measured experimental line widths as a function of applied laser power are presented using symbols in Fig. 2-3. Within the bounds of the two upper and lower thresholds, the higher the power the wider the line width. The laser power variation in 41 mW to 120 mW range focused by the +10 cm lens and the power variation in 104 mW to 186 mW range focused by the +25 cm lens are examined in this study. With the +25 cm lens, lines ranging from 90 μm to 200 μm in width were produced; for the +10 cm lens line features with widths ranging from 30 μm to 100 μm were produced. The two focal lengths yield different spots sizes and as such yield different intensities for the previously mentioned power ranges.

Theoretical Formulation

A mathematical model is defined to describe our system, the theoretical governing equations are formulated under some simplifying assumptions and relevant parameters are identified. Subsequently, the governing equations are solved and the effect of simplifying assumptions made during the formulation and solution are critically assessed. The model can be used to predict the patterning feature size based on experimental parameters, e.g. scanning speed, sample initial temperature and laser power.

Model Definition

Complete desorption of chemisorbed SAMs of different type (1,4-benzenedimethanethiol, 1-octadecanethiol and 1-octanethiol) from a gold surface have been reported to occur between 473 K to 493 K.[19-21] The surface temperature field induced by the CW moving laser beam is the effective parameter in prediction of the desorbed monolayer feature size. The geometry of the model used in calculations is shown in Fig. 2-4. The figure depicts a Gaussian laser beam intensity distribution shone on a sample surface scanning along the X axis.

Beside laser parameters, the induced temperature distribution depends on optical absorption within the irradiated zone, the transport of heat out of this zone and transformation enthalpies for desorption of the monolayer. The main variables involved in formulation of temperature field problem are thus the incident laser power, laser beam radius, scan speed, thermal conductivity, thermal diffusivity, optical absorption coefficient of the sample, and the energy needed to break chemical bonds between the gold and sulfur atoms. The incident laser power, the incident laser radius on the surface of the sample and scan speed can be set by appropriate optical and mechanical adjustments, the absorption percentage was measured and the thermal properties of the substrate glass are taken from both the manufacturer's data and also measured.[22] The energy needed to break chemical Au-S bonds was found in literature.[19]

Formulation of the Governing Equation

When the laser pulse duration is much longer than the electron-phonon thermal relaxation time, which is of the order of picoseconds, the laser heating can be modeled by the conventional heat diffusion mechanism.[23] The duration of the pulse in the CW regime is physically infinite. Thus, the heat diffusion model is used in this study. The governing differential equation for diffusive heat conduction is as follows (Fourier equation):[24]

$$\nabla \cdot \left[\kappa(T).\nabla T\right] + Q(x,y,z,t) = \frac{\kappa(T)}{D(T)} \cdot \frac{dT}{dt} \tag{1}$$

where κ, D, T, Q and t represent the sample thermal conductivity, thermal diffusivity, temperature, heat source function, and time, respectively. Furthermore, in Eq. 1, x, y, z denote stationary coordinates (Fig. 2-4) and d/dt is the time derivative. The thermophysical and optical properties of the sample are assumed to be independent of position and orientation within planes parallel to x-y plane due to homogeneity and isotropy of the glass substrate.

To determine the mathematical form of the heat source function, i.e. $Q(x,y,z,t)$ in Eq. 1, an analysis of laser absorption as it penetrates into the sample is needed. First, the percentage of the energy absorbed in different layers (gold, titanium and glass) should be considered. The absorption coefficients of glass and gold at 488 *nm* are 30 m^{-1},[25] and 0.685×10^{7} m^{-1},[26] respectively. Applying the Beer-Lambert absorption law,[27] it is calculated that more than 99% of the absorption occurs at the gold layer. Thus, in the presented thermal model it is assumed that the absorbed energy is fully delivered to the gold layer. The penetration depth of the laser which is, by definition, the inverse of the laser absorption coefficient, is 0.15 μm; the smallest intensity 2e-folding beam waist radius used in the experiments is 22 μm when the beam is focused by +10 cm lens. It means that the penetration depth of the laser is less than beam waist by two orders of magnitude. Thus, based on a Ferrieu and Auvert[28] analysis, a Dirac delta function in the z direction can represent the deposited energy penetration for the CW argon ion laser used. The energy distribution in X and Y directions is Gaussian. Hence, the moving heat source term in Eq. 1 is represented by:

$$Q(x,y,z,t) = 2\frac{PA(T)}{\pi w_0^2}\exp(-2\frac{(x-vt)^2+y^2}{w_0^2})\ \delta(z) \qquad (2)$$

where P, w_0, v, and A represent laser power, 2e-folding intensity radius of the laser beam, the speed of the sample movement relative to laser spot, and the optical absorption percentage of the sample, respectively. Near the beam waist, w_0 will be a sufficiently slowly varying function of depth, z, that w_0 is treated as constant in Eq. 2.[29]

As Boyd[18] recommends the energy consumed by all physical changes, e.g. melting, sublimation, and/or all chemical changes, i.e. any chemical reaction, should also be taken into account in formulation of amount of energy delivered to the surface (Eq. 2). The breaking of Au-S chemical bonds is endothermic. The enthalpy of Au-S chemical bond for thiols in SAMs on gold is 40 kcal/mol.[19] In the Schlenoff et al.[19] work, the overall monolayer adsorption is reported to be exothermic with enthalpy of –5 kcal/mol. Based on the studies performed on the packing of the thiol molecules adsorbed on the gold surface, the average surface area occupied by each thiol molecule is 21.6 Å^2.[1] Thus, the energy needed to break all Au-S chemical bonds is 3.22 $\text{fJ}/\mu\text{m}^2$ that is negligible compared to the energy delivered by laser beam. Thus, consideration of bond breaking energy does not change the results.

Due to high conductivity and low heat capacity of the thin gold and titanium layer compared with glass it is assumed that the temperature at the gold layer is equal to the temperature at the surface of the glass substrate. This assumption has been verified in similar systems.[30-32] For thin films on a substrate, Burgener and Reedy[30] showed that the thermal properties of the substrate supporting the film dominate and should thus be used in Eq. 1, if one is not concerned with the transient temperatures in the first few nanoseconds. The diameter of the laser spot is of the order of tens of micrometers whereas length and width of the sample are of the order of centimeters. Therefore, it is assumed that the substrate is physically an infinite media in X and Y directions and the edge effects on the local thermal field around the heating spot can be neglected. Hence, the model is simplified to an infinite substrate in X and Y directions and thermal properties are from glass microscope slides.

Substituting Eq. 2 into Eq. 1 gives the complete form of the governing differential equation of the model. Due to temperature dependence of coefficients in Eq. 1, i.e. thermal conductivity, thermal diffusivity and absorption coefficient, the governing partial differential equation is a nonlinear equation. This nonlinear partial differential equation is non-autonomus and admits no classical integral. In order to simplify the equation, the dependence of optical absorption on temperature is neglected noting that at wavelength used (488 nm), the temperature dependence of optical absorption is typically small for most metals before melting; also the maximum temperature coefficient of reflectivity for gold is of the order of 10^{-5} K^{-1} in wavelength range from 200 to 700 nm.[23]

The substrate was assumed to be a half-space adiabatically insulated on its surface. The following initial and boundary conditions were adopted:

$$T(t \to 0) = T_0 \qquad (3)$$
$$T(r \to \infty) = T_0$$

where r represents radius in standard spherical coordinate system and T_0 is ambient (initial) temperature.

Lax[33] showed that the nonlinearity due to temperature dependence of conductivity in the governing heat conduction equation, i.e. Eq. 1, can be removed by employing the Kirchhoff transformation. This transformation can yield a linear partial differential equation, if the diffusivity is not temperature dependent. In this study, it will be shown that temperature dependence of sample thermal diffusivity can be neglected for our set of experimental parameters. Then, Kirchhoff transformation is used to linearize Eq. 1. The calculations are based on the Moody and Hendel[34] steady state solution of Eq. 1 in moving coordinate system, which uses the same transformation. Ferrieu and Auvert[28] transient solution is also used for comparison and verification of the results. Both of the references formulated the resulting temperature profile using Green functions for the linearized equations.

Definition of Governing Equation Coefficients

In order to predict the temperature profiles, the values of all the parameters involved in Eqs. 1 and 2 are needed. Values of the parameters relevant to the theoretical model are given in Table 2-1. The thermal properties listed in Table 2-1 are those of the soda lime glass. Considering the available data for soda lime glass, simplifying assumptions are made regarding the temperature dependence of both thermal diffusivity and thermal conductivity. Then, the effects and consequences of alternative assumptions about temperature dependence of thermal diffusivity and thermal conductivity on results are considered and the validity of the assumptions are assessed.

Araki and Sasahara[35] measurements show that the diffusivity of soda glasses change by at most 10% in the range of 250 K to 800 K. Experimental measurements also show a change of 10% in the thermal diffusivity for 298-348 K temperature range.[22] Furthermore, in agreement with results obtained by Ferrieu and Auvert[28] in modeling of a similar system, it is shown that the temperature dependence of diffusivity does not change the resulting temperature profile significantly. Therefore, temperature dependence of diffusivity is ignored in this study.

An analysis was used to study the effect of diffusivity on resulting temperatures. It was found that the steady state temperature of the substrate (in moving coordinate system) is not changed significantly when the diffusivity coefficient varies by 10% further verifying the appropriateness of the constant diffusivity assumption. The negligible effect of temperature dependence of diffusivity on resulting temperature profiles in this particular problem, however, does not mean diffusivity is constant in general.

Conductivity values of the sample at different temperatures are needed to perform the Kirchhoff transformation.[33] In order to develop a rational basis for the substrate conductivity-temperature relation, conductivities of soda lime glasses having chemical compositions similar to the one used in our experiments are shown in Fig. 2-5. Most of the thermal conductivities show a linear growth in the range of 300 K to 1000 K. The conductivity-temperature relation can be assumed linear. Our results also show that linear temperature-conductivity function is reasonable as considering various functional forms (e.g. second order polynomials and inverse square function with various coefficients) only results in a shift up/down of the theoretically predicted line widths for different laser powers. Therefore, a linear approximation of the conductivity temperature dependence will not cause significant errors in the theoretical predictions. To find a generic conductivity-temperature slope a line is fitted to all the collected data (Fig. 2-5). The resulting slope value (0.68 mW/mK^2) was used in calculations (temperature dependence of thermal conductivity values for the glass used in this study was not available). Since the range of conductivity values for glasses having similar chemical composition to the one used in these experiments is wide, a question arises as to how the theoretical line widths change with variations of the conductivity-temperature course within the collected data envelope. Comparison of the predicted line widths showed that a net conductivity increase results in a net downward shift of line widths and vice versa. It was also observed that predicted line widths change proportionally with respect to the slope of the conductivity temperature dependence, i.e. changing the slope of temperature dependence of the substrate conductivity did not change the slope of the theoretical line widths versus applied laser power. Key characteristics of the theoretical curve describing the relationship between line widths and laser powers, e.g. slope and curvature, were not sensitive to variations of conductivity-temperature relationship within the collected data envelope.

Temperature Profiles

Equation 1 was numerically integrated using the Runge-Kutta algorithm of Maple 8 software. Validation of the code was done using a control experiment in which laser was used to melt polypropylene films on gold samples; theoretical and experimental width of melted regions matched each other.

A typical temperature contour plot (at the plane of the surface) obtained from the model by the preceding procedure is presented in Fig. 2-6. It shows the constant temperature isotherms at the surface of the substrate in the X-Y plane. At the 200 μ m/s speed of the heating spot, each point of the sample on the scan axis experiences 500 K or higher temperatures for approximately 0.3 s. Using 0.2 s as half life of desorption in 500 K,[36] one can calculate that more than 99% of the thiol molecules are removed from each point of the sample at centerline of the scanning spot.

Our calculation based on the model shows that the point of hottest temperature is at negligible distance from the instantaneous spot of the moving beam. Both occurrence of maximum temperature at center of heating spot and negligible asymmetry of temperature profiles are in agreement with the theoretical results obtained by Burgener and Reedy[30] for heating of an essentially similar two-layer system. They ascertained unimportant asymmetry of the resulting temperature profiles in the X and Y directions before a certain velocity threshold ($v<0.3D_{Top\ layer}/w_0$).

Monolayer line widths can be predicted using temperature profiles and monolayer removal temperature threshold. The predictions obtained from the model can be compared to the experimental measurements and will be discussed in the following section.

Results and Discussion

Predicted monolayer line widths based on the transient solution at steady state limit are compared with the line widths based on a steady state solution in moving coordinate system. Ferrieu and Auvert[28] and Moody and Hendel[34] formulations are examined with parameters chosen to represent experimental conditions. The transient temperature profile at a representative time (after 2.5 min when the spot has moved 3 cm away the starting point) based on the Ferrieu and Auvert[28] approach is compared with the steady state temperature profiles based on the Moody and Hendel[34] approach. The resulting removed monolayer widths (assuming the desorption temperature to be 480 K in middle of the range reported in literature for complete desorption of various types of chemisorbed SAMs from gold surface, i.e. 473 K to 493 K.[19-21]) versus target incident power are in very good agreement (Fig. 2-3). The removed monolayer line widths obtained based on steady state solution are less than the ones obtained based on transient solution by at most 1.5% (Fig. 2-3). Moreover, results of both formulations predict no monolayer removal for 40 mW laser incident power when +10 cm lens is used and 100 mW when +25 cm lens is used, which are in good agreement with the experimental ranges for removal threshold reported in Section 5.1. The very good agreement of the two theoretical formulations

(Fig. 2-3) show that steady state solution can be used in general to calculate the parameters of interest to the present study.

Comparison of Theoretical and Experimental Results

Theoretically predicted line widths at different values of the laser power are compared to experimentally measured values in Fig. 2-3. The percentage of differences between the predictions and measured values in Fig. 2-3 is higher at lower laser powers. Schvan and Thomas[37] in consideration of CW laser induced melting of silicon have also reported such a deviation in comparison of calculated versus measured melt depths. This is because the spatial gradient of the temperature change is lower at lower incident powers. Figure 2-7 shows that the sensitivity of the obtained results to the temperature including that the sensitivity coefficient[38] (The first derivative of feature line width with respect to the temperature) is larger at high powers. If the sensitivity coefficient is large, the estimation of line width is very sensitive to errors.[38] It means any uncertainty and/or deviation from the calculated temperatures due to factors such as instantaneous instability in laser light intensity, deviation of laser from the TEM_{00} mode, may cause significant difference in the results at higher powers. Figure 2-7 also shows that sensitivity of the line widths to desorption temperature for the case where a +10 cm lens was used is less than that of a +25 cm lens; this is also apparent in Fig. 2-3 where the deviation of the theoretical line width predictions from experimental measurements in Fig. 2-3a (+10 cm lens) is less than that of Fig. 2-3b (+25 cm lens).

The calculated maximum temperature for the case where the gold surface was damaged, i.e. 500 mW laser focused using a +25 cm lens is 1585 K; this is calculated by taking into account the finite depth effects (a correction of 18%).[39] The calculated value differ from the gold melting point, i.e. 1337 K,[40] by 15%, , which is within the error bar of the beam focal spot size. The degradation of thermal conductivity in a local area (as a result of tiny cracks or imperfections) prevents heat from dissipating into the surrounding media and may significantly increase local temperature.[41]

To compare theoretical predictions with experimental results a quantitative measure of the difference between the theoretical results and experimental measurements is defined. The measure, *e*, is defined as sum of absolute values of the difference between the experimental and theoretical laser incident powers at constant line width value for all experimentally examined data points. The *e* was minimized with respect to 1-hexadecanethiol desorption temperature. It was observed that the best correlation of the experimental results with theoretical calculations occur for desorption temperature of 485 K (Fig. 2-8). Figure 2-9 shows the best fit isotherm (solid line) and limits of a 40 K wide envelope (dashed lines). It is reported that different SAMs on gold are completely removed in the temperature range of 473 K to 493 K.[19-21] It is also shown that a slow desorption regime exists even below this temperature.[42,43] The calculated desorption temperature is within the range of reported complete desorption temperatures.

Figure 2-10a shows *e* as function of both desorption temperature and conductivity-temperature slope. The topography of the surface shows that the there exists a line of minimum error rather than a singular minimum point, i.e. for each conductivity-slope value there exists a unique desorption temperature that minimizes the *e*. Thus, using above calculated 485 K as desorption temperature, the assumed generic slope (0.68 mW/mK^2) minimizes the *e*. A similar test is performed on the conductivity value at 298 K with 485 K as desorption temperature and the assumed generic slope (0.68 mW/mK^2), see Fig. 2-10b. It appears that the measured conductivity value[22] agrees with the optimal value. Therefore, the conductivity-temperature relation used readily minimizes the difference between the theoretical results and experimental measurements.

Minimization of the *e* with respect to the incident beam waist radius shows that the minimum difference occurs at 2e-folding intensity beam radius of 31 μm where the +10 cm lens is used (Fig. 2-11a). Similar analysis results in 2e-folding intensity beam waist radius of 89 μm where +25 cm lens is used (Fig. 2-12a). Using the calculated 2e-folding intensity beam waist radius values, the theoretical line width of the removed monolayer versus incident power is presented in Figs. 2-11b and 12b showing good agreement with experimental results. Moreover, the flat region in Figs. 2-11a and 2-12a suggests that at very narrow beam waists there is little difference between a point source and a source with Gaussian profile. However, our Gaussian source can not be approximated by a point source. Furthermore, the curve in Fig. 2-12a does not have a pronounced minimum like the one in Fig. 2-11a because of scatter in experimental data points in Fig. 12b when compared to experimental data points in Fig. 2-11b.

It can be concluded that the presented model can be used to predict monolayer removal line widths. The quantitative comparison of the experimental measurements with the theoretical results showed that neither variations in the conductivity parameters nor the monolayer removal temperature could change the trend of the theoretical predictions to make them better follow the experimental measurements pattern. Phenomenologically, it is observed that the measurements correlate with theoretical isotherms of a narrower effective beam waist better than isotherms of the used beam waist for both +10 cm and +25 cm lenses.

Feasibility of Laser Patterning

Feasibility of the patterning method in terms of the chemical reactions involved from both kinetics and thermodynamic points of view is discussed. The reactions are expected to be spontaneous, i.e. lead to thermodynamically more stable species, in an experimentally reasonable time. The selection of the chemicals can greatly influence effectiveness and thus feasibility of laser patterning. The reactions in the proposed direct laser patterning method are considered.

The second step of the laser patterning process involves the desorption reaction of SAM from the gold surface. To our knowledge, no quantitative thermodynamic or kinetic information dealing with desorption of thiols into a gaseous medium is yet published. Quantitative data obtained from studies involving desorption of monolayers in a liquid medium perhaps can be used as an approximation. However, extrapolation of the data related to energetics of the desorption in liquid medium to gas medium should be done carefully as the thiol molecules may interact with solvent molecules. The feasibility of the desorption reaction is considered form both kinetic and thermodynamic points of view.

Kinetics of desorption for different classes of SAMs from gold substrate in isooctane and decalin solvents at 333 to 383 K is considered by Garg et al.[42] and it is concluded that there exist two distinguishable desorption kinetic regimes: an initial fast regime followed by a slower regime. Both of the desorption regimes are shown to be temperature enhanced. The desorption standard activation free energies for different monolayers are shown to be 27 ± 1 kcal/mol at 298 K during the fast desorption regime.[42] The activation enthalpy and entropy is shown to be 28 kcal/mol and 8 kcal/mol.K, respectively, for 1-hexadecanethiol during the fast desorption regime.[42] By fitting the kinetic data obtained during the fast desorption regime in decalin as solvent to a first order reaction kinetics, the rate constant is shown to be about 0.18 min^{-1} at 363 K for 1-hexadecanethiol (experimental error is estimated to be ± 15%).[42] The general desorption kinetics taking into account both rapid and slow regimes shows that the time needed for desorption of three forth of the monolayer at 373 K in decalin solvent is 15 minutes.[42]

We could not find information regarding the temperature variation of SAM desorption thermodynamic energetics, i.e. enthalpy and entropy, at elevated temperatures, showing an ultimate value for desorption. However, desorption studies of Garg et al.[42] show that practically all monolayer can be desorbed. Therefore, the desorption step is expected to be both thermodynamically and kinetically feasible.

It is desired that 16-mercaptohexadecanoic acid form monolayers only on bare gold.[12] Replacement of thiols does not involve major exchange of energy but increases entropy. The equilibrium constant should be almost unity and it increases with temperature. In contrast, the thiol adsorption has equilibrium constant of 1.1×10^{4}.[19] Thus, in the equilibrium conditions the 1-hexadecanethiol monolayer reduce the absorption of 16-mercaptohexadecanoic acid by four orders of magnitude.

Thermodynamic equilibrium constants only show the final equilibrium situation of the system. Thus, although reduction of the equilibrium constant is a necessary condition to show the shielding capability of a homogeneous monolayer of 1-hexadecanethiol in the equilibrium condition, it may not be a sufficient condition in the experimental reaction time scale. From kinetics point of view, Kakiuchi et al.[36] showed that the replacement of adsorbed 1-hexadecanethiol with 12-mercaptohexadecanoic acid molecules, which differs from 16-mercaptohexadecanoic acid by only four methylene units, in 1 mM ethanolic solution at 304 K adopts a pseudo-first-order kinetics. They report the rate constant of 9.1×10^{-3} h^{-1} for the thiol replacement reaction. In other words, the half-life of the exchange reaction is more than 76 hours, which is long compared to the solution deposition time in the experiment that is of the order of a few minutes. The exchange half-life is by 5 orders of magnitude less than thiol deposition half-life, which is reported to be of the order of a few seconds.[19,44] Thus, 1-hexadecanethiol SAM can effectively shield adsorption of 16-mercaptohexadecanoic acid and result in adsorption of 16-mercaptohexadecanoic acid only on bare gold regions.

Furthermore, it is shown that the opposite exchange reaction, i.e. the replacement of adsorbed 16-mercaptohexadecanoic acid with 1-hexadecanethiol molecules in the solution is shown to be much slower.[36] This confirms that making negative patterns with the above two species is also feasible. However, sensitivity of 16-mercaptohexadecanoic acid SAM to oxygen in ambient air requires usage of inert (non-reactive) atmosphere from the beginning of the first step of laser patterning process.

Summary and Conclusions

A new laser patterning technique is developed that directly uses laser for microengineering of SAM coated surfaces. The successful application of the developed methodology is reported for micropatterning of hydrophilic/hydrophobic functionalities using SAMs of alkanethiols on a gold film. In this technique, localized regions of an initially coated SAM on the substrate is desorbed by scanning the focal spot of a CW laser beam. The thermal desorption in the form of dimerized species occurs as result of high substrate temperature produced by the moving laser beam. After completing the scans, another SAM (with different characteristics) is let to self-assemble along the previously irradiated regions through solution deposition. Feature sizes are determined both experimentally and theoretically. Using the direct laser patterning method, straight line patterns was produced with widths of 28 to 170 micrometers. Direct laser patterning approach is unique in that it eliminates the need for photolithography, is non-contact, and can be extended to other systems such as SAMs on silicon wafers or potentially polymeric substrates.

The application of the Fourier's diffusion equation in theoretical prediction of the temperature profiles at the surface of the sample and feature sizes produced through thermal desorption of SAMs is also shown. The constructed model for a scanning CW circular TEM_{00} laser beam considered the temperature dependence of the substrate thermal properties, i.e. thermal conductivity and thermal diffusivity, and the energy needed to conduct the endothermic Au-S chemical bond breaking.

To compare theoretical predictions with experimental results a quantitative difference measure (*e*) was defined. The quantitative comparison of the experimental measurements with the theoretical predictions provided a means to infer the desorption temperature from the experimental results. It was found that 1-hexadecanethiol desorption temperature is 488 K which is in agreement with the value reported in literature for desorption in solvents. Using 488 K as desorption temperature, it was found that the theoretically predicted line widths are in good agreement with the experimentally measured line widths. The *e* values were also used to verify the assumed values for sample conductivity at different temperatures; They were all successfully verified.

The results show the effectiveness of the theoretical model in describing the monolayer removal process. Therefore, the predictions of the model can be used to set experimentally controllable parameters, e.g. laser power, beam waist radius, scanning speed. for obtaining a predetermined patterning feature size.

Table 2-1. The numerical values of the parameters in Eqs. 1 and 2.

k, Thermal conductivity at 298 K (Erie)	0.872 W/mK
D, Thermal diffusivity (Erie)	0.33 mm^2/s
v, Spot speed (Controlled)	200 μm/s
w_0, 2e-folding intensity beam radius (+10 cm lens) (Measured)	22 μm
w_0, 2e-folding intensity beam radius (+25 cm lens) (Measured)	52 μm
A, Optical absorbance of the sample (Measured)	44%

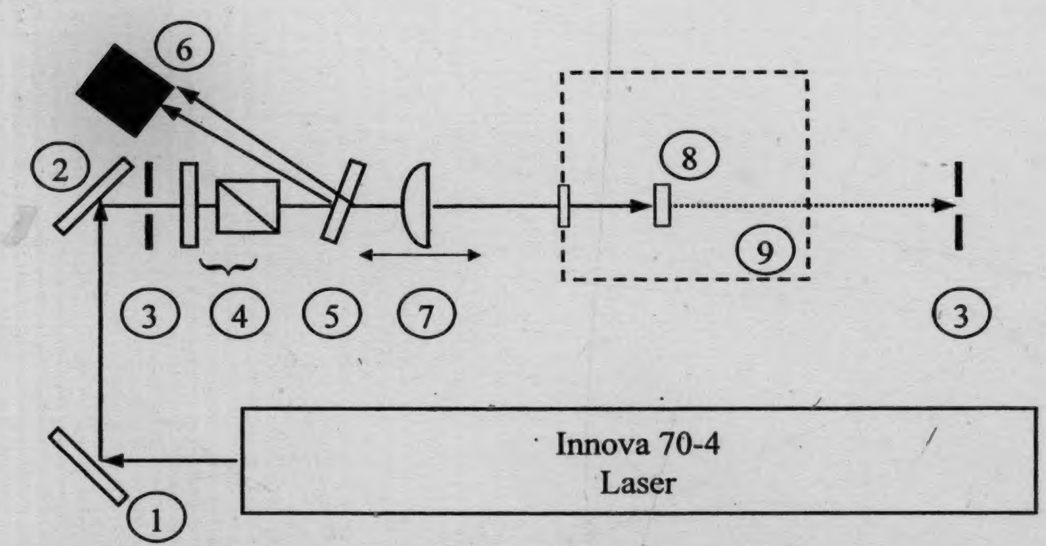

Figure 2-1. Schematic of the experimental setup for laser patterning of a surface by direct writing. The output of the laser is steered by two 1-inch aluminum mirrors (1 and 2) for alignment through two apertures (3). Attenuation optics, a combination of a half-wave plate mounted on a rotation mount and a Glan polarizer that leaves the beam vertically polarized (4), adjusts the desired incident power to the monolayer sample (8). A 2°-wedge window (5) reflects 4% of the selected laser power from the front face to a photometer (Industrial Fibre Optics Photometer) (6) for monitoring the laser power. The back face reflected beam is dumped onto an anodized surface. Focusing the laser through a BK7 lens (plano-convex, +10 cm or +25 cm focal lengths) (7) mounted on a motion stage to set the focal spot on the gold surface creates the different scanning spot sizes. The focused beam is directed into an Environmental Process Chamber (9) through a 1/16-inch thick BK7 window.

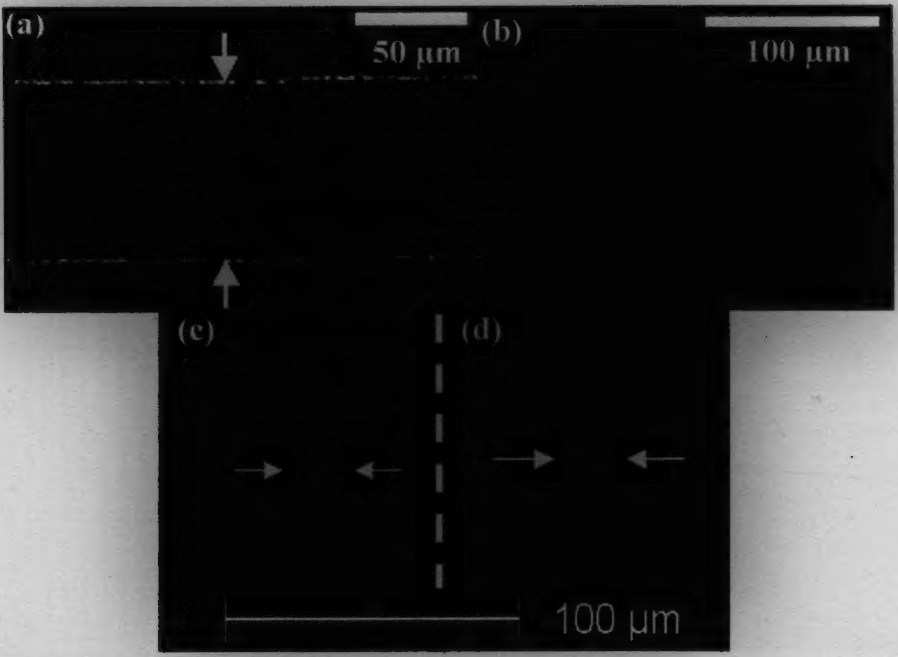

Figure 2-2. (a) A 70 µm wide hydrophilic line, delimited by arrows, written with a 90 mW Ar$^+$ beam focused by a +10 cm BK7 plano-convex lens. The contrast difference is a result of tridecane confinement within the hydrophilic region of the surface. The scale bar is 50 µm long. (b) An optical microscope picture of the damage on the gold film formed by overheating the glass slide. The scale bar is 100 µm long. (c) SEM image of scanned region. A 30 mW laser beam was focused using a +10 cm lens in the region between the two arrows and did not yield hydrophobic monolayer desorption. (d) SEM image of scanned region. A 50 mW laser beam was focused using a +10 cm lens and the hydrophobic monolayer was desorbed and replaced by the hydrophilic monolayer (formation of the dark strip).

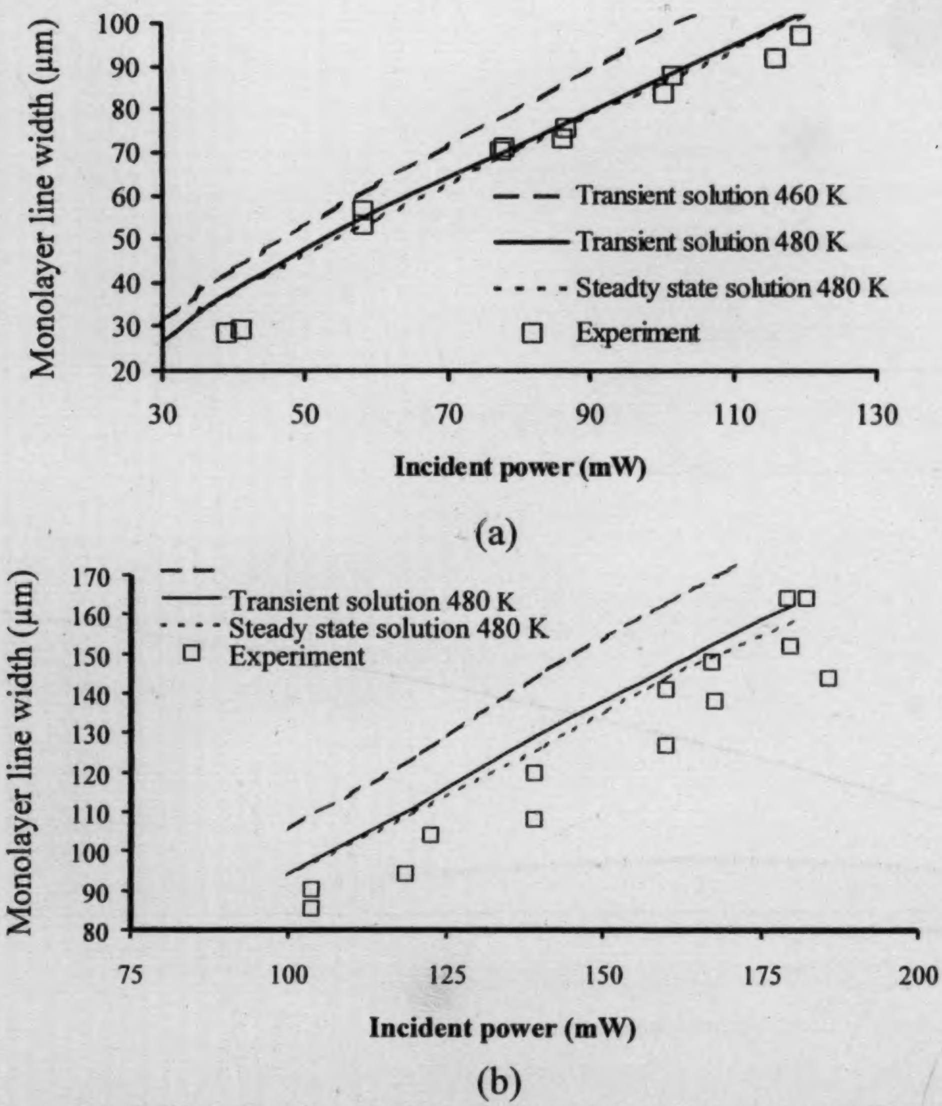

Figure 2-3. Scaling of replaced monolayer line width with laser power. The symbols represent experimental measurement using optical microscope for tridecane confinement; and the lines represent theoretical modeling results. To focus the laser beam a +10 cm lens is used in (a) and a +25 cm lens is used in (b). The line width predictions based on formulation by Ferrieu and Auvert[28] transient state (thermal conductivity of 0.872 W/mK at 298 K a rate of 0.68 mW/mK^2) and Moody and Hendel[34] steady state formulations.

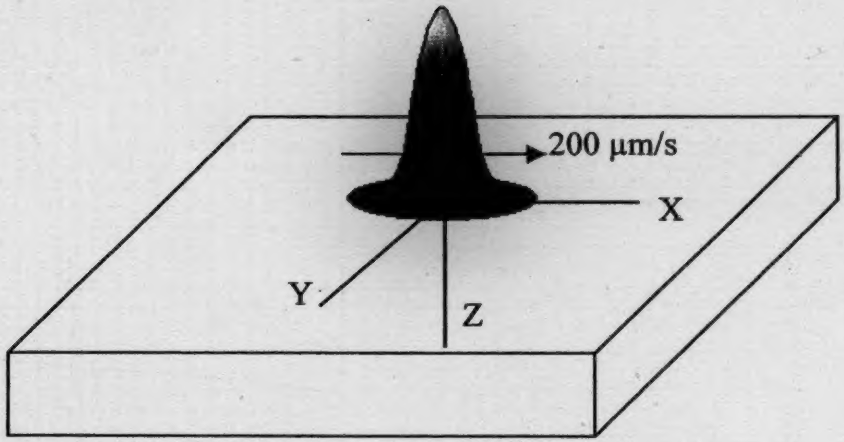

Figure 2-4. Cartesian coordinate system used to define directions in Eqs. 1 and 2. The figure represents a Gaussian TEM_{00} laser beam on sample surface scanning along the X axis.

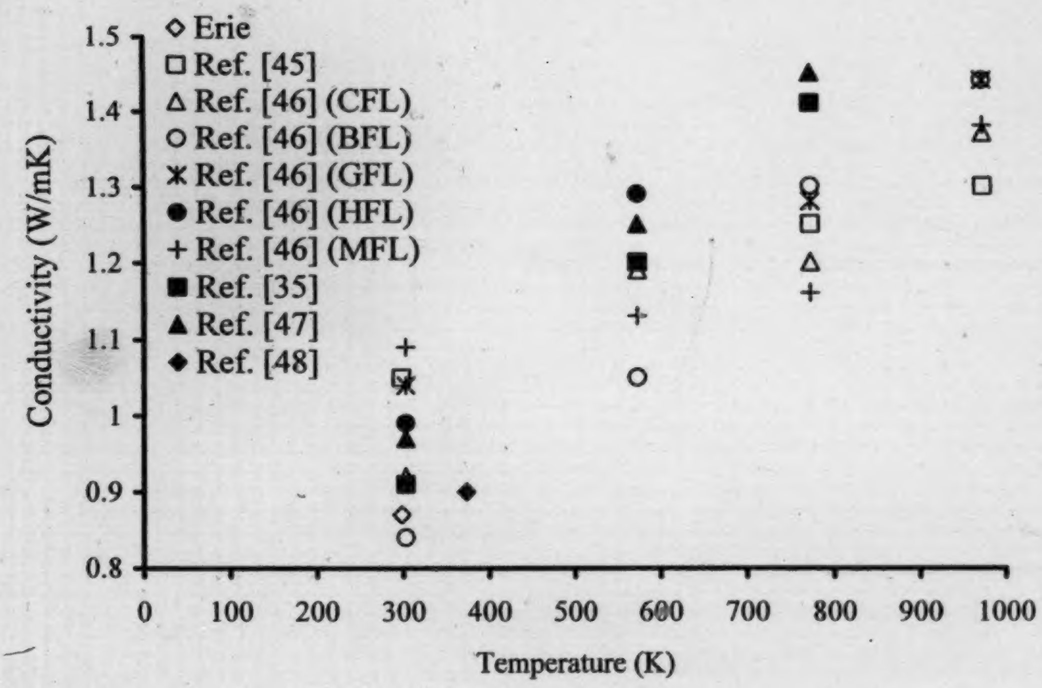

Figure 2-5. Thermal conductivity of the available data for soda lime glasses.

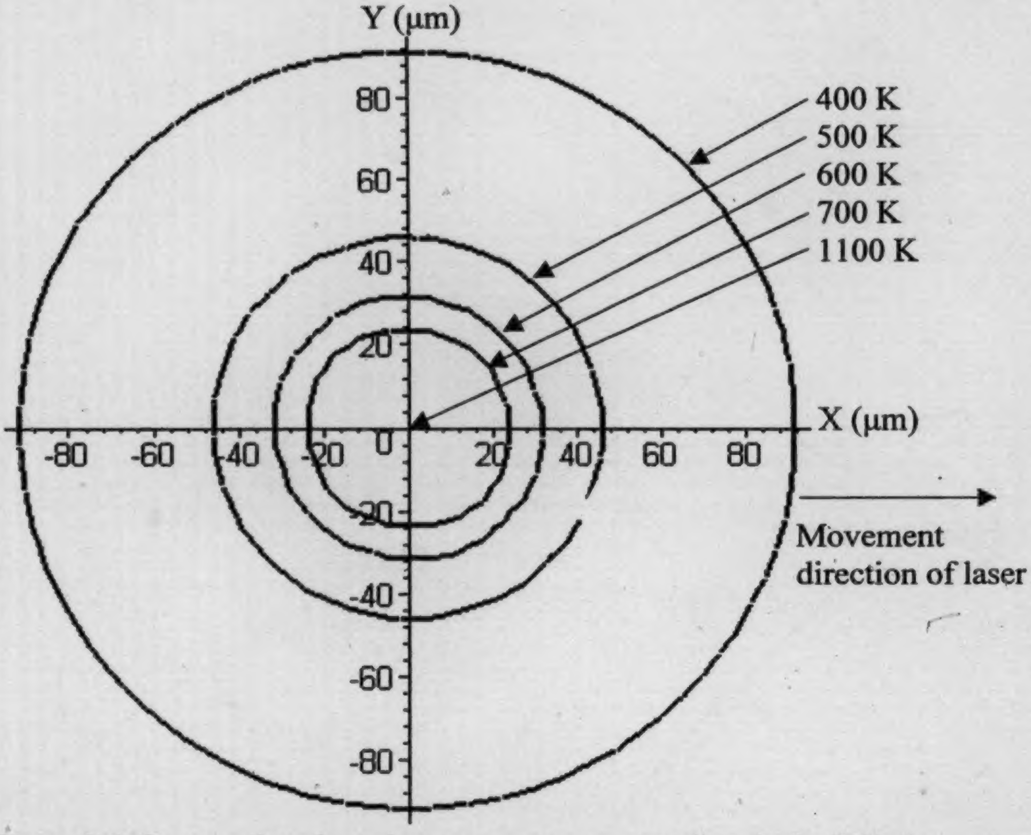

Figure 2-6. Contour plot of transient temperature constant lines in the X-Y plane, where a +10 cm lens with 120 mW power is used. The 2 e-folding intensity radius of the spot is 22.2 micron. The spot is at center of the coordinate system and its movement direction is along the X axis from left to right (toward positive values of X direction).

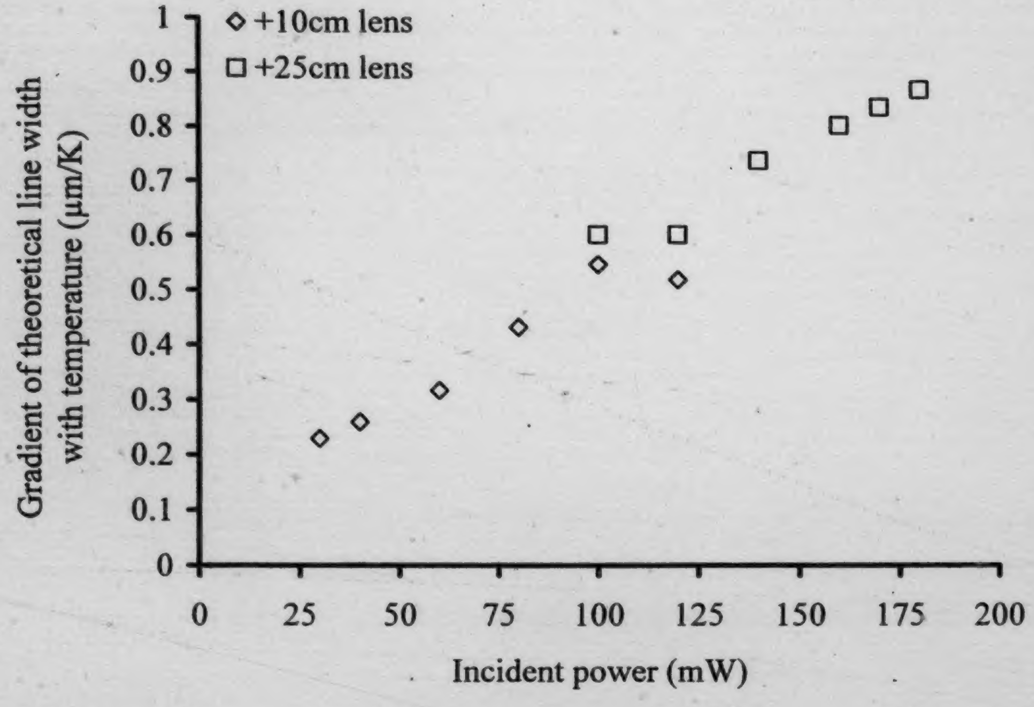

Figure 2-7. Sensitivity of the SAM feature line widths to variations in temperature at 480 K (thermal conductivity of 0.872 W/mK at 298 K a rate of 0.68 mW/mK^2).

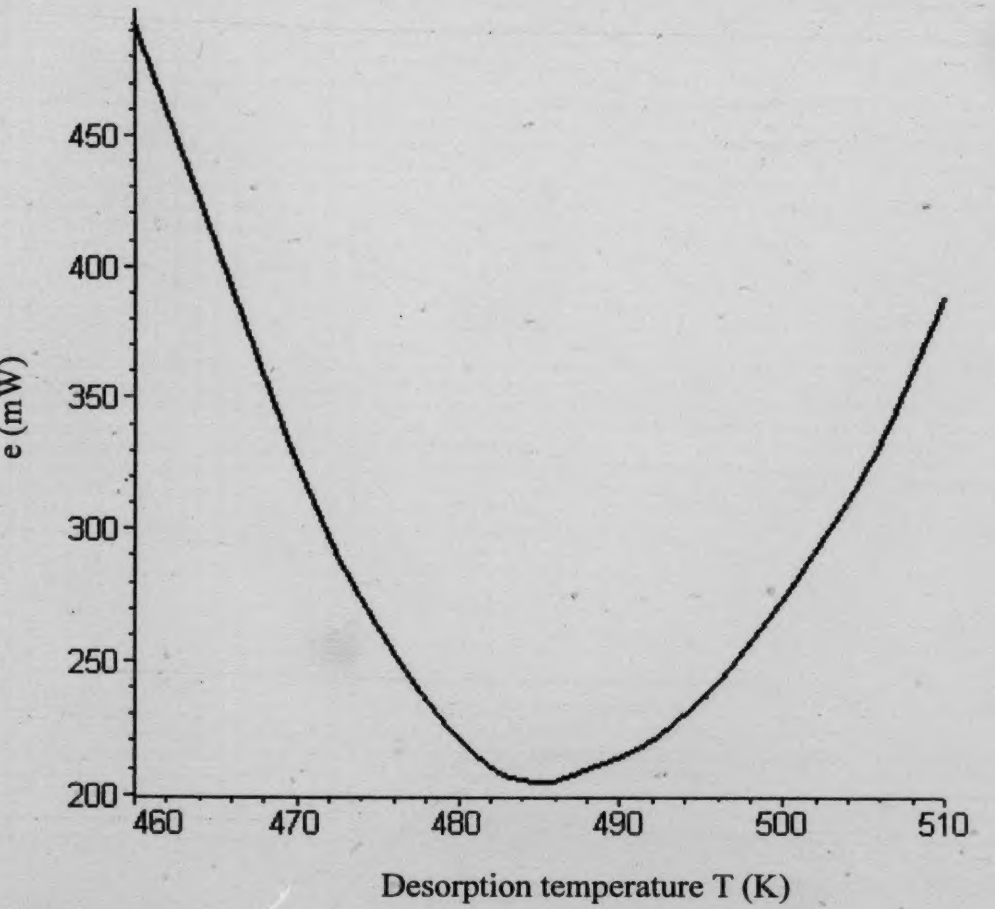

Figure 2-8. The *e* versus 1-hexadecanethiol SAM removal temperature. The figure shows the most appropriate temperature for monolayer desorption from gold substrate.

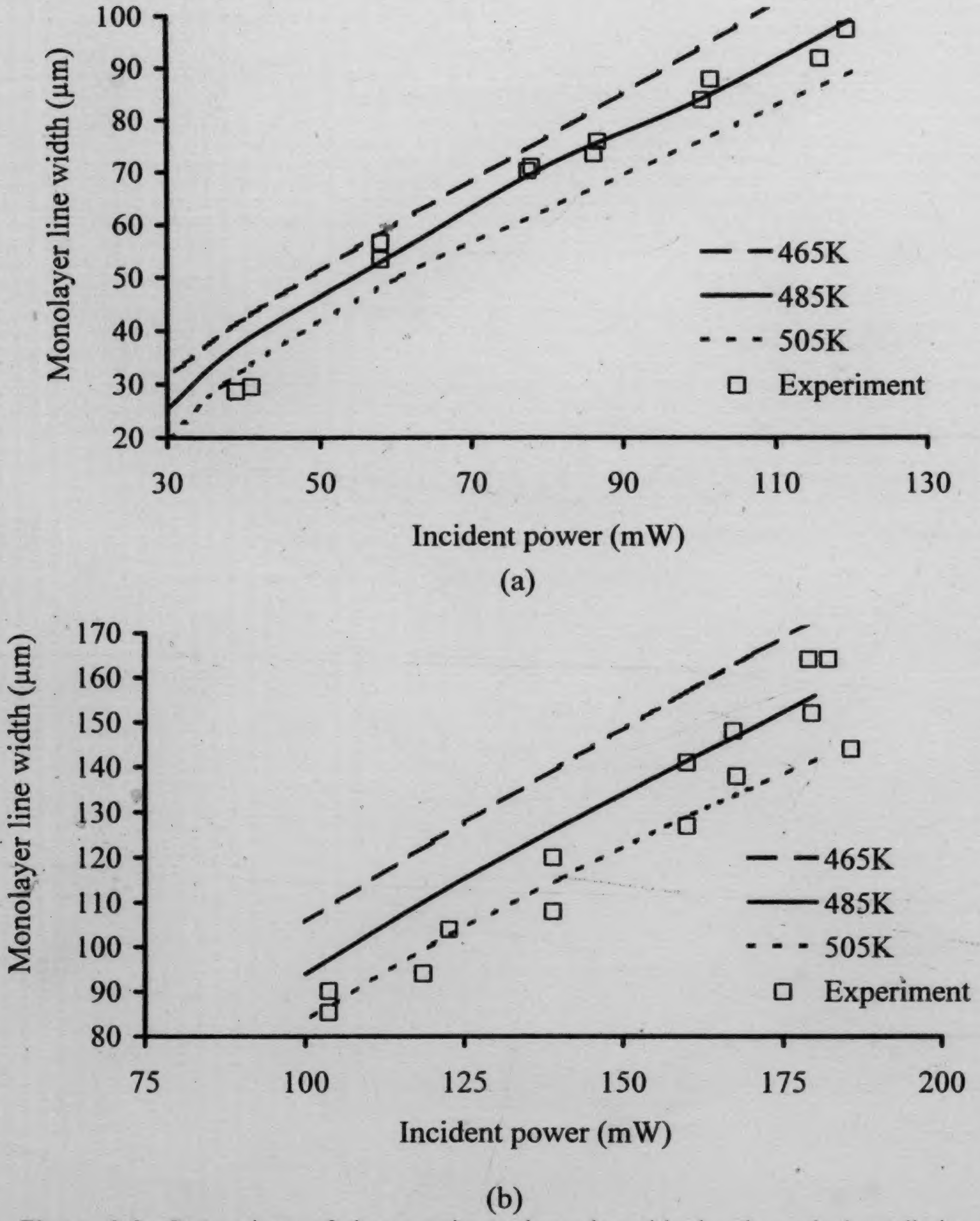

Figure 2-9. Comparison of the experimental results with the theoretical predictions. (a)+10 cm (b)+25 cm was used. Optimized values for desorption temperature (488 K) and conductivity-temperature slope is used (0.68 mW/mK^2).

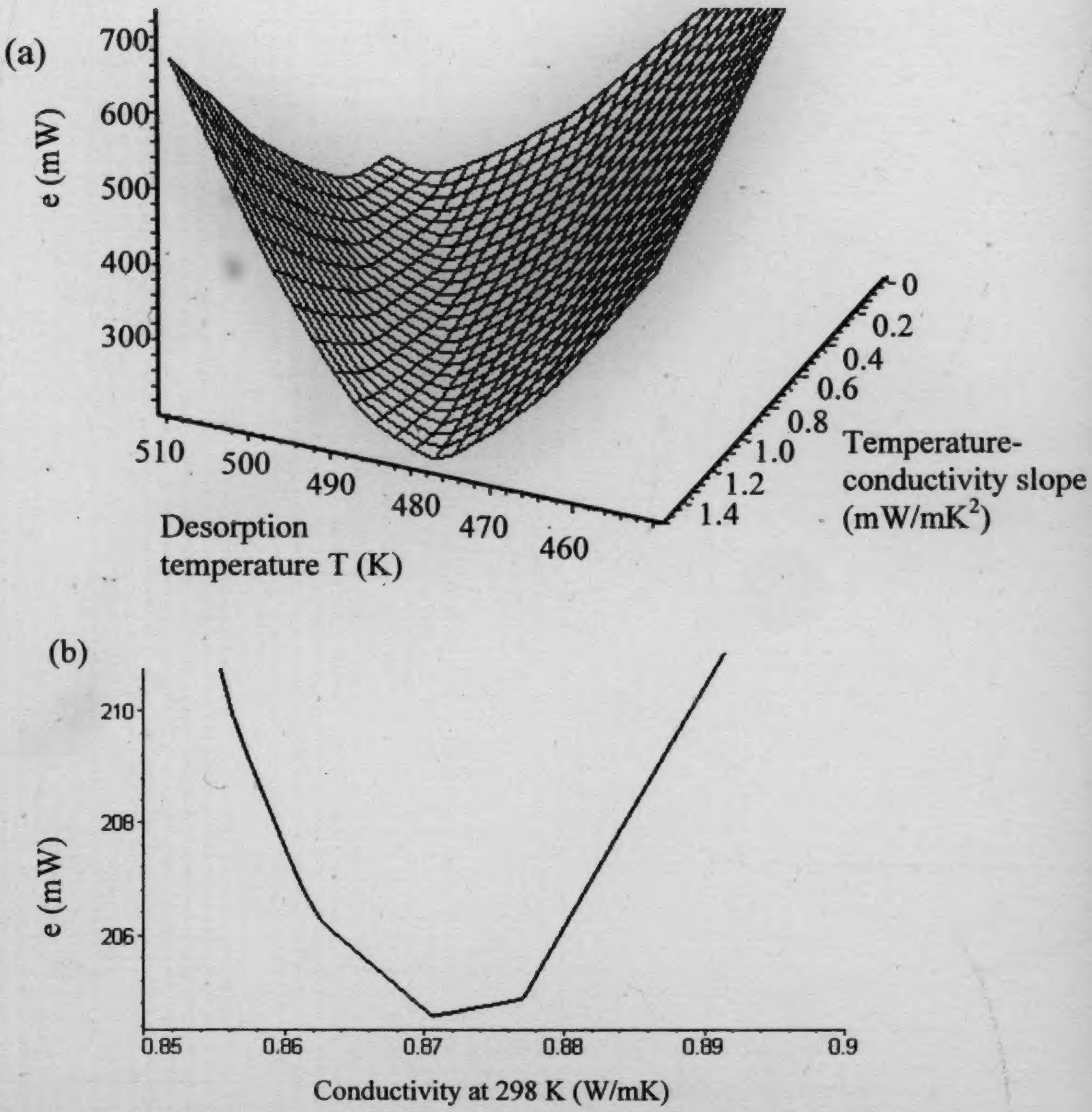

Figure 2-10. (a) The *e* versus desorption temperature of 1-hexadecanethiol SAM from gold and the substrate conductivity-temperature slope. The figure shows there is not a single minimum, but there exist a minimum line. The conductivity at 298 K is assumed to be 0.872 W/mK. (b) The *e* function versus the substrate conductivity at 298 K. The figure shows the conductivity at 298 K that results in best fit of theoretical predictions versus experimental results. The conductivity-temperature slope is assumed to be 0.68 mW/mK^2 and the desorption temperature is assumed to be 488 K.

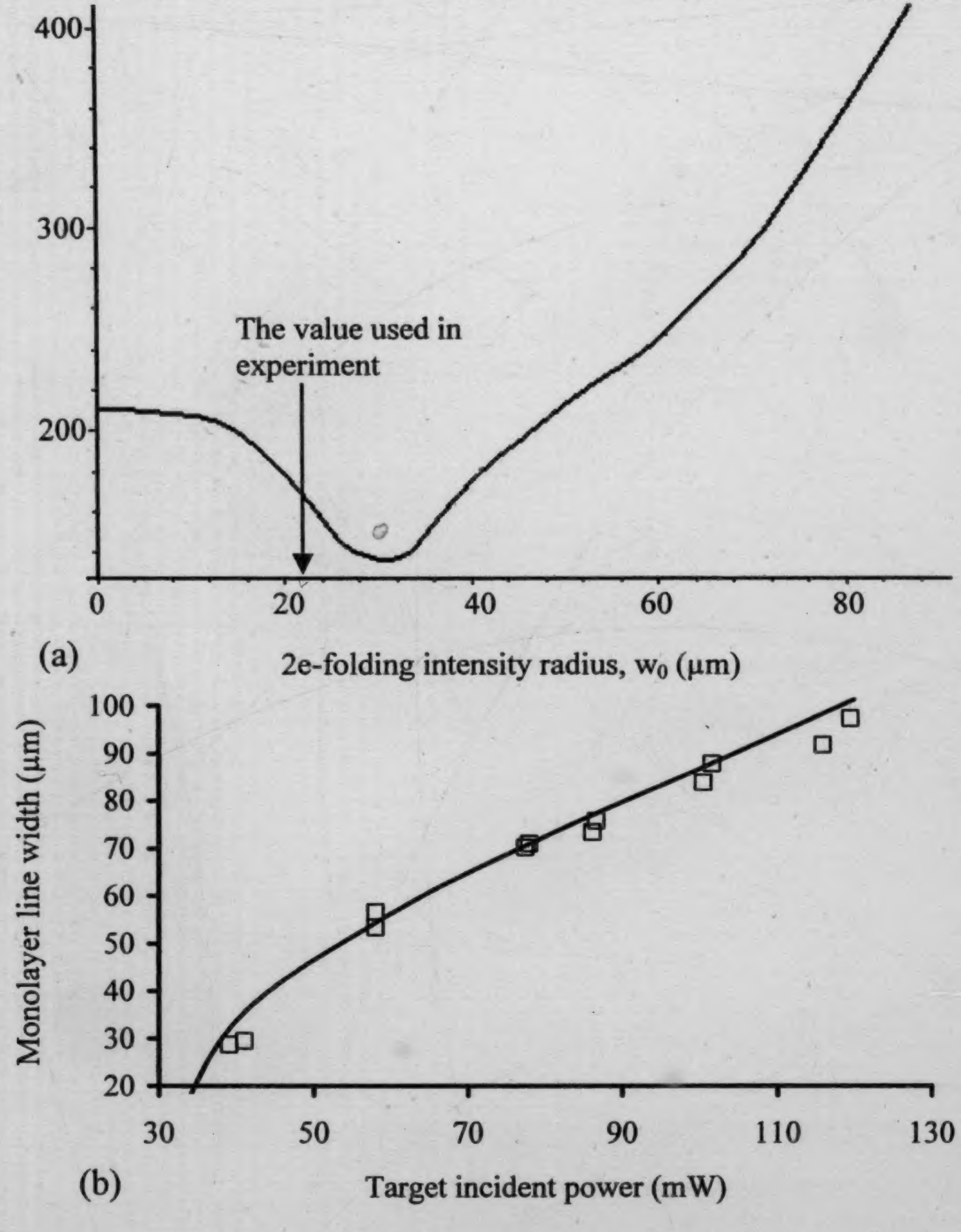

Figure 2-11. (a) Variation of *e* with respect to beam waist when the +10 cm lens is used keeping desorption temperature (488 K) and substrate thermal properties fixed. (b) The line width-incident power diagram when the optimum value of the beam waist is used in calculations.

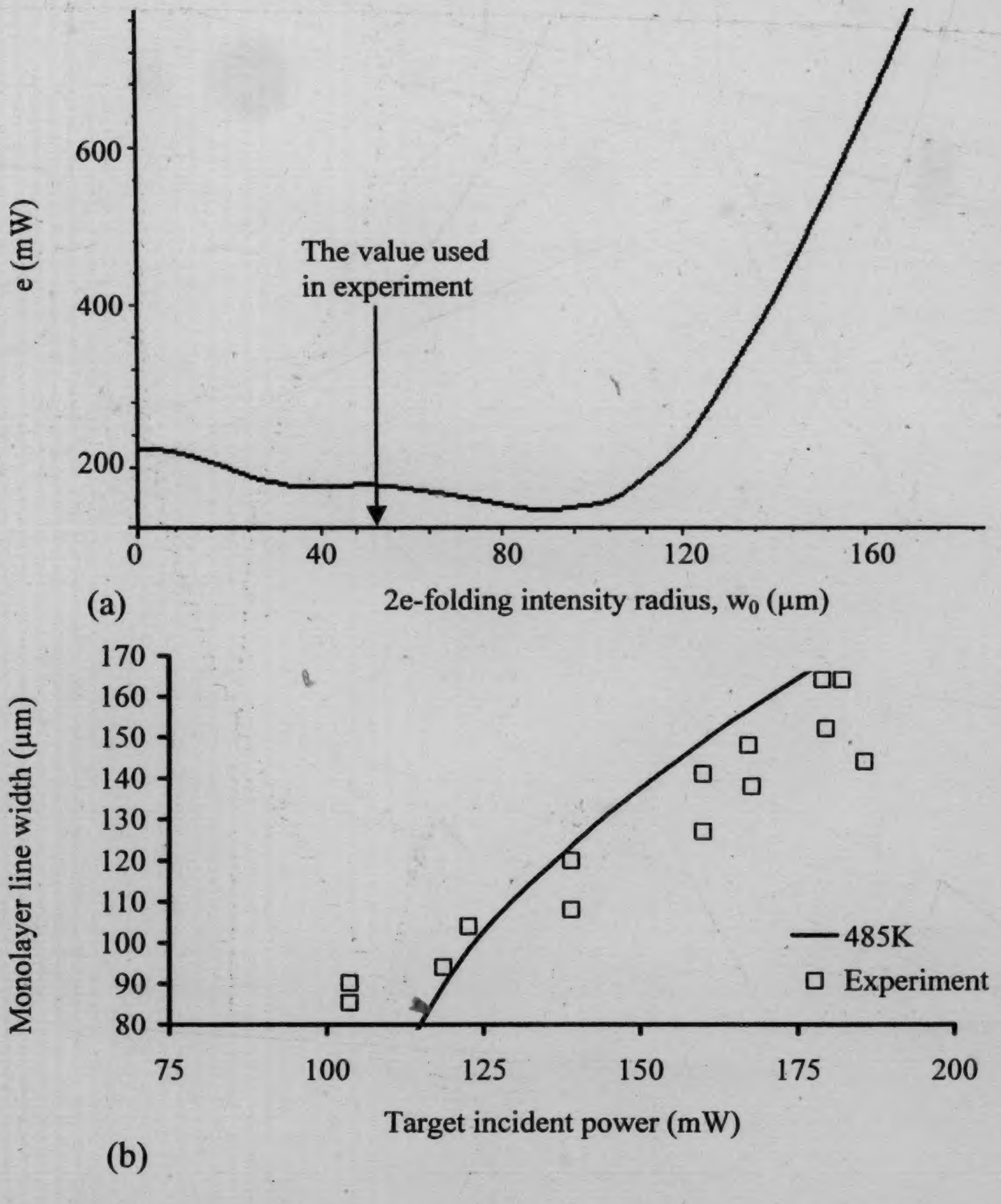

Figure 2-12. (a) Variation of *e* with respect to beam waist where the +25 cm lens is used keeping desorption temperature (488 K) and substrate thermal properties fixed. (b) The line width-incident power using the optimum value of the beam waist radius.

References

(1) Schreiber, F. *Prog. Surf. Sci.* **2000,** *65*, 151-256.

(2) Bain, C.D.; Evall, J.; Whitesides, G.M. *J. Am. Chem. Soc.* **1989,** *111*, 7155-7164.

(3) Nuzzo, R.G.; Dubois, L.H.; Allara D.L. *J. Am. Chem. Soc.* **1990,** *112*, 558-569.

(4) Zhao, X.; Wilbur, J.L.; Whitesides, G.M. *Langmuir* **1996,** *12*, 3257-3264.

(5) Yang, Z.; Frey, W.; Oliver, T.; Chilkoti, A. *Langmuir* **2000,** *16*, 1751-1758.

(6) Nishida, N.; Hara, M; Sasabe, H.; Knoll, W. *Jpn. J. Appl. Phys.* **1996,** *35*, 799-802.

(7) Kawasaki, M.; Sato, T.; Tanaka, T.; Takao, K. *Langmuir* **2000,** *16*, 1761-1728.

(8) Abbott, N.L.; Folkers, J.P.; Whitesides, G.M. *Science* **1992,** *257*, 1380-1382.

(9) Lopez, G.P.; Biebuyck, H.A.; Frisbie, C.D.; Whitesides, G.M. *Science* **1993,** *260*, 647-649.

(10) Dulcey, C.S.; Georger, J.H., Jr.; Krauthamer, V.; Stenger, D.A.; Fare, T.L.; Calvert, J.M. *Science* **1991,** *252*, 551-554.

(11) Kumar, A.; Whitesides, G.M. *Appl. Phys. Lett.* **1993,** *63*, 2002-2004.

(12) Tender, L.M.; Worley, R.L.; Fan, H.; Lopez, G.P. *Langmuir* **1996,** *12*, 5515-5518.

(13) Hong, S.; Mirkin, C.A. *Science* **2000,** *288*, 1808-1811.

(14) Friebel, S.; Aizenberg, J.; Abad, S.; Wiltzius, P. *Appl. Phys. Lett.* **2000,** *77*, 2406-2408.

(15) Takehara, K.; Yamada, S.; Ide, Y. *J. Electroanal. Chem.* **1992**, *333*, 339-344.

(16) Gad-el-Hak, M. *The MEMS Handbook*; CRC Press: Boca Raton, 2002; Chapter 10.

(17) Kirkwood, S.E.; Shadnam, M.R.; Fedosejevs, R.; Amirfazli, A. *Proceedings of the Int. Conference on MEMS, NANO and Smart Systems*; Banff, Canada, IEEE Publication: Los Angeles, 2003, pp 48-52.

(18) Boyd, I. W. *Laser Processing of Thin Films and Microstructures: Oxidation, Deposition, and Etching of Insulators*; Springer-Verlag: New York, 1987; Chapters 1, 2.

(19) Schlenoff, J. B.; Li, M.; Ly, H. *J. Am. Chem. Soc.* **1995**, *117*, 12528-12536.

(20) Nuzzo, R.G.; Fusco, F.A.; Allara, D.L. *J. Am. Chem. Soc.* **1987**, *109*, 2358-2368.

(21) Venkataramanan, M.; Pradeep, T. *Anal. Chem.* **2000**, *72*, 5852-5856.

(22) Sardarli, A. *Private Communications*, 2003.

(23) Qiu, T.Q.; Tien, C.L. *Int. J. Heat Mass Transfer* **1992**, *35*, 719-725.

(24) Schneider, P.J. *Conduction Heat Transfer*, Addison-Wesley: Cambridge, 1957; Chapter 1.

(25) Goldsmith, A.; Waterman, T.E.; Hirschhorn, H.J. *Handbook of Thermophysical Properties of Solid Materials*; Macmillan: New York, 1961; Vol. 3, pp 739-740.

(26) Ordal, M.A.; Long, L.L.; Bell, R.J.; Bell, S.E.; Bell, R.R.; Alexander, R.W., Jr.; Ward, C.A. *Appl. Optics* **1983**, *22*, 1099-1119.

(27) Hall, C.W. *Laws and Models: Science, Engineering and Technology*; CRC Press: Boca Raton, 2000; pp. 30-31.

(28) Ferrieu, F.; Auvert, G. *J. Appl. Phys.* **1983**, *54*, 2646-2649.

(29) Lax, M. *J. Appl. Phys.* **1977**, *48*, 3919-3924.

(30) Burgener, M.L.; Reedy, R.E. *J. Appl. Phys.* **1982**, *53*, 4357-4363.

(31) Diniz Neto, O.O. *Revista De Metalurgica* **1998**, *34*, 148-153.

(32) Huber, M.; Deutschmann, R.A.; Neumann, R.; Brunner, K.; Abstreiter, G. *Appl. Surf. Sci.* **2000**, *168*, 204-207.

(33) Lax, M. *Appl. Phys. Lett.* **1978**, *33*, 786-788.

(34) Moody, J.E.; Hendel, R.H. *J. Appl. Phys.* **1982**, *53*, 4364-4371.

(35) Araki, N.; Sasahara, Y. *Proceedings of the 22nd National Heat Transfer Symposium of Japan*; Tokyo, 1985.

(36) Kakiuchi, T.; Sato, K.; Iida, M.; Hobara, D.; Imabayashi, S.; Niki, K. *Langmuir* **2000**, *16*, 7238-7244.

(37) Schvan, P.; Thomas, R.E. *J. Appl. Phys.* **1985**, *57*, 4738-4741.

(38) Beck, J.V.; Blackwell, B.; Clair, C.R. ST., Jr. *Inverse Heat Conduction: Ill-posed Problem*; John Wiley-Interscience: New York, 1985; Chapters 1,2.

(39) Imen, K.; Lin, J.Y.; Allen, S.D. *J. Appl. Phys.* **1989**, *66*, 488-491.

(40) Goldsmith, A.; Waterman, T.E.; Hirschhorn, H.J. *Handbook of Thermophysical Properties of Solid Materials*; Macmillan: New York, 1961; Vol. 1, p 313.

(41) Tzou, D.Y.; Li, J. *Int. J. Heat Mass Tran.* **1993**, *36*, 3887-3895.

(42) Garg, N.; Carrasquillo-molina, E.; Lee, T.R. *Langmuir* **2002**, *18*, 2717-2726.

(43) Delamarche, E.; Michel, B.; Kang, H.; Gerber, C. *Langmuir* **1994**, *10*, 4103-4108.

(44) Karpovich, D.S.; Blanchard, G.J. (1994). *Langmuir* **1994**, *10*, 3315-3322.

(45) Van den Brink, J.P.; Rongen, M.H.M. *Therm. Conduct.* **1994**, *22*, 70-79.

(46) Kiyohashi, H.; Hayakawa, N.; Aratani, S.; Masuda, H. *High Temperature-High Pressures* **2002**, *34*, 167-176.

(47) Kuriyama, M.; Katayama, K.; Taguma, Y.; Hasegawa, Y. *Trans. Japan Soc. of Mech. Eng. B* **1975**, *41*, 3588-3595.

(48) Ratcliffe, E. H. *Glass Tech.* **1963**, *4*, 113-128.

Chapter 3- Thermo-Kinetics Study of Laser Induced Desorption of Self Assembled Monolayer from Gold: Case of Laser Micropatterning[*]

Introduction

Alkanethiol molecules ($HS(CH_2)_nX$, where X can be any of CH_3, COOH, NH_2, etc.) can spontaneously chemisorb on a gold surface from solution to make a well-organized monomolecular layer called a self assembled monolayer (SAM) (see inset of Fig. 3-1). The potential of SAMs to alter surface properties has been exploited to make patterned surfaces (see [1] for a review and also [2]). The thiol molecules are desorbed when the surface experiences elevated temperatures for a suitable time period.[3] In this paper the laser induced thermal desorption of SAMs is considered within the context of a recently developed methodology called "direct laser patterning of SAMs".[2] Direct laser patterning of SAMs uses a focused laser beam to thermally desorb thiol molecules in areas of interest on the surface and then backfills the bare regions with a second thiol that has a different tail group in order to engineer micropatterned surfaces (Fig. 3-1). We used a scanning laser beam (the 488 nm line of Argon ion laser) to desorb a 1-hexadecanethiol SAM (HDT), $HS(CH_2)_{15}CH_3$, from the gold substrate along a straight line and then backfilled the bare regions with 16-mercaptohexadecanoic acid SAM (MHA), $HS(CH_2)_{15}COOH$. A SAM of HDT makes the surface hydrophobic because of its methyl tail group, whereas a SAM of MHA makes the surface hydrophilic because of its carboxylic acid tail group. In this way, a hydrophilic pattern on a hydrophobic background was generated as a model surface for this study. It is shown that the resulting patterned surface can confine liquid within the hydrophilic pattern and act as a channel without any physical wall.[2] Such a pattern, for instance, can be used in open microfluidics systems for liquid delivery.

---

[*] A version of this chapter has been published. *Shadnam, Kirkwood, Fedosejevs, Amirfazli 2005. The Journal of Physical Chemistry B. 109: 11996-12002.*

In practical applications, e.g. microfluidics, the control of the resulting feature sizes on patterned surfaces is of crucial importance. In order to understand how the feature sizes can be controlled, consideration of the underlying chemical processes that entails formation of features is necessary. It is shown that high temperatures can accelerate the SAM desorption reaction.[3,4] To comprehensively understand the final SAM composition on surface in the laser patterning method, a thermal model, which determines the surface temperature field, should be combined with a kinetics model, which describes SAM desorption reaction. In this direction, results of a previously developed thermal model that predicts surface temperature field[2] is coupled with a kinetics model for SAM desorption reaction. The resulting model is used to calculate the final composition and feature sizes produced in the laser patterning methodology. This allows one to predict properties (e.g. wetting) of the resulting processed surface and helps in selecting the heating parameters (e.g. laser power, scanning speed) to obtain surface features of desired properties and quality.

There is little information in the literature to date regarding the quantitative aspects of patterning, e.g. how to control patterning parameters to achieve a particular feature size, edge quality and cross sectional profile of the resulting patterns.[5] Often only feature sizes are reported as a measure for effectiveness of patterning methods. The exception can be considered the very recent predictive model and kinetic study of laser deposition patterning methodology[6,7] (in contrast to laser desorption methodology, which is presented here). The detailed SAM coverage profiles on surfaces can be used to define edge quality in terms of cross sectional surface concentration of SAMs. The present investigation is a step towards the quantitative study of edge resolution and feature sizes in terms of the chemical composition and properties of patterned surfaces In particular, the specific case of wetting is considered here as it relates to open microfluidics systems.

Procedure

The substrates used for making SAMs were thin films of gold supported on glass microscope slides from Fisher Scientific Co. (Erie Electroverre). Substrates were prepared by sequentially sputtering a 50 Å titanium adhesion layer and a 300 Å gold film layer in an ultra-high vacuum chamber on a carefully cleaned microscope glass slides (see ref 2 and 8 for details of sample preparation procedure). The substrates were immediately immersed in 1 mM ethanolic solution of HDT to make a homogeneous SAM on gold (solution deposition). The second step was irradiation of the sample by the focal spot of a continuous wave (CW) laser beam while moving the sample at constant speed (200 μm/s) using a computer controlled translation stage. The SAM was thermally desorbed along straight-line regions. An Argon ion laser beam (488 nm line) with beam waist (2 e-folding intensity radius) of 22 μm at the focal spot was used. The laser beam was focused using a plano-convex +10 cm lens in one set of experiments and a 10X microscope objective in another set. The third step was immersion of the processed sample in 1mM ethanolic solution of MHA. The MHA made a SAM on the resulting bare regions and in this way, a straight line hydrophilic pattern on a hydrophobic background was made. Further details of the optical setup used and the procedure for direct laser patterning of SAMs can be found elsewhere.[2]

The patterned surfaces were examined using both SEM and optical microscope imaging (before and after backfilling with the MHA). The SEM images provided direct information on the relative surface coverage of HDT and MHA. Lopez et al.[9] have shown that the contrast in SEM images (see Fig. 3-2) can be used to distinguish HDT and MHA SAMs on a gold surface. To quantify the experimental SEM results, the SEM images were post processed to extract pixel intensity values. Similar method for quantitative determination of surface coverage of surface by nanoparticles through post processing of SEM images has been reported.[10,11] In order to extract pixel values, each line-shaped feature in SEM images was scanned across 5 to 10 lines (see the dotted line in the inset of Figs. 3-3 to 3-5). Each scanned line was a pixel wide (i.e. 2.09 μm-wide). The scan lines were separated by no more than a few pixels for each SEM image to collect statistical information about contrast variation profile. Using the intensity tool in SigmaScan 5 software (Systat software Inc.) pixel intensities for each scan across the line feature were recorded and used to produce pixel intensity profiles. The resulting pixel intensity profiles are averaged and normalized with respect to the average pixel intensity of the MHA covered region (dark region in SEM images); see symbols in Figs. 3-3 to 3-5. The error bars in Figs. 3-3 to 3-5 represent the standard deviation of intensity values based on the multiple lines across the line feature in a SEM image.

To investigate the wetting properties of the surfaces, the samples were imaged through optical microscopy within one day of the experiments. Placing a small drop of tridecane from a syringe, and dragging the drop along the hydrophilic lines produced fluidic lines. The liquid was confined to the MHA monolayer regions (without any physical barrier) and as such pattern line width was measured using the image of the fluidic lines under the optical microscope. The measured value corresponds to the full visible width of the line.

Experimental Results

The SEM contrast images are used to determine the feature size (line width) and the surface composition. Results of measurement of the resulting line profiles for various laser powers applied are presented in this section.

Lopez et al.[9] investigated the effect of tail group and free energy of surface on contrast in SEM images of SAMs; they reported that SEM is able to form images of patterns of SAMs on gold and the contrast in SEM images is sensitive to the structures of the components and compositions of the SAMs. The contrast in the SEM images shown in Fig. 3-2 indicates the presence of different SAMs on the surface. Thus, in Fig. 3-2 the resulting contrast suggests that the initial HDT SAM was desorbed and was successfully substituted with a MHA SAM. Narrow transition regions are observed in Figs. 3-3 and 3-4. At lower powers the narrow transition region disappears. It was also observed that feature sizes became wider as samples were irradiated with higher incident laser powers (see Fig. 3-2). The border separating the dark feature and the light background is sharp; but it is not an ideal step. Results of our theoretical modeling (presented in next section) suggests that the transition area in between the dark and light regions in Figs. 3-3 to 3-5 is result of partial desorption of HDT and subsequent backfill with MHA.

The results presented in this section demonstrated successful patterning of SAMs on gold using a laser beam and provided information suggesting gradual change of contrast near edges. A suitable mathematical model to describe the experimental results and to predict the outcome of patterning was constructed and is presented in the next section.

Thermal-Kinetic Model for SAM Desorption

Temperature accelerates the thermal desorption of SAM and thus controls resulting feature sizes.[3,4] A thermal model is used for prediction of the temperature history of individual points on surface of the sample, which is needed in calculation of time dependent instantaneous desorption rates. The resulting temperature profiles are used in a chemical kinetics model (Eyring)[12] that takes into account the rate of SAM desorption at different temperatures. Literature values for the parameters involved in the kinetics model are used. The combined governing equation is integrated in order to find the fraction of SAM desorbed from the surface as result of laser heating (see below).

The influence of heat induced strain rate on heat conduction is neglected, i.e. the material is assumed to be a rigid heat conductor. Thus, the heat diffusion equation does not need to be coupled with elasticity equations.[13] The governing heat equation is derived from the classical Fourier diffusion equation adapted for a moving source heating as:[14]

$$\nabla\cdot\left(\kappa(T)\cdot\nabla T\right)+\frac{2PA(T)}{\pi w_0^2}exp\left(-2\frac{(x-vt)^2+(y-y_0)^2}{w_0^2}\right)\delta(z)=\frac{\kappa(T)}{D(T)}\cdot\frac{dT}{dt} \tag{1}$$

where κ, D, T and t represent the sample thermal conductivity, thermal diffusivity, temperature, and time, respectively; P, w_0, v, and A represent the laser power, 2 e-folding intensity radius of the laser beam, the speed of the sample movement relative to the laser spot, and the optical absorption percentage of the sample, respectively. In Eq. 1, x, y, z denote stationary coordinates and d/dt is the time derivative. The following initial and boundary conditions were adopted:

$$\begin{aligned} &T(t\rightarrow 0)=T_0\\ &T(r\rightarrow \infty)=T_0 \end{aligned} \tag{2}$$

where r represents radius in standard spherical coordinate system and T_0 is ambient (initial) temperature.

Since the diameter of the laser spot is of the order of tens of micrometers whereas the length and width of the sample are of the order of centimeters, the substrate is assumed physically infinite in x and y directions and edge effects on the local thermal field around the heating spot are neglected.[15] The model simplifies to an infinite substrate in the x and y directions. It is argued that because of the low thickness and high conductivity of the metallic layer relative to the glass, the thermal properties of the glass are dominated.[2,16,17] The thermal properties used in calculations are those of soda lime microscope slides from

Fisher Scientific. The values for all parameters needed to calculate the temperature profiles using Eq. 1, are given in Table 3-1.

To determine the mathematical form of the heat source function, an analysis of laser absorption as it penetrates into the substrate was needed. The fractions of the energy absorbed in different layers (gold, titanium and glass) were considered and it was concluded that more than 99% of the absorption occurs at the gold layer.[2] It is assumed for this study that the absorbed energy is fully delivered to the gold layer. The Dirac delta function on the left hand side of Eq. 1 signifies this assumption.

Within the Rayleigh range, the beam waist, w_0, will be a sufficiently slowly varying function of depth, that w_0 is treated as a constant in Eq. 1.[18] The temperature dependence of optical absorption is neglected by noting that at 488 nm, the temperature dependence is typically small for most metals before melting and that the maximum temperature coefficient of reflectivity for gold is of the order of 10^{-5} K^{-1} between 200 to 700 nm.[19] It is also shown that temperature dependence of sample thermal diffusivity can be neglected.[2]

The governing differential equation (Eq. 1) is nonlinear due to the temperature dependence of the thermal properties of the sample, i.e. thermal conductivity; it is argued that thermal diffusivity and absorption coefficient does not vary significantly within range of temperatures relevant to laser patterning technique.[2] In the calculations, a linear increase of conductivity with temperature at a slope of 0.68 mW/mK^2 was used as this was a characteristic of the soda lime glass used.[2] The above mentioned assumptions and a

Kirchhoff transformation[20] simplifies Eq. 1 to a linear partial differential equation. Since the exposed surface of the sample was assumed to be adiabatically insulated, the solution of the above problem is simply double the solution for the case of a moving Gaussian source in full space. Also, the temperature is required to be finite at the origin.

The desorption of SAMs from a gold surface during the first few minutes in nonpolar liquids is shown to adopt a first order kinetics, i.e. the rate of desorption is proportional to the surface concentration of SAMs: [3,4,21]

$$\frac{dC}{dt} = -k.C \tag{3}$$

where C denotes surface concentration of SAM, and, k is the proportionality factor (also called rate constant). The rate constant, k, is a temperature enhanced factor according to the Eyring equation,[10]

$$k = \frac{k_B T(x,y,t)}{h} \exp\left(-\frac{\Delta G}{RT(x,y,t)}\right) \tag{4}$$

where k_B is the Boltzmann's constant, h is Planck's constant, ΔG is the Gibbs free energy of activation of the SAM desorption reaction, and R is the gas universal constant.

To use the kinetics model, the values of the rate constant at different temperatures were needed. This entails that activation Gibbs energy value is needed. Gibbs energy of SAM desorption from gold substrate in hydrocarbon solvents, specifically isooctane and decalin, at 333-383 K was used from ref [4]. Lee's group[4] showed that there exist two distinguishable desorption kinetic regimes: an initial fast regime followed by a slower regime. Both of the desorption regimes were shown to be temperature enhanced, and within each regime, the rate of desorption is believed to be a function of the molecular structure of the SAM. Since the desorption happens in a few seconds in direct laser patterning of SAMs, the constants of the initial fast regime is relevant to our patterning methodology (heating lasts almost 0.85 s for temperatures of higher than 400 K for heating with a beam of 120 mW traveling at 200 μm/s; for lower powers this residency time is even shorter). The standard activation free energies for desorption of long chain alkanethiol monolayers in decalin were shown to be 27 ± 1 Kcal/mol at 298 K during the fast desorption regime.[4] The desorption activation enthalpy and entropy was shown to be 28 Kcal/mol and 8 Kcal/mol.K, respectively, for HDT during the fast desorption regime in decalin.[4] The activation enthalpy for HDT in isooctane was reported to be 30.9 Kcal/mol, which is not far from the associate value for decalin (28 Kcal/mol).[4] The closeness of the SAM desorption activation energies in decalin and isooctane may be interpreted that as far as the SAM desorption occurs in nonpolar media, the activation energetics of desorption does not change much (compare to much slower desorption rates that is reported in ref [21] for desorption in aqueous solutions). We assumed that the Gibbs activation energy for SAM desorption in nonpolar gaseous media is of the same order of magnitude as Gibbs activation energy for SAM desorption in nonpolar liquid media. This was necessary since no quantitative information dealing with desorption of thiols in a gaseous medium under atmospheric pressure, which is relevant to our laser patterning experiments, can be found in the literature. Thus, the quantitative data obtained from studies in nonpolar liquid medium was used as an approximation for values in gaseous medium. However, the data related to energetics of desorption in liquid solvent medium should be extended to gas medium with care because the thiol molecules may have significant interactions with solvent molecules. Furthermore, since there is no evidence yet reported for a mechanistic change in SAM desorption reaction at temperatures beyond those examined by Garg et al.,[4] we assumed that mechanism of desorption remained the same at elevated temperatures as well. Thus, the activation Gibbs free energy reported by Garg et al.[4] is used at all temperatures.

The temperature dependence of the rate constant is determined according to Eq. 4 for a known value of Gibbs activation energy. In order to the find final SAM concentration on a surface, the desorption rate (Eq. 3) is numerically integrated over time taking into account the temperature history at each point. Therefore, the following equation is constructed to relate the SAM desorption kinetics to the thermal model described earlier.

$$C(x,y) = C_0(x,y)\exp\left(-\int_{t_0}^{t_1}\frac{k_B T(x,y,t)}{h}\exp\left(-\frac{\Delta G}{RT(x,y,t)}\right)dt\right) \qquad (5)$$

In the above equation $C_0(x, y)$ represents the initial SAM coverage of the surface, which is assumed to be complete and uniform everywhere (i.e. $C_0(x, y)=1$). In Eq. 5, the temperature in the denominator of the exponential and the coefficient within the integrand come from the results of thermal modeling. In other words, Eq. 1 together with conditions listed (i.e. Eq. 2) give the time dependent temperature each point *(x,y)* experienced during laser heating. The resulting temperature history for each point, $T(x,y,t)$, is used in Eq. 5 to calculate the final SAM coverage on surface. Equation 1 was numerically integrated using the Runge-Kutta algorithm of Maple 8 software. The resulting temperature was substituted into Eq. 5; then, Eq. 5 was also integrated using the Runge-Kutta algorithm of Maple 8 software to obtain the surface chemical composition.

Using the profile of the remaining HDT coverage on surface in Figs. 3-3 to 3-5, one can define theoretical width of the channel at different removal levels (percentages) as shown in Fig. 3-6. For example, it is clear that the width of HDT removal at 20% removal level (denoted by $W_{20\%}$) is narrower than the width of HDT removal at 80% removal level (denoted by $W_{80\%}$). The removal width at different HDT percentages were extracted from the theoretical curves in Figs. 3-3 to 3-5 (and similar graphs for other laser powers, which are not presented in this paper); they are shown in Fig. 3-7 as continuous lines together with experimental line widths measured using fluidic lines[2] and presented using symbols.

Discussion

The calculations combining both heat diffusion and kinetics of SAM desorption equations resulted in theoretically calculated final composition profiles of SAMs on the gold substrate. The effect of laser power on the induced temperature profile and subsequently SAM desorption profile was considered. At each laser power level, the experimentally obtained SEM contrast plots were compared to theoretically calculated SAM coverage profiles. Also, in order to compare the resulting surface chemical compositions with experimental line widths (fluidic lines as explained above) measured using optical microscopy, we relate chemical composition of the surface to the surface wetting properties using results reported by Bain and Whitesides.[22,23]

Figure 3-8 provides insight into how the laser beam energy is distributed on a sample surface to desorb the SAM. It shows that the resulting induced temperature profile (dotted line) is broader than the energy profile of the laser beam (dashed line) in terms of spatial width, which shows the diffusion of heat energy within material (sample). It can also be noted that the width of the SAM removal (solid line in Fig. 3-8) is even broader than the width of the temperature profile (the width of the full desorption region, delimited by the arrows in Fig. 3-8, is almost equal to width of the temperature profile at 0.25 of height); therefore, it can be concluded that approximately 20-25% of the peak temperature is enough for desorption of the monolayer for the given conditions.

The theoretical and experimental profiles were compared for incident laser powers of 73, 49, and 24 mW. In Figs. 3-3 to 3-5, the symbols show normalized SEM pixel intensities averaged over several sections across the straight line feature (normalized intensity values along the dotted lines shown in the inset of Figs. 3-3 to 3-5). The lines in Figs. 3-5 represent the results of the theoretical calculations based on the mathematical model (right axis). There are two lines in each of Figs. 3-3 to 3-5. The theoretical results in each figure (Figs. 3-3 to 3-5) are presented for two laser beam waists in order to discuss the dependence of the results on beam waist: One of the beam waists is the measured value during the experiments (i.e. 22 μm as 2 e-folding intensity radius)[2]; the results associated with this beam waist are presented by solid lines in Figs. 3-3 to 3-5. The other beam waist is 30% larger than the measured beam waist value (i.e. 31 μm as 2 e-folding intensity radius); and the results associated with this beam waist are presented by dashed lines in Figs. 3-3 to 3-5. Complete desorption has happened where HDT coverage is 0 (flat top portion of curves) whereas partial desorption is where the HDT coverage is between 0 and 1 (shoulders of the curves). In Figs. 3-3 to 3-5, it is observed that the theoretical calculations are in good agreement with experimental SEM contrast plots in terms of the width of the partial as well as complete desorption and subsequent filling with MHA. The agreement, with the theoretical predictions based on the measured beam waist, is better at higher laser powers. Considering the theoretical results for the two beam waists in Figs. 3-3 to 3-5, it is clear that at lower laser powers (e.g. 24 mW, Fig. 3-5), keeping other parameters constant, the final SAM composition plots show high sensitivity to beam waist; whereas they do not show such sensitivity at higher powers. It implies that the control of fine feature sizes needs robust control of the laser beam waist and it is an important defining parameter that needs to be controlled quantitatively.

To further strengthen the correlation of SEM pixel intensity plots with surface coverage of SAMs a control experiment using Auger Electron Spectroscopy (AES) was performed. The AES is a surface sensitive method that can provide quantitative elemental analysis for all elements except hydrogen and helium.[22] The AES can be used for quantitative chemical profiling of 2-20 layers of atoms on the surface. The AES involves irradiation of surface with a focused low energy electron beam (~4-10 keV) in a vacuum chamber and analysis of resulting electrons with respect to their energies, making AES capable of identifying elemental composition with sensitivity down to 0.5 atomic percentile. The resulting electrons have discrete kinetic energies that are characteristic of the emitting atoms. Resolution of the AES results used in this study was 300 nm (resolution of AES machines can be as small as 15 nm).

Previous AES studies on SAMs have concluded that absolute intensities of Auger peaks can be used to calculate mole fraction of mixed SAMs on surfaces.[23,24] A number of patterned surfaces were examined using both AES and SEM (Figs. 3-9 to 3-11). The AES provides intensity of oxygen signal along the marked line in the SEM image (see insets). The SEM results were post processed to extract pixel intensities are extracted along a few lines in vicinity of the marked lines. The SEM pixel intensity profiles were averaged and normalized with respect to the average pixel intensity of the MHA covered region (dark region in SEM images). The error bars represent the standard deviation of intensity values based on multiple scanned lines in vicinity of the marked AES line. Good correlation of SEM pixel intensity graphs with AES oxygen plots provide another corroborating reason to show SEM pixel intensities are correlated with surface concentration of SAMs.

Using theoretically predicted composition profiles of SAMs on the gold substrate (i.e. Figs. 3-3 to 3-5), the width of the resulting channel (line width) was calculated at different HDT removal levels for different laser powers. The resulting line widths (solid lines in Fig. 3-7) are compared with the experimentally measured wetted line widths (symbols in Fig. 3-7) under optical microscope using tridecane. Figure 3-7a shows that the experimental line widths (measured based on tridecane confinement on the hydrophilic pattern) lie between $W_{40\%}$ and $W_{80\%}$ theoretical curves. Bain and Whitesides[25,26] have reported contact angle measurements for SAMs containing different fractions of HDT and MHA (mixed SAMs). They have reported the threshold for spread of hexadecane on the mixed SAM surface to be between 30% to 66% of HDT in a mixed HDT and MHA surface. The calculated surface composition threshold for spread of tridecane (i.e. 40% to 80% HDT) overlaps with the range reported by Bain and Whitesides.[25,26] It should be noted that comparison of results of tridecane wetting (i.e. our experiment) with that of hexadecane wetting (i.e. Bain and Whitesides[25,26] experiments) is appropriate, as the liquid-vapor surface tension (γ_{lv}) of hexadecane differs only 0.7% from tridecane; and considering the Young equation, i.e. $\gamma_{lv}\cos\theta = \gamma_{sv} - \gamma_{sl}$, the results from hexadecane can be used as an estimate for that of tridecane.

Using a 31 μm as beam waist, the theoretical HDT removal width at different removal levels (percentages) is presented in Fig. 3-7b. Figure 3-7b shows that the experimental line widths, both at high and low laser powers, lie between $W_{20\%}$ to $W_{60\%}$, which is within the interval Bain and Whiteside[25,26] reported for spread of hexadecane on mixed SAM of HDT and MHA (i.e. between 30% and 66% as fraction of HDT within HDT-MHA mixed SAM). Figure 3-7c shows comparison of line width measurements and theoretical calculations data for a smaller beam waist (8 μm) achieved through focusing the laser beam with a 10X microscope objective. The experimental points are located in the region of $W_{60\%}$ to $W_{80\%}$ theoretical curves. Similar to Fig. 3-7a, at higher powers they are close to 80% HDT and reduce in HDT percentage at lower powers. Comparison of

Fig. 3-7c with Fig. 3-7a shows a small shift of experimental line widths toward higher HDT percentages.

Summary and Conclusions

Laser patterning methodology for SAM on gold surfaces where a laser beam in TEM_{00} mode is scanned along straight lines is analyzed. In this method the laser beam locally heats up the surface and triggers the endothermic reaction of SAM desorption to produce linear patterns. In this paper a comparison between theoretical predictions and experimental observations for the thermal laser patterning of SAMs is presented. Contrast differences in the SEM images of patterned surfaces is used as an indication of SAM coverage on the surface. To theoretically predict the final composition of the surface in terms of fraction of SAM coverage a model was constructed, which combined the temperature history of the surface as a result of laser heating with a model describing kinetics of SAM desorption based on the Eyring equation. The resulting calculated surface chemical composition profiles were compared with experimental results obtained using SEM images. Good agreement of theoretically calculated coverage profiles and experimentally measured contrast plots was observed in terms of line widths. The theoretical chemical composition contours were also related to wetting properties of surface and it was shown that the theoretical predictions were also in agreement with experimental observations of liquid confinement on the surface. The results indicate that width of the resulting lines and their wetting properties can be controlled by changing laser incident power. It is shown that the mathematical model presented can be used to predict feature sizes and chemical composition as well as wetting properties of generated patterns.

Table 3-1. Thermal and process parameters used in solving Eqs. 1 and 5.

κ, Thermal conductivity at 298 K (Erie)	0.872 W/mK
D, Thermal diffusivity (Erie)	0.33 mm^2/s
v, Spot speed (Controlled)	200 μm/s
w_0, 2 e-folding intensity beam radius (focused by +10 cm lens) (Measured)	22 μm
w_0, 2 e-folding intensity beam radius (to show effect of beam size) (Theory)	31 μm
w_0, 2 e-folding intensity beam radius (focused by 10X objective) (Measured)	8 μm
A, Optical absorbance of the sample (Measured)	44%
ΔG, Gibbs free energy of activation of the SAM desorption (from ref 4)	28 kcal/mol

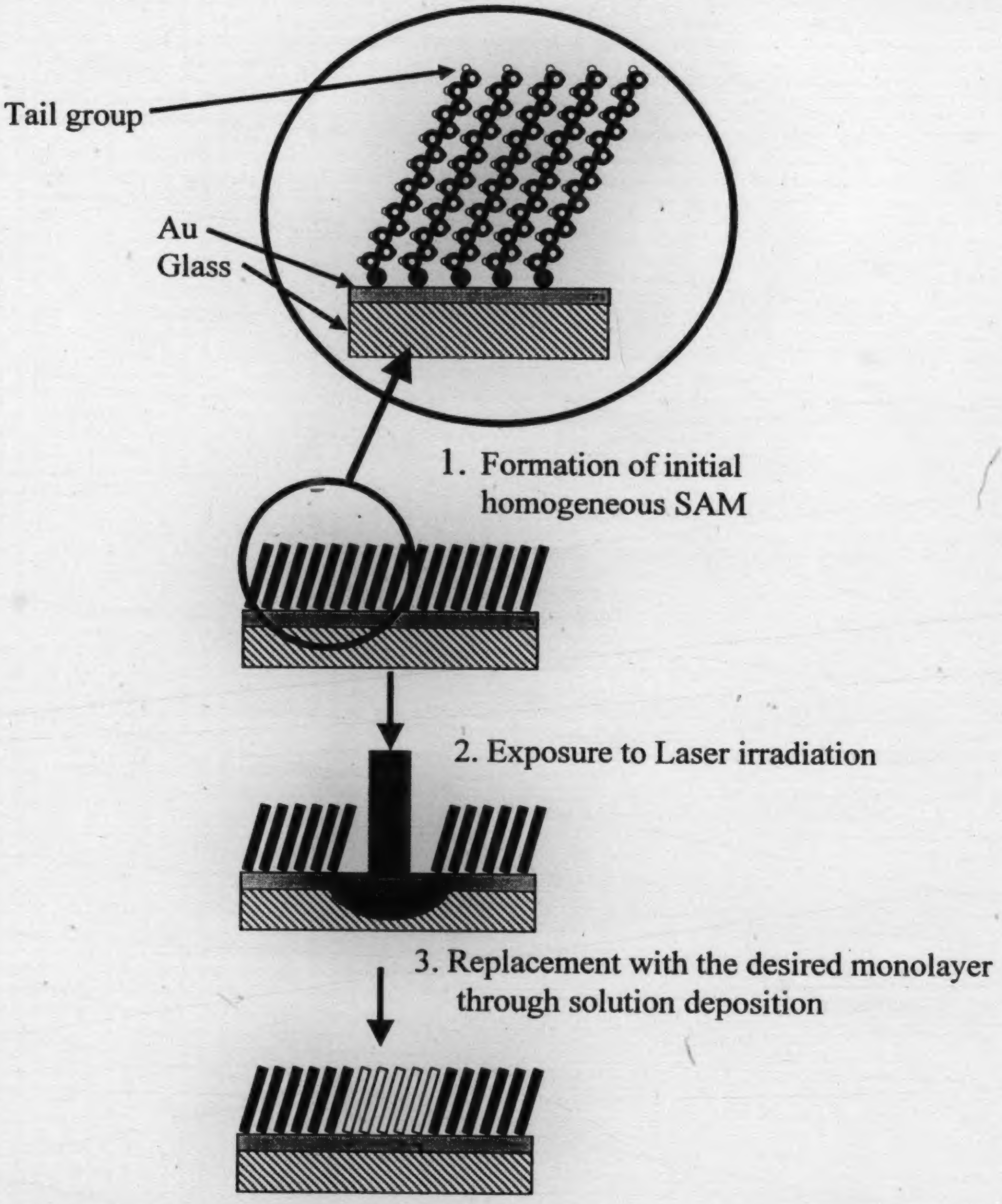
Tail group
Au
Glass
1. Formation of initial homogeneous SAM
2. Exposure to Laser irradiation
3. Replacement with the desired monolayer through solution deposition

Figure 3-1. Steps of direct laser patterning procedure: 1. Initial formation of a homogeneous SAM surface; 2. Subsequent removal of SAM at desired locations by laser heating; 3. Solution deposition of another SAM with different terminal group in the irradiated bare regions. Inset: an enlarged view of self assembled monolayer of 16-carbon alkanethiol molecules chemisorbed to a gold surface.

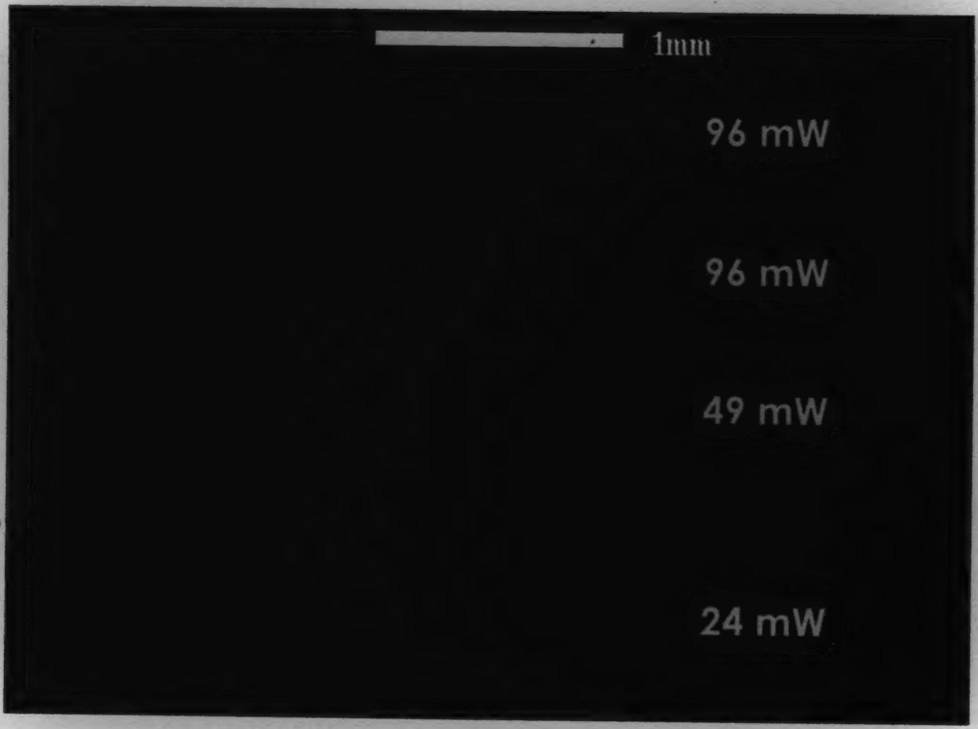

Figure 3-2. The SEM image of a scanned sample at different laser powers. The sample was placed at the focal spot of the laser beam focused by a +10 cm plano-convex lens during the laser heating. The HDT monolayer was desorbed and replaced by the MHA monolayer (formation of dark strips). The HDT monolayer was completely desorbed and replaced by the MHA monolayer in the dark regions. In making SEM images the acceleration voltage was 15.00 kV and the magnification was 15 times.

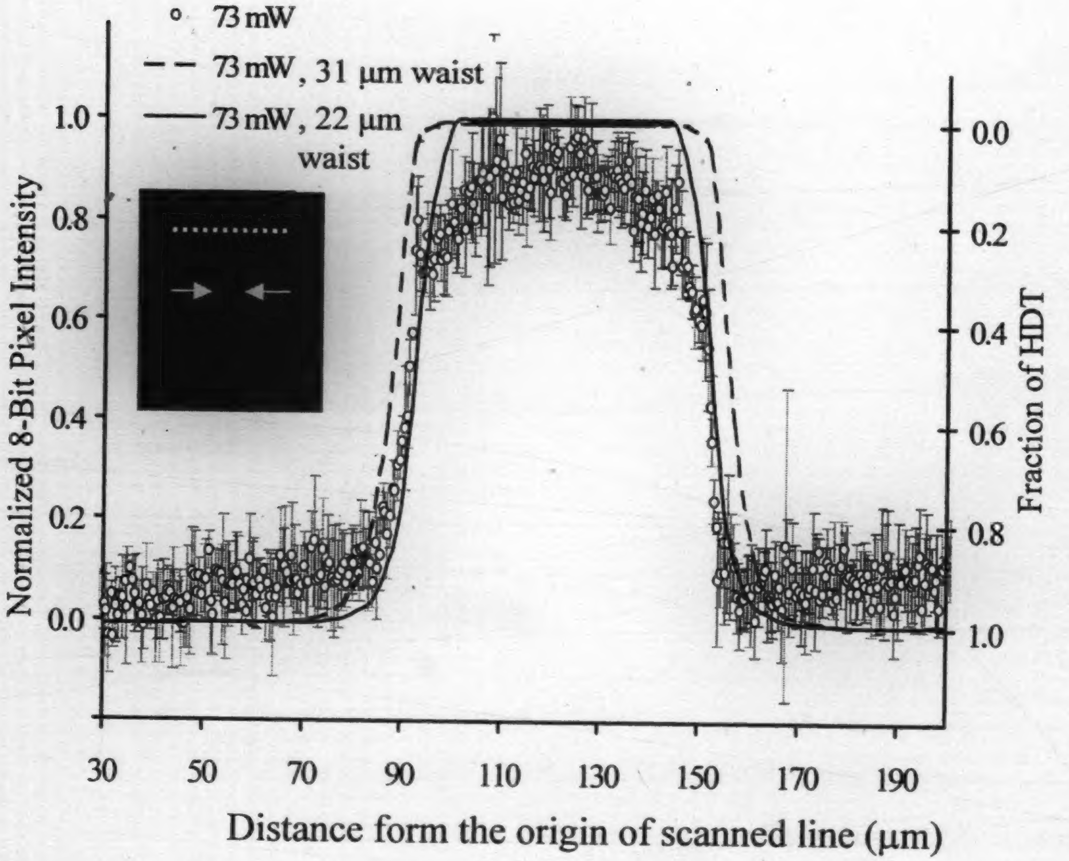

Figure 3-3. The correlation of the contrast plots of SEM image (left axis) with theoretically calculated chemical composition of the surface for incident laser power of 73 mW (right axis). The solid line shows the results of calculations using the measured beam waist (22 µm) and the dashed line shows the results of calculations using a beam waist of 31 µm. The inset shows the SEM image out of which this contrast plot is extracted, through scanning along sections across the line-shaped dark feature (the dotted lines across the feature shown as inset).

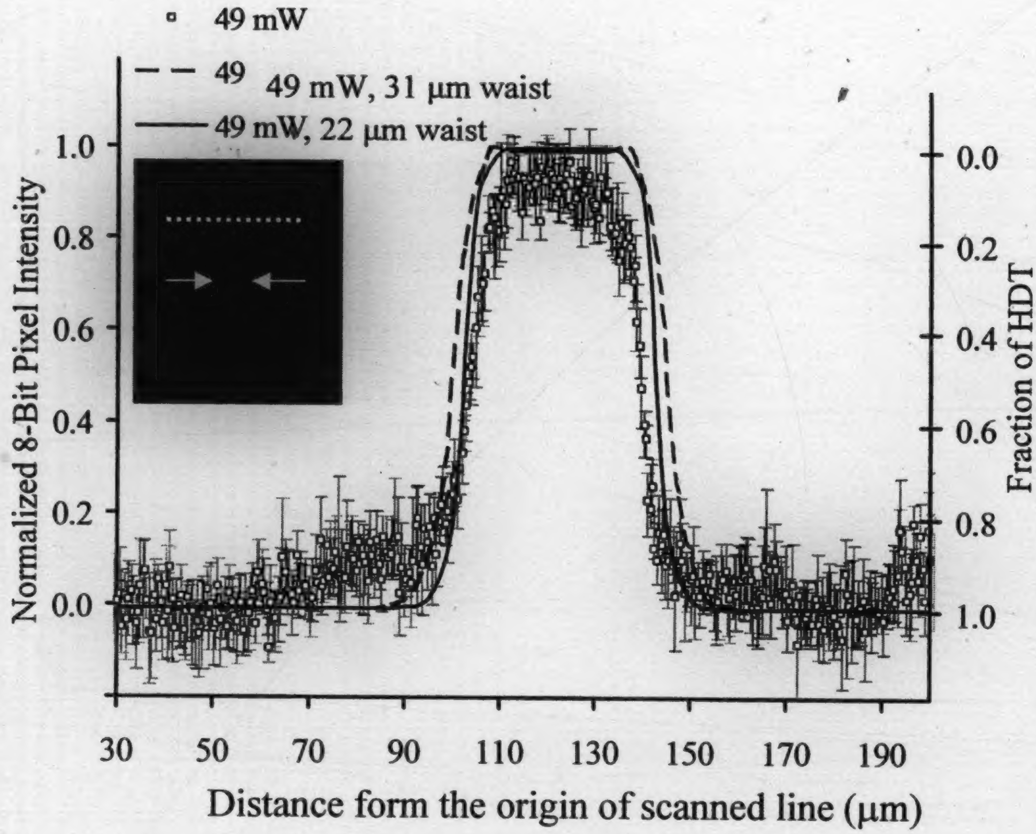

Figure 3-4. The correlation of the contrast plots of SEM image (left axis) with theoretically calculated chemical composition of the surface for incident laser power of 49 mW (right axis). The solid line shows the results of calculations using the measured beam waist (22 μm) and the dashed line shows the results of calculations using a beam waist of 31 μm. The inset shows the SEM image out of which this contrast plot is extracted, through scanning along sections across the line-shaped dark feature (the dotted lines across the feature shown as inset).

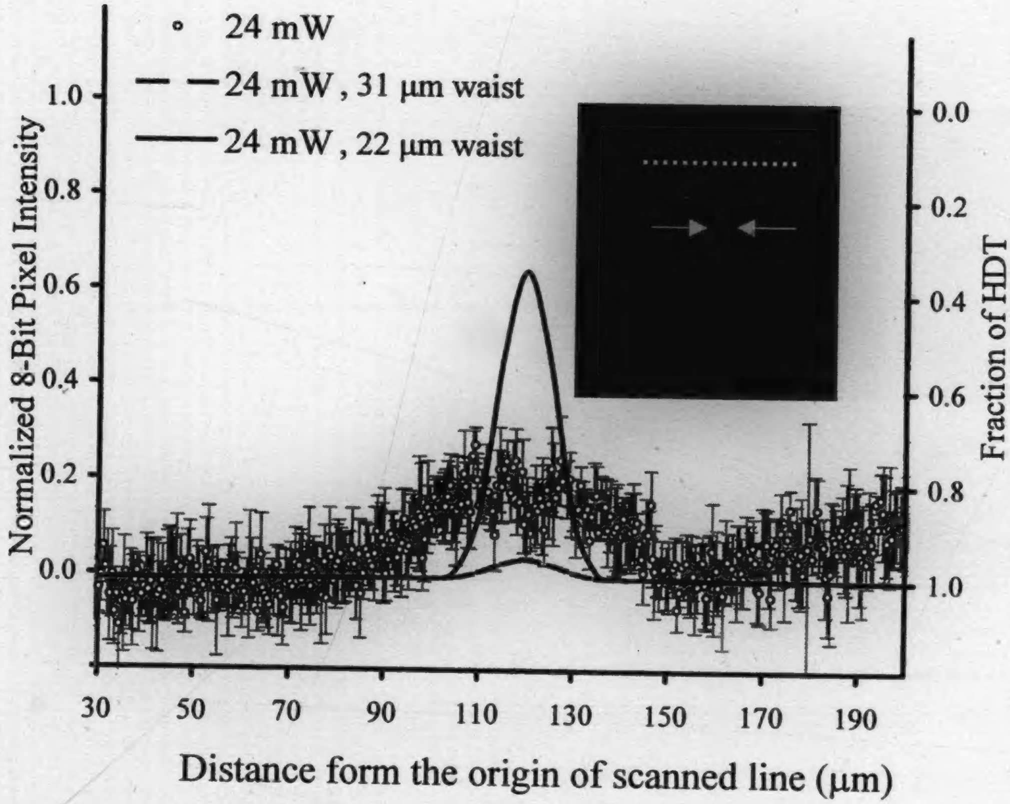

Figure 3-5. The correlation of the contrast plots of SEM image (left axis) with theoretically calculated chemical composition of the surface for incident laser power of 24 mW (right axis). The solid line shows the results of calculations using the measured beam waist (22 μm) and the dashed line shows the results of calculations using a beam waist of 31 μm. The inset shows the SEM image out of which this contrast plot is extracted, through scanning along sections across the line-shaped dark feature (the dotted lines across the feature shown as inset).

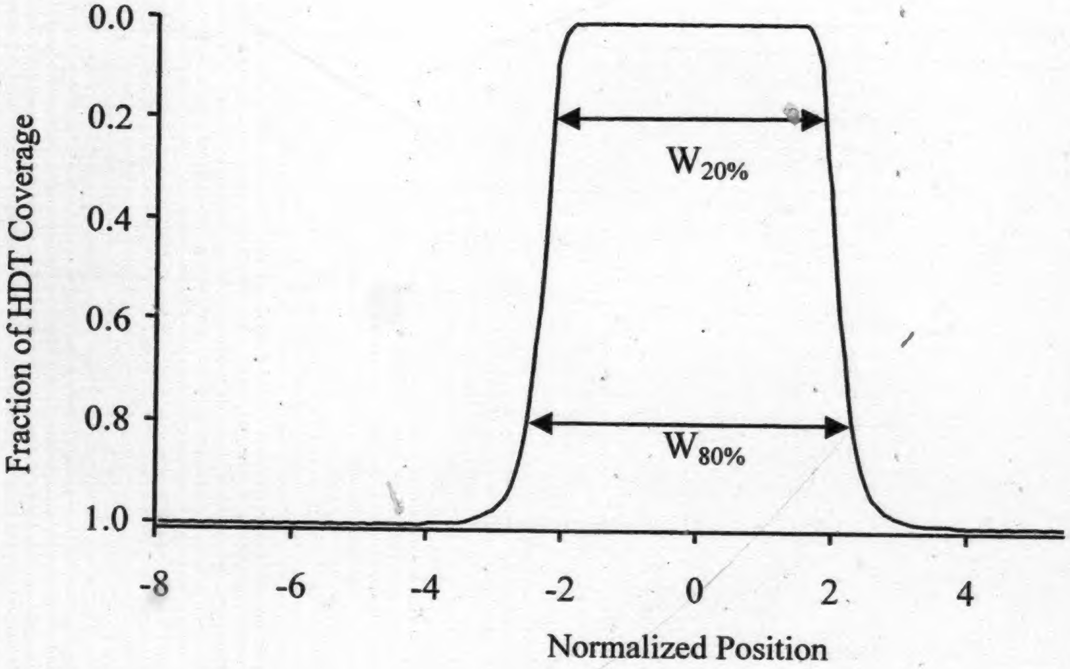

Figure 3-6. The curve shows a schematic final surface coverage of HDT across a section perpendicular to the laser scanning direction. The arrows define the line width at certain fraction of HDT left on the surface. The distances on horizontal axis are normalized to the e-folding radius of the laser beam, and plotted with reference to the centerline of beams scanning path.

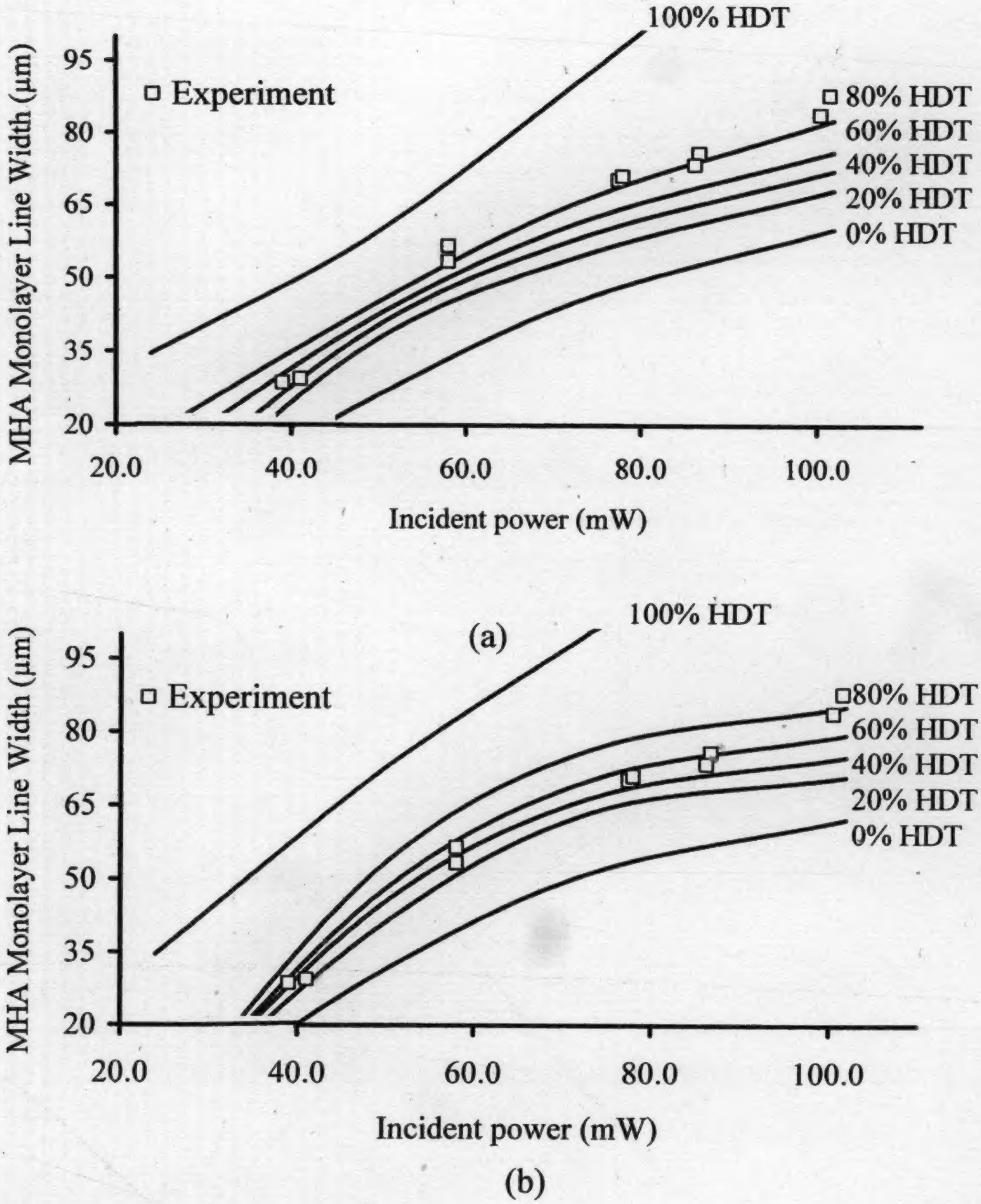

Fig. 3.7 (Continued in next page)

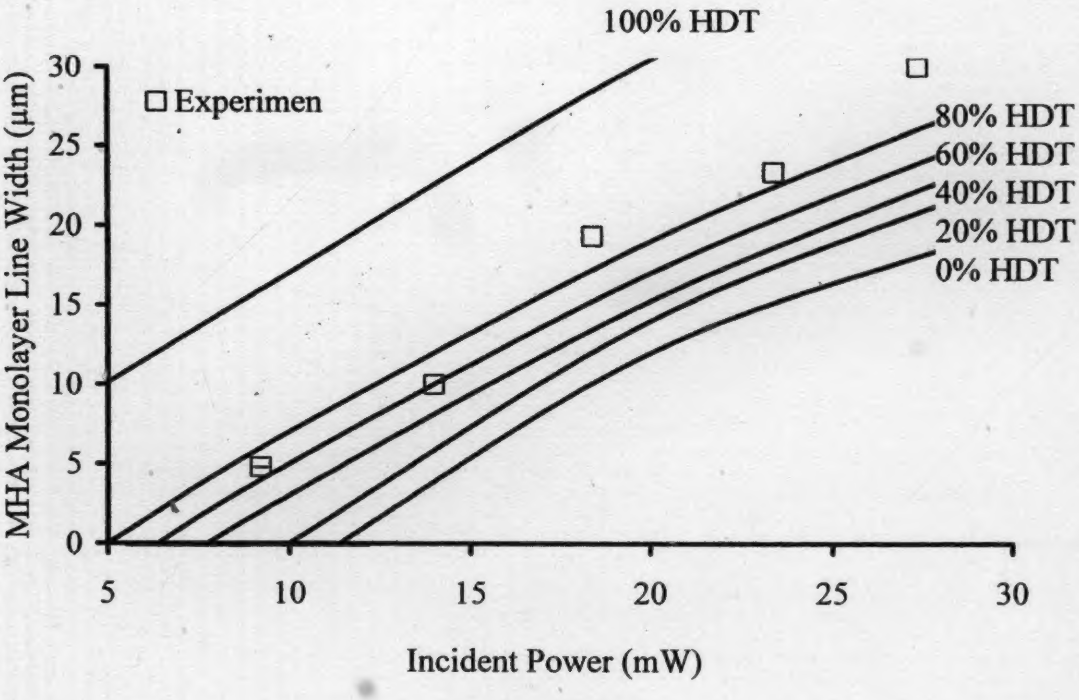

(c)

Figure 3-7. Variation of the replaced monolayer line width with laser power. The symbols represent experimentally measured channel widths using optical microscopy at different laser incident powers. Confinement of a liquid (tridecane) was used to visualize the channel. The lines represent the theoretical modeling results. The theoretical width of the resulting channels is calculated based on calculated final chemical composition profiles of SAMs on the gold surface (see Figs 3-5). (a) The theoretical line width-incident power lines are calculated with the measured value of the beam waist of 22 µm. (b) The theoretical line width-incident power lines are calculated with the beam waist of 31 µm. (c) The theoretical line width-incident power lines are calculated with the measured beam waist of 8 µm.

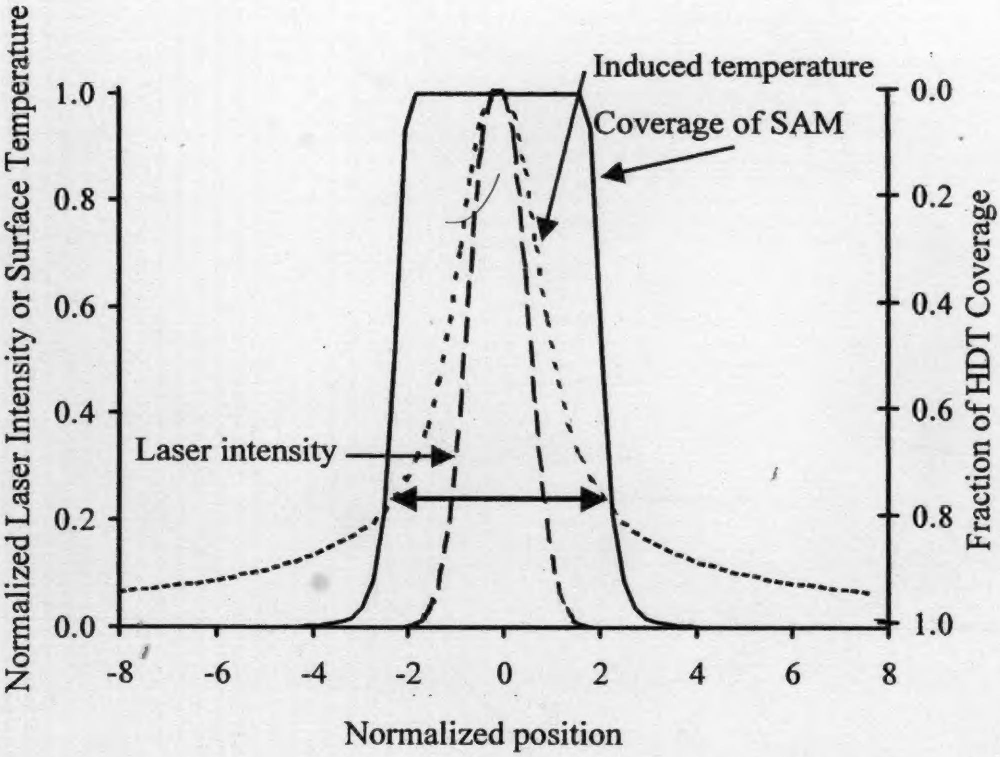

Figure 3-8. The normalized spatial profile of the CW laser beam, the induced temperature, and the final fraction of monolayer desorbed across a typical section perpendicular to the laser scanning direction. The value of each parameter on vertical axis is normalized through dividing by its associated maximum value. The distances on horizontal axis are normalized to the e-folding radius of the laser beam, and plotted with reference to the centerline of beams scanning path. The curve associated with the coverage of SAM has to be cut at zero HDT coverage (sharp corners in above graph) because there is no more SAM left to be desorbed.

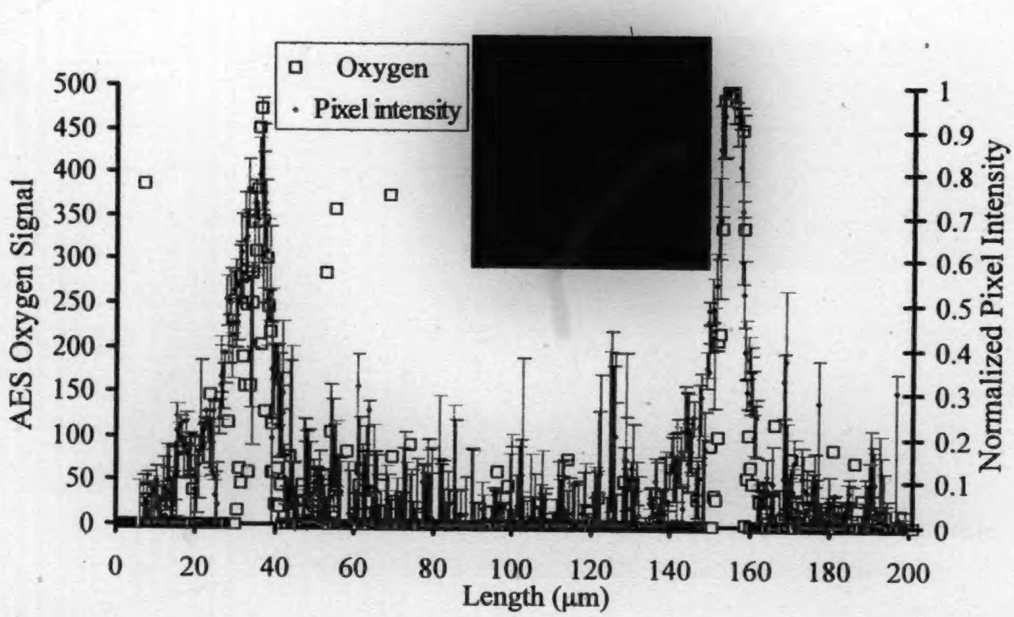

Figure 3-9. Correlation of AES oxygen signal (squares, left axis) with pixel intensity plots of the SEM image (small crystals with error bars, right axis) across two lines (along the line marked in inset). The left line in inset is out of focus and the right one is in focus. Both of them have been made through scanning of a 30 mW laser beam focused with a 10X objective. The inset shows the SEM image out of which this pixel intensity plot is extracted, through scanning along the horizontal line.

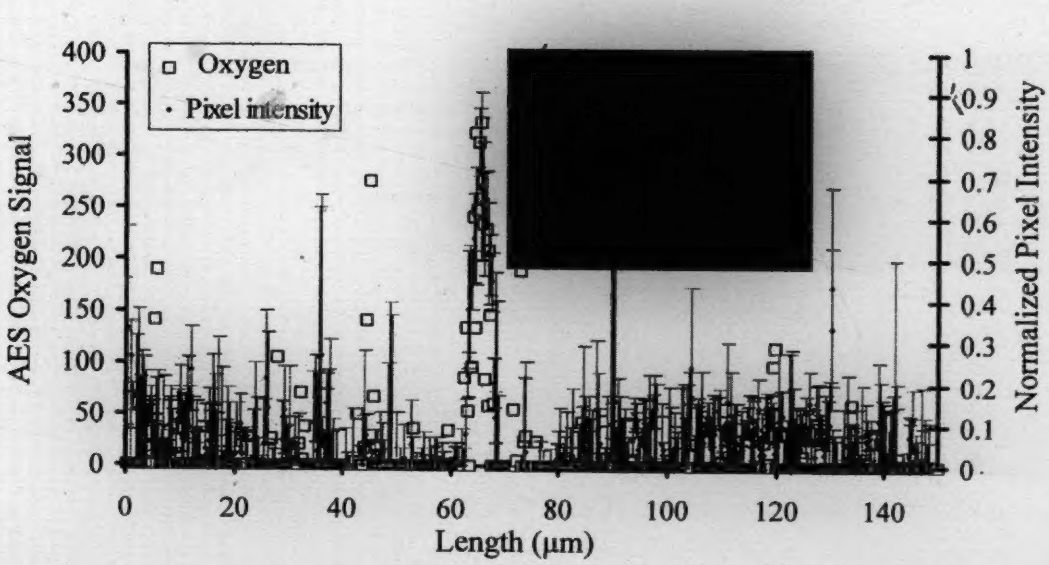

Figure 3-10. Correlation of AES oxygen signal (squares, left axis) with pixel intensity plots of the SEM image (small crystals with error bars, right axis) across the line (along the line marked in inset). The line has been made through scanning of a 20 mW laser beam focused with a 10X objective. The inset shows the SEM image out of which this pixel intensity plot is extracted, through scanning along the horizontal line.

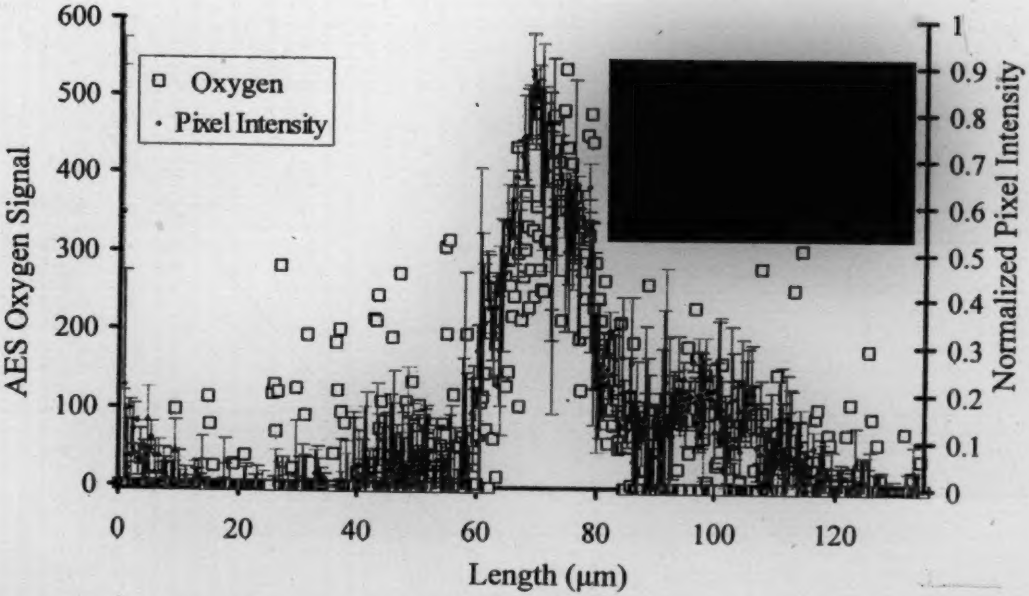

Figure 3-11. Correlation of AES oxygen signal (squares, left axis) with pixel intensity plots of the SEM image (small crystals with error bars, right axis) across a 20 mW line (along the line marked in inset). The line has been made through scanning of a 20 mW laser beam focused with a 10X objective (out of focus). The inset shows the SEM image out of which this pixel intensity plot is extracted, through scanning along the horizontal line.

References

(1) Xia Y.; Whitesides, G. M. *Angew. Chem. Int. Ed.* **1998,** *37,* 551-575.

(2) Shadnam, M.R.; Kirkwood, S.E.; Fedosejevs, R. and Amirfazli, A. *Langmuir* **2004,** *20,* 2667-2676.

(3) Shon, Y. S.; Lee, T. R. *J. Phys. Chem. B* **2000,** *104,* 8192-8200.

(4) Garg, N.; Carrasquillo-Molina, E.; Lee, T.R. *Langmuir* **2002,** *18,* 2717-2726.

(5) Fuierer, R.R.; Carroll, R.L.; Feldheim, D.L.; Gorman, C.B. *Adv. Mat.* **2002,** *14,* 154-157.

(6) Hugonnot, E.; Delville, J.P. *Phys. Rev. E* **2004,** *69,* 051605.

(7) Hugonnot, E.; Popescu, A.; Hanifi-Kadi, S.; Delville, J.P. *Phys. Rev. E* **2004,** *69,* 051606.

(8) Kirkwood, S.E.; Shadnam, M.R.; Fedosejevs, R.; Amirfazli, A. *Proceedings of the Int. Conference on MEMS, NANO and Smart Systems*; Banff, Canada, IEEE Publication: Los Angeles, 2003, pp 48-52.

(9) Lopez, G.P.; Biebuyck, H.A.; Whitesides, G.M. *Langmuir* **1993,** *9,* 1513-1518.

(10) Wormeester, H.; Kooij, E.S.; Poelsema, B. *Phys. Rev. B* **2003,** *68,* 085406.

(11) Brouwer, E.A.M.; Kooij, E.S.; Wormeester, H.; Hempenius, M.A.; Poelsema, B. *J. Phys. Chem. B* **2004,** *108,* 7748-7753.

(12) Lowry, T.H.; Richardson, K.S. *Mechanism and Theory in Organic Chemistry*, Harper & Row: New York, 1987; p 208.

(13) Plochocki, Z.; Mioduchowski, A.; Maczynski, J.F. *Z. Angew Math. Phys.* **1995**, *46*, 339-354.

(14) Ferrieu, F.; Auvert, G. *J. Appl. Phys.* **1983**, *54*, 2646-2649.

(15) Tzou, D.Y. *J. Heat Trans-T. ASME* **1989**, *111*, 232-238.

(16) Burgener, M.L.; Reedy, R.E. *J. Appl. Phys.* **1982**, *53*, 4357-4363.

(17) Huber, M.; Deutschmann, R.A.; Neumann, R.; Brunner, K.; Abstreiter, G. *Appl. Surface Sci.* **2000**, *168*, 204-207.

(18) Lax, M. *J. Appl. Phys.* **1977**, *48*, 3919-3924.

(19) Qiu, T.Q.; Tien, C.L. *Int. J. Heat and Mass Transfer* **1992**, *35*, 719-725.

(20) Lax, M. *Appl. Phys. Lett.* **1978**, *33*, 786-788.

(21) Schlenoff, J. B.; Li, M.; Ly, H. *J. Am. Chem. Soc.* **1995**, *117*, 12528-12536.

(22) Adams, F.; Van Vaeck, L.; Barrett, R. *Spectrochim. Acta B* **2005**, *60*, 13-26.

(23) Hayes, W.A.; Shannon, C. *Langmuir* **1996**, *12*, 3688-3694.

(24) Hayes, W.A.; Kim, H.K.; Yue, X.; Perry, S.S.; Shannon, C. *Langmuir* **1997**, *13*, 2511-2518.

(25) Bain, C.D.; Whitesides, G.M. *J. Am. Chem. Soc.* **1988**, *110*, 6560-6561.

(26) Bain, C.D.; Evall, J.; Whitesides, G.M. *J. Am. Chem. Soc.* **1989**, *111*, 7155-7164.

Chapter 4- Kinetics of Alkanethiol Monolayer Desorption from Gold in Air*

Introduction

Alkanethiol molecules can adsorb on a gold surface through strong gold-sulfur (Au-S) bond and self assemble into an ordered periodic structure at molecular scale called self-assembled monolayer (SAM). For modeling purposes of our recently developed "direct laser patterning" (DLP) methodology for SAMs,[1] we are interested in desorption kinetics of SAMs in air. To calculate the feature sizes generated using DLP one needs to combine SAM desorption kinetics equation with heat propagation equations.[2] Accurate activation energy value will allow for correct prediction of pattern sizes generated in DLP, i.e. a thermally driven process. Such kinetics information is also useful in feasibility studies for many other applications of SAMs (see ref. [3] and references therein).

Thermal stability and kinetics of SAM desorption in solvents have been investigated using ellipsometry[3,4] and temperature programmed desorption.[5] The coverage of SAMs in this study was characterized through X-ray Photoelectron Spectroscopy (XPS), which is significantly better than ellipsometry used in previous studies for quantitative analysis, and wetting observation.

Experimental Procedure

Thin films of gold supported on microscope glass were used as substrate for making SAM surfaces (experimental details can be found in ref. [1]). Thermal desorption of

---

* A version of this chapter has been published. *Shadnam, Amirfazli 2005. Chemical Communications. 38: 4869-4871.*

1-hexadecanethiol (HDT) in ambient air was studied in an oven for temperatures ranging from 383 to 653 K. The SAM coated gold samples were rinsed with ethanol and blown dry with 99.9998% pure nitrogen prior to the experiment. The SAM coated samples were placed in a preheated oven at the desired constant temperature (accuracy ±2 K). In order to facilitate the heat transfer though conduction, samples were placed atop a metallic plate in the oven. The temperatures were both read from the oven thermometer (which shows temperature of air) and measured by a thermocouple attached to the metallic base plate. It was ensured prior to each experiment that the two temperatures were at steady state and agreed with each other within ± 2 K. The temperatures were recorded at the beginning and the end of the heating period as well as a few times within the heating period. The samples were removed from the oven at the end of the selected time interval, rinsed with ethanol, and again blown dry with nitrogen. The samples were kept under 97% nitrogen and analyzed using XPS (Axis-165, Kratos Analytical) within less than 24 hours. The XPS operating conditions: base pressure was 0.5×10^{-10} Torr; the X-ray source used was Aluminum (monochromatized) with initial photon energy of 1486.71 eV operated at power of 210 W. In survey spectra pass energy was 160 eV; binding energy range was 0-1100 eV with steps of 0.33 eV. We examined high-resolution spectra of O1s, C1s, S2p and Au4f regions for each sample (pass energy was 20 eV and the steps were 0.1 eV each). In data processing, the intrinsic relative sensitivity factors and transmission function of the instrument were used. For composition analysis peak areas were integrated, with linear background subtracted. Take-off angle was 90° (normal to the surface). XPS signal of SAMs on gold surfaces depends on take-off angle. Sulfur signal decreases ~10% when the take-off angle is deceased from 80° to 0°, whereas gold signal decreases by ~30%.[6,7] Atomic percentages out of XPS analysis are closest (but still not equal) to the stochiometric values at 0° take-off angle.[7] Our XPS analysis were consistently performed normal to surface to avoid any variation of signals as discussed. The extent of desorption was measured by dividing the atomic S/Au ratio of each heated sample by the average of the atomic S/Au ratio of unheated samples (average of 6 samples), which were used as benchmark. Since we used the ratio of atomic percentages to the associated ones from our benchmark samples (analyzed under the very same conditions) our coverage ratios represent the percentages of SAM species present on surface.

Results and Discussion

The XPS spectra of heated samples show evidence of SAM desorption. For example, the 162 eV S2p doublet signal (i.e. S2p3/2 and S2p1/2 with 2:1 ratio of photoionization cross sections and 1.2 eV difference in binding energy), which shows chemisorbed sulfur, was quantitatively less intense than those collected from SAMs at full coverage (unheated samples) under the same conditions (see Fig. 4-1). The S2p region of XPS spectra shown in Fig. 4-1 clearly demonstrate the loss of sulfur from the gold surface after heating the sample at 653 K for 1 minute. Figure 4-1 also shows C1s region of the same 3 samples that corroborate the desorption of SAMs. The C1s signal does not completely fade in case of heated sample at 653 K, which can be due to presence of some carbonaceous contamination. The XPS results were consistent with our wetting observations; all samples prior to heating appeared hydrophobic whereas after heating samples that experienced higher temperatures for longer times were visibly hydrophilic.

It was also examined that by omitting the rinsing step after heating (see notes), the spectra sometimes showed weak shifted sulfur peaks; such shifted S2p peaks are known to signify presence of physisorbed sulfur[6,7] (S2p binding energy depends on the sulfurs chemical state. The bound thiolate shows S2p3/2 signal close to 162 eV (see Fig. 4-1) whereas unbound sulfur causes the binding energy increases.)

Ratio of areas of S2p doublet over Au4f peak was calculated and then normalized with respect to that of fully SAM covered unheated samples to find coverage of monolayer on sample surfaces. Figure 4-2 shows the time dependent desorption of HDT SAM at different temperatures in air. The SAM desorption rate was slower than those from earlier studies of similar SAMs into solvent media at 383 K reported by Garg et al.[3] and Shon and Lee[4] for HDT and 1-heptadecanethiol, respectively (there is evidence in the literature8,9 that for long chain alkanethiols kinetics constants do not change). At high temperatures SAM is completely desorbed in a few minutes (Fig. 4-2a). The time for desorption of 50% of HDT SAM in decalin at 383 K is less than 2.5 min[3] and that of 1-heptadecanethiol SAM under same conditions was less than 1 min;4 it takes, however, ~1 hour to desorb 50% of HDT in air (see Fig. 4-2b).

At 383 K full desorption was not achieved during our test period, i.e. 2 hours. The desorption profile at 383 K seemingly has a horizontal asymptotic higher than zero coverage (see the dashed line in Fig. 4-2b) at ~40% SAM coverage. Thermal desorption at 363 K also showed the same trend as that of 383 K with a higher asymptotic (data not shown). Shon and Lee[4] reported such an asymptotic desorption behavior for desorption of 1-heptadecanethiol in decalin at similar temperature (i.e. 373 K) near 20% SAM coverage; whereas Garg et al.[3] did not report any more than zero SAM coverage asymptotic for desorption of HDT in decalin. Asymptotic behavior can signify that thermodynamic yield of the SAM desorption reaction is not 100% below a certain temperature threshold, which is characteristic of endothermic reactions. Shon and Lee[4] reported SAM full desorption for 383 K in 3 min; but they could not reach full SAM desorption in their experiments in 363 K and 343 K, even after more than 4 hours. Thus, for long chain alkanethiol SAMs the thermodynamic threshold for incomplete desorption is between 363K and 383 K; whereas the same threshold for SAM desorption in air is somewhere between 383 K and 433 K (Fig. 4-2b). Lower threshold of incomplete desorption in liquid shows that thermodynamically the desorption reaction is more productive in liquid media, which could be explained in terms of solvatation of desorption products, i.e. dithiols, in liquid media.

All monolayers were desorbed in shorter time scales at higher temperatures. Downward shift of ultimate desorption asymptotic line with increasing the temperature shows thermodynamic enhancement of yield of SAM desorption reaction, which is consistent with what is expected from endothermic reactions. Such dependence of final yield of SAM desorption reaction has previously been reported for desorption of SAMs in solvent media as well.[3,4]

The data in Fig. 4-2 illustrate important features of the desorption behavior of the SAMs. Comparing the diagrams in Fig. 4-2 shows that the slope of the desorption profiles (rate constants) increase with increasing temperature, which is consistent with an endothermic thermally activated process.

Based on qualitative observations a two consecutive first order regimes is suggested in literature for desorption of SAM in liquid media;[3] in this study we provide a quantitative analysis and model for desorption of SAM. But before that, to determine order of the desorption kinetics, the data in Fig. 4-2 were analyzed with the classical graphical tests: The graphs in Fig. 4-2 are not linear; therefore, the SAM desorption reaction in air cannot be a zeroth order reaction. Semilogarithmic plots of data were used to see if the reaction follows a first order kinetics, i.e. the rate of desorption is proportional to the surface concentration of SAMs. Semilogarithmic graphs (see Appendix 5) showed that data from higher temperature experiments follow a linear trend more closely than those at lower temperatures as judged by the correlation coefficient (R^2=0.9 at 653 K and 513 K, but R^2=0.7 at 433 K and R^2=0.4 at 383 K). We also examined possibility of a second order desorption, i.e. the rate of desorption is proportional to square of surface concentration of SAMs. Linearity of graph of inverse of products versus time is characteristic of a second order reaction. The linearity at higher temperatures, were poor (R^2=0.6, 0.7, 0.4 and 0.8 at 653 K, 513 K, 433 K and 383 K, respectively; see Appendix 5). We concluded that SAM desorption in air is better represented by a first order reaction compared to a second order and zeroth order kinetics.

To demonstrate our quantitative analysis, first we examine the case of a single 1st order kinetics to describe the desorption. The data from all examined temperatures were fitted to the first order kinetics equation using least square method and the activation energy was back calculated through error minimization. Thus, the resulting desorption profiles were fitted to the following first order kinetic equation:

$$dC/dt = -k(T).C \tag{1}$$

where C denotes surface concentration of SAM, and *k* is the proportionality factor (also called rate constant). The rate constant is a temperature (T) enhanced factor according to the Eyring equation:[10]

$$k(T) = \frac{k_B T}{h} \exp\left(-\frac{\Delta G}{RT}\right) \tag{2}$$

where k_B is the Boltzmann's constant, *h* is Planck's constant, ΔG is the Gibbs free energy of activation of the SAM desorption reaction, and R is the universal gas constant.

The temperature dependence of the rate constant is determined according to Eq. 2 for a known value of Gibbs activation energy. In order to find the final SAM concentration on a surface, the desorption rate (Eq. 1) was integrated over time; and it resulted in the following equation:

$$C(T,t) = C_0 \exp\left(-\frac{k_B T t}{h}\exp\left(-\frac{\Delta G}{RT}\right)\right) \tag{3}$$

In the above equation C_0 represents the initial SAM coverage, which is assumed to be complete and uniform everywhere (i.e. C_0=1). Least squares method was used to fit Eq. 3 to experimental results. The error function was calculated for a wide span of activation Gibbs energy values (0 to 90 kcal/mol) to identify the minimum.

Activation Gibbs energy evaluated from fitting Eyring equation to data of HDT SAMs desorption in air was calculated to be 30.5 ± 0.5 kcal/mol (see Fig. 4-3), which is close to previously reported data in literature for long chain aliphatic SAMs of alkanethiol type, i.e. 30.1 ± 0.5 kcal/mol.[8] We checked that elimination of data points of any of the tested temperatures will not change the final calculated activation Gibbs energy by more than ± 0.4 kcal/mol. This value is shown to be fairly constant for alkanethiols of different chain length[8] and terminal group.[9] This independence is attributed to the fact that chemisorption occurs through interaction of sulfur atom with gold surface and the rest of the molecule does not play a significant role.[9]

The calculated activation Gibbs energy, i.e. 30.5 ± 0.5 kcal/mol, is higher by 15% compared to the value previously reported for desorption of the same SAM into liquid solvent, i.e. 27± 1 kcal/mol.[3] This is consistent with our observation of slower desorption of SAMs from gold in gaseous media compared to solvent media. The observation also conforms to theoretical expectations, as solvation interactions of molecules in media are stronger in solvent media compared to gaseous state where the molecules are far apart (and there is no solvation at all). Stronger solvation interaction of media molecules both thermodynamically and kinetically is in favor of faster desorption in solvent. Thermodynamically, HDT with bulk vapor pressure of 0.1 mmHg at 293 K and bulk boiling point of 303 K does not volatilize at ambient temperatures into gaseous media but it can easily be dissolved in organic solvents. This argument shows that desorption of HDT should lead to thermodynamically more stable state in solvent media compared to gaseous media. Thus, it can be expected that the transition state that leads to the final desorption products also be more stable in solvent, thus kinetically more favorable and associate with a smaller value of desorption Gibbs activation energy.

Two consecutive first order kinetics regimes was suggested by Garg et al.[3] for desorption of SAMs in liquid solvent: an initial fast desorption regime followed by a slow regime. However, Garg et al.[3] did not mention any transition time for shifting from fast regime into slow regime. We examined this idea quantitatively to see if it can better describe our results and open the door to a more quantitative evaluation of the suggested mechanism. We assumed a fixed temporal threshold for transition between the two first order kinetics (*tc*). Such assumption will allow us to estimate over the range temperatures examined that how long desorption of weakly bound molecules will take. Fitting our experimental data points to such a two regime mechanism required a 3 parameter least square optimization; parameters are activation energy of each regime and the transition time (*tc*). This process was executed through iteratively fixing one of the three parameters and finding the other two parameters through graphical minimization of error function. This process converged to (4 iterations): ΔG_{fast}= 29.9 kcal/mol, ΔG_{slow}= 32.7 kcal/mol, *tc* = 87 sec. The result was reconfirmed through calculating the error function on a grid of all 3 parameters with 0.1 kcal/mol spacings for activation energy and 1 sec steps for transition time. The optimal result conformed with what we obtained using the iterative method. This transition time (i.e. 87 sec) can be considered as the upper limit of the first desorption kinetics given that there might be an enhancement with temperature for switching from the fast to slow regime. Figure 4-3 shows significance of the 2 step mechanism by providing a better fit to experimental data. To further verify the validity of *tc*, we fitted data for the first 87 sec of individual series of experiments (fixed temperature) to Eyring equation; the resulting values for ΔG_{fast} were all in range of 28 to 34 kcal/mol with average close to the reported value (less than 4% difference). The same test on ΔG_{slow} also resulted in values in range of 30 to 35 kcal/mol with average close to the reported value (less than 4% difference). The agreement further shows validity of the transition threshold. The reported values for activation energies of the fast and slow regimes differ by 2.8 kcal/mol, which is much larger than accuracy of determining these values (0.1 kcal/mol); it means the two desorption regimes are distinct from each other.

Summary and Conclusions

We used the results of the above kinetics investigation in our thermokinetics model[2] for DLP. Since laser patterning occur in a few seconds,[1] energetics of fast desorption regime were used for calculations. The SAM coverage profiles were examined at powers of 73, 49, and 24 mW. Slower rate of desorption of SAMs in air causes line widths (full SAM desorption) produced in DLP to decrease by ~20%. The new data helps in better predicting DLP results as a result of accurate kinetics information available in this study.

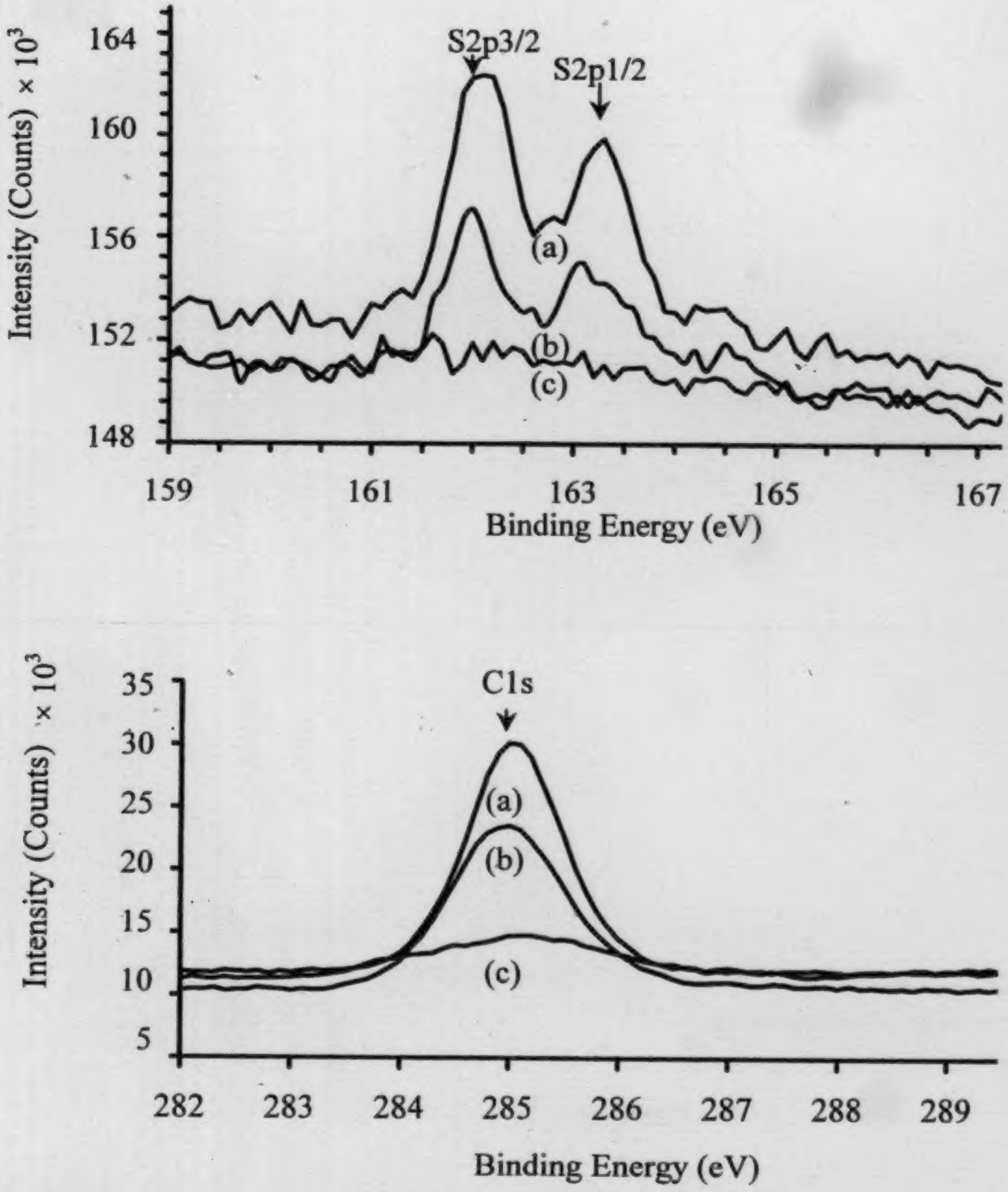

Figure 4-1. High resolution XPS spectra for S2p (up) and C1s (down) of HDT SAM on gold. (a) before heating (b) after heating at 383 K for 2 hours and (c) after heating at 653 K for 1 minute.

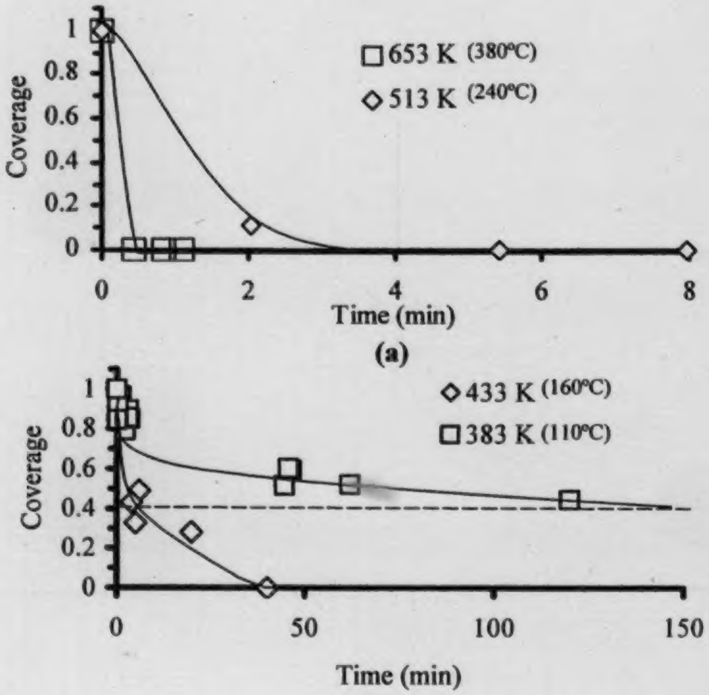

(a)

(b)

Figure 4-2. Thermal desorption profile of HDT SAMs from gold surface at (a) 653 K (=380 °C) and 513 K (=240 °C), (b) 433 K (=160 °C) and 383 K (=110 °C). The lines are to guide eyes.

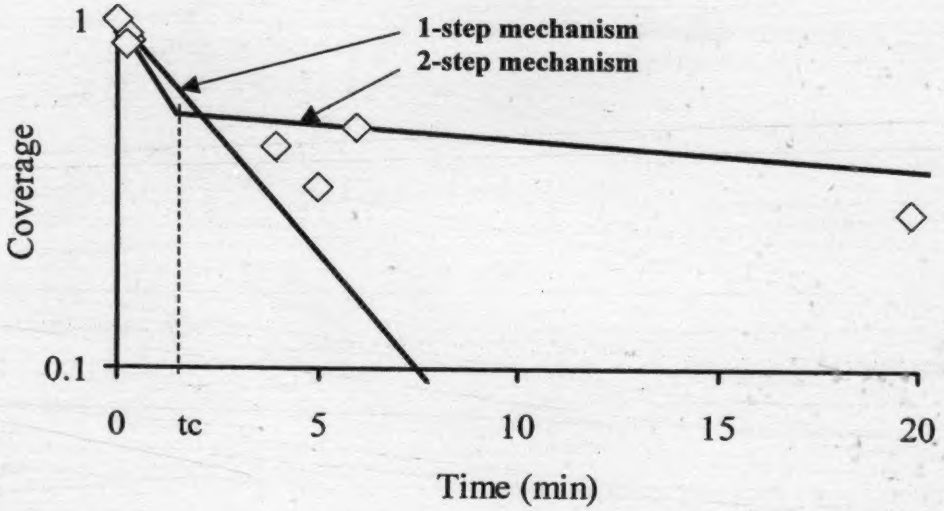

Figure 4-3. A sample of fitted curves to experimental desorption data at 160°C. Symbols represent experimental data.

References

(1) Shadnam, M.R.; Kirkwood, S.E.; Fedosejevs, R. and Amirfazli, A. *Langmuir* **2004**, *20*, 2667-2676.

(2) Shadnam, M.R.; Kirkwood, S.E.; Fedosejevs, R. and Amirfazli, A. *J. Phys. Chem. B* **2005**, *109*, 11996-12002.

(3) Garg, N.; Carrasquillo-Molina, E.; Lee, T.R. *Langmuir* **2002**, *18*, 2717-2726.

(4) Shon, Y. S.; Lee, T. R. *J. Phys. Chem. B* **2000**, *104*, 8192-8200.

(5) Schlenoff, J. B.; Li, M.; Ly, H. *J. Am. Chem. Soc.* **1995**, *117*, 12528-12536.

(6) Sun, F; Castner, D.G.; Grainger, D.W. *Langmuir* **1993**, *9*, 3200-3207.

(7) Wang, W.; Castner, D.G.; Grainger, D.W. *Supramol. Sci.* **1997**, *4*, 83-99.

(8) Wetterer, S.E., Ph.D. Thesis Princeton University, NJ (Princeton) 1998, Chap. 4.

(9) Nuzzo, R.G.; Dubios, L. H.; Allara, D. *J. Am. Chem. Soc.* **1990**, *112*, 558-569.

(10) Lowry, T.H.; Richardson, K.S. *Mechanism and Theory in Organic Chemistry*, Harper & Row: New York, 1987; p 208.

Chapter 5- Using Laser to Fabricate Miniaturized Network of Open Channels: Curvilinear Paths and Various Junction Types

Introduction

Self-assembled monolayer (SAM) is a packed and organized one-molecular layer of chemically bounded organic molecules on certain metalic surfaces, e.g. gold, silver. Depending on their tail groups, SAMs can mask certain properties (e.g. wettability and adhesion) of the substarte. For example, 1-hexadecanethiol (HDT), $HS\text{-}(CH_2)_{15}\text{-}CH_3$, form a hydrophobic SAM on surface and 16-mercaptohexadecanoic acid (MHA), $HS\text{-}(CH_2)_{15}\text{-}COOH$, form a hydrophilic SAM. From technological point of view, self-assembled monolayers are important for their potential in the development of biological and chemical sensors,[1] microfluidic lab-on-chips,[2] transistors,[3] electronic manufacturing,[4] and fabrication of photonic devices.[5] In the above applications SAM are used to modify physical, chemical, biological and/or optical properties of a substrate. In this way, SAMs offer an excellent means for manipulation of surface properties.

There are various ways to create surfaces having different properties in neighbouring regions (patterned surface) with SAMs such as photolithography,[6] microcontact electrometric stamping,[7] dip-pen lithography,[8] and direct laser patterning (DLP).[9] The resulting patterned SAM surfaces have been used to make channels without physical wall,[9] valves for controlled liquid delivery in microfluidics,[10] enzymes immobilizing biotechnology applications,[11] resistant in lithography steps,[12] and implantation of nanotube networks.[13] Channels of desired width and various curvilinear paths (sharp and smooth bents, arcs, etc.) and various junction types (crosses, T-junctions, etc.), which are focus of this chapter, on their own and together with comaptible valves[10] and various compatible methods of active liquid movement on the channels[14-16] constitute elements of different lab on a chip systems (e.g. combinatorial grids and microfluidics).

It is shown that at high temperatures the gold-sulfur bond becomes unstable and SAMs regardless of their origin (either alkanethiol or dithiol) desorb as dimmer molecules from surface.[9] Thermal instability of SAMs at elevated temperatures has succesfully been used as a means for making patterned surfaces in DLP[9] (see Fig. 5-1). As shown in Fig. 5-1, laser patterning uses a focused laser beam as means of localized heating to desorb thiol molecules in areas of interest on the surface and then backfills the bare regions with a second thiol that has a different tail group in order to engineer micropatterned surfaces of derired properties.[9] For example, a hydrophilic SAM patterned on a hydrophobic SAM background will delimit liquid on the hydrophobic region of the surface and act as a liquid pool or channel without any physical barrier (Fig. 5-2). The DLP technique is simple, economic and fast; using this technique the patterns of multiple SAMs can easily be made and removed over arbitrarily large areas on a single surface. The DLP procedure does not need any solvent and can be executed in gaseous media under atmospheric pressure.

In this chapter capabilities of DLP methodology for fabrication of curvilinear paths and various junction types is explored. Fabrication of nonlinear features using the above techniques require heating on nonlinear trajectories. Thus, the question arises as how and to what extent the geometry of patterns (e.g. curvature of the heating trajectory) may affect the induced temperature profiles and the resulting feature sizes. Although classical analytical solutions as well as recent numerical solutions exist for the problem of moving heat source along a straight line (see for example refs [17], [18] and the references there in), there is no consideration of the heating on more complex geometries (e.g. curvilinear trajectories) in literature. Therefore, this chapter also reports on the effect of trajectory curvature and heat source velocity on the induced temperature field for a model substrate system.

Experimental Procedures and Materials

Thin films of gold on microscope glass were made using sputtering: glass slides are first sputtered with 50 Å of titanium to provide an adhesion layer for the 300 Å of gold that is sputtered afterwards. The HDT SAM was formed through solution deposition i.e. placing a gold coated substrate into a solution of HDT overnight under inert atmosphere (preparation details can be found in ref [9], Chapter 2). The sample is taken out of solution and placed into the substrate holder in the micropositioner setup (Fig. 5-3). Instead of moving the laser to make a pattern onto the sample, two micropositioners controlled the *x* and *y* positions of the sample (Fig. 5-3) while the laser beam remained stationary. The micropositioners were Coherent EncoderDriver linear actuators and were controlled by a PMC DCX-PCI100 controller card. The laser beam (after being aligned, calibrated, characterized and focused) used to desorb the HDT SAM on areas of interest. The substrate was then placed in a solution of

MHA; the MHA hydrophilic SAM backfilled bare regions. Feature sizes were measured using an optical microscope as well as Scanning Electron Microscopy (SEM) images.

An algorithm and pattern generation system was designed to make monolayer patterns such as crosses, T-junctions, cusp angles, and curves using DLP method. Since the controller moved the micropositioners independently, a software algorithm was required to emulate dependent axis motion. The algorithm was implemented using C++ to allow the controller card to control micropositioner movement such that any combination of features could be patterned onto the substrate. Separate algorithms were designed as individual functions to make different features. The net velocity of the positioners were kept constant along all featurs (0.2 mm/sec). To pattern curvilinear featurs, the controller must be used in velocity mode, where dynamic control of velocity can be achieved. By making the velocity of one positioner a function of the position of the other positioner, dependent motion can be emulated. The parametric equations of each feature and the velocity of the controller was determined. The hardware did not accept negative velocities as inputs and instead required an input for the direction of motion and a positive value for the velocity. For example, the algorithm split a circle into 4 sections corresponding to the 4 quadrants of the circle. Depending on the quadrant, the direction of motion for each axis was determined, and an absolute value for the velocity was input into the controller.

Figure 5-4 shows the optical setup of DLP. In our DLP setup, a Melles Griot Argon ion laser emited laser beam (488 nm line) that passed through two polarizers, which were used to adjust the power. The beam then went through a wedge, which reflected ~4% of energy into a power meter. The beam was then reflected on two mirrors and went through two apertures. The apertures were used for alignment of the beam. A microscope objective used to focus the beam onto the sample. To pattern discontinous features, a beam blocker was used to block the beam when the satges were moving the sample to the new start point.

Experimental Results

Various types of features were made: stair pattern, circle, cross, tee junction, cusp angles, bents and circles. Figure 5-5 shows images of patterns written at 27 mW under light microscope; a drop of tridecane was placed on the substrate for visualization (liquid only wets hydrophilic regions). The line widths of all the features are all approximately 30 μm, which matches theoretical expectations.[19] More examples are presented in Appendix 4.

Figure 5-5 shows optical microscope images of cusp angles and crosses written at 27 mW with tridecane on surface (for visualation). Figure 5-6 shows SEM images of crosses and T-junctions written at 18 mW and 27 mW. The feature size remained unchanged near the intersection point, i.e. no broadening or necking was observed. Figure 5-7 shows SEM image of a cusp angle with an angle of 90° written with a 18 mW beam. The cusp angle seemed to have two different levels of contrast within the feature. In the darkest areas of the feature, full desorption has occurred and the hydrophilic monolayer has backfilled this area. In the areas with lighter contrast, however, only partial desorption may have occurred. The reason can be that the laser has a Gaussian profile with most of its energy directed to the center of the beam. The power is lower in the outer sides of the beam, therefore, only part of the monolayer is desorbed on the edges (see ref. [19] for more information). No feature size change is observed near the vertex of the angle. Figure 5-8 shows SEM image of 2 circles. Figure 5-9 shows an image of the "U of A" (abbreviation of our institiution) patterned as a hydrophilic MHA SAM on a hydrophobic HDT SAM background.

Surface Temperature Profile Induced by the Laser Beam

In DLP, it is shown that there is a critical temperature threshold for desorption of species from the surface which controls the resulting feature size; also substrate damage can occur beyond an upper temperature threshold.[9] Thus, the precise knowledge of temperature field in material induced by the moving laser beam is important. In general such problem belongs to a wider field of temperature profile induced due to a moving heat source.

In our experiments, the thermalization is faster than the SAM desorption reaction; as such the process in DLP with Argon laser is thermally activated. In such cases the energy deposition is not photochemically regulated (i.e. the individual photons of laser beam directly initiate the process); it is thermally controlled (i.e. energy is absorbed by the substrate and provides a localized high temperature and the resulting temperature field generated by the laser then causes the process) and the laser act like a heat source. [9]

Formulation of Thermal Model

A Gaussian heat source with 2e-folding intensity radius (radius at $1/e^2$ maximum intensity) of w_0 and incident power, P, is scanned with a constant velocity, v, along a trajectory defined by $\underline{x}(t)$ and $\underline{y}(t)$ on the surface of a sample (t denotes the time). The material is assumed to have temperature dependent thermal conductivity. The coordinate system origin can be any fixed point on surface of the sample; for circular arcs examined here the coordinate system origin (used in our formulation) overlays on the center of the circular-arc trajectory. For linear segments the origin is at the starting point of the line segment.

Since continuous heating is considered in this paper, the pulse length is physically infinite. As relaxation and thermalization occurs in picoseconds they are significant on such time scales or heating with ultra-short pulses and not for continuous heating used in this study (see for instance [20,21]); thus details of photon-electron and electron-phonon interactions are not included in this study. Thus, the diffusion model can be used, as the time scale of heating is larger than the thermal relaxation time.[20,21] The diffusion model is also appropriate as length scale is larger than the phonon mean free path, which is reported to be of submicron order (see for example [21,22]). Thus, the results presented in this chapter are physically valid for time scales longer than picosecond and length scales on the order of micrometers.

The governing heat equation is derived from the classical Fourier diffusion equation adapted for a moving source heating:[9,23]

$$\nabla \cdot [\kappa(T).\nabla T] + Q(x,y,z,t) = \frac{\kappa(T)}{D(T)}.\frac{dT}{dt} \tag{1}$$

where κ, D, T and Q represent the sample thermal conductivity, thermal diffusivity, temperature and heat source function, respectively. Furthermore, in Eq. 1, *x*, *y*, *z* denote stationary coordinates and d/dt is the time derivative. The thermophysical and optical properties of the sample are assumed to be independent of position and orientation within planes parallel to x-y plane due to homogeneity and isotropy of the glass substrate.

To determine the mathematical form of the heat source function, i.e. Q(x,y,z,t) in Eq. 1, it was calculated that more than 99% of the absorption occurs at the gold layer.[9] In the presented thermal model it is assumed that the absorbed energy is fully delivered to the gold layer. Thus, a Dirac delta function in the z direction can represent the deposited energy penetration for the CW argon ion laser used. The energy distribution in x and y directions is Gaussian. The moving Gaussian intensity distribution is normalized to give a total power P. Hence, the moving heat source term in Eq. 1 is represented by:

$$Q = \frac{2PA(T)}{\pi w_0^2} \exp\left(-2 \frac{\left(x - \underline{x}(t)\right)^2 + \left(y - \underline{y}(t)\right)^2}{w_0^2} \right) \delta(z) \tag{2}$$

where A represents the optical absorption percentage of the sample. The temperature dependence of optical absorption is neglected.[9] It is also shown that temperature dependence of sample thermal diffusivity can be neglected.[9]

Equation 1 can be linearized using Kirchhoff transformation:[17]

$$\Theta(T,t) = \int_{T_0}^{T(t)} \frac{\kappa(s)}{\kappa_0} ds \tag{3}$$

where T_0 is initial substrate temperature, κ_0 is conductivity at T_0 and Θ is linearized temperature change over room temperature. We solved Eq. 3 analytically using a linear fit to available experimental data[9] for temperature dependence of conductivity ($\kappa(T)=k_0+k_1.T$) and solved the resulting equation for temperature:

$$T(t) = \frac{-2k_0 + 2\sqrt{(k_0 + k_1 T_0)^2 + 2k_1 \Theta \kappa_0}}{2k_1} \tag{4}$$

In the examples presented in this paper a linear increase of conductivity with temperature at a slope of 0.68 mW/mK^2 (k_1), and room temperature conductivity of 0.872 mW/mK (k_0), which are characteristic of soda lime glass (the substrate used in our laser patterning experiments) is used. Considering case of temperature independence of κ, Eq. 4 gives the substrate temperature, which is physically expected. The linearized form of Eq. 1 is:

$$\frac{\partial\Theta}{\partial t} - D\nabla^2\Theta = \frac{DQ}{\kappa_0} \tag{5}$$

To solve Eq. 5, the known solution of the temperature distribution of a unit point source, G, located at coordinates X, Y, t′ on the surface is superimposed. Heat flow from the laser at X, Y, t′ on the surface influences the temperature x, y, z in the material at a later time t by

$$\Theta = \int_0^t \int_{-\infty}^{+\infty}\int_{-\infty}^{+\infty}\int_{-\infty}^{+\infty} \left(\frac{DQ}{\kappa_0}\right)(XYZt') \times G(XYZt', xyzt)\,dZdYdXdt' \tag{6}$$

The Green's function, G, for the diffusion equation is:

$$G = \frac{\exp\left(\frac{-(x-X)^2-(y-Y)^2-(z-Z)^2}{4D(t-t')}\right)}{4(\pi D(t-t'))^{3/2}} \tag{7}$$

Assuming a circular arc of radius *r* as heating trajectory being scanned at constant angular speed, *w*, means $\underline{x}(t) = r.\cos(wt)$, $\underline{y}(t) = r.\sin(wt)$. For laser patterning applications the temperature profile on the surface (z=0) was of our concern. We were interested in the temperature profile along radial and tangential directions, which suggests use of cylindrical coordinate system would be more useful ($x = \rho.\cos(\alpha),\ y = \rho.\sin(\alpha)$). Substitution of x and y in the integrand in Eq. 6 and algebric simplification, results in:

$$\Theta(\rho,\alpha,t) = \frac{PA}{2\kappa_0 \pi^{3/2}} \int_0^t \frac{\exp\left\{-\dfrac{r^2+\rho^2+2r\rho\cos(w(t-t')-\alpha)}{2(w_0^2+2Dt')}\right\}}{(w_0^2+2Dt')} \sqrt{t'}\,dt' \qquad (8)$$

Spatial parameters appear only on the numerator of the exponential. For all real values of r, the numerator trends to zero as ρ trends to +∞, thus, exponential and the whole integral vanish as physically anticipated: far away from the heating region, there should not be any temperature change.

Before using the model for our experimental cases, features of the solution are qualitatively studied. Considering the range of t' (from 0 up to t), it can be concluded that the denominator in Eq. 8 will always be positive. The quadratic numerator of the exponent is also always nonnegative as the coefficient of the second-degree term is positive and $\Delta = 4r^2\left(\cos^2(w(t-t')-\alpha)-1\right) \le 0$ as range of cosine function is between –1 and +1. Thus, the exponential never diverges (i.e. never trends to infinity) and the grater the numerator of exponent the smaller is the value of exponent (because e^{-a} is a decreasing function of a); hence where the numerator has a minima the exponent has a maxima and as result, the integral has a mixima as well. The minimum of the exponent numerator occur at $\rho = -r.\cos(wt'-\alpha)$; since the cosine function is always between –1 and +1, one can conclude that the locus of the maximum temperature should always be closer to the center of rotation than radius of curvature of the heating trajectory. This conclusion is physically expected, as the instantaneous hot regions have more overlap on the concave side of the heating trajectory compared to the convex side (see Fig. 5-10). It can also be argued that the shoulder of heating gaussian profile at concave side of the heating trajectory is scanning at a slower linear velocity compared to the other shoulder of the heating gaussian profile (since linear scanning velocity is the constant angular velocity multiplied by radius).

Moreover, the term responsible for asymmetry is in numerator of the exponent in Eq. 8 whereas beam size (w_0) is in denominator of the same exponent; exponential function with negative exponent shows maximum sensitivity at lowest values of the exponent; thus, asymmetry effects are more significant for larger values of beam size compared to radius of curvature, which appears in numerator of the exponent. In short lower ratio of r/w_0 magnifies curvature assymetry effects. At extreme case of $r/w_0 \rightarrow 0$ a big beam scanning a small circle, it is intuitively evident that the center point (of circle) would have maximum temperature. Along this line of reasoning, comparing the maximum temperatures for different radii of curvature shows more sensitivity at higher value of beam size.

In our computations, the temporal integral (i.e. Eq. 8) was numerically calculated using 0.5 ns time steps, which grantees 10 digits of precision for the computation.[24] The code is placed in Appendix 3.

Discussion

The results for temperature profiles of a few laser heating cases with a laser beam of 44 μm size (2e-folding intensity radius) that, as mentined above, can better shows the above mentioned curvature effects are discussed first. In second part results for a laser beam of 8 μm size (2e-folding intensity radius), which is relevant to our experimrnts are discussed.

Figure 5-11 shows width of the area that experiences temperatures equal or higher than 80% of the peak temperature ($w_{80\%}$) induced by a moving CW laser beam as it scans a circular arc (of radius 88 μm); the $w_{80\%}$ is used as a measure for comparing width of temperature profiles. Figure 5-11 shows that the higher the heating velocity the narrower is the width (80% of the peak temperature or higher). It also shows that 1 order of magnitude change in speed does not affect the feature sizes as much as a 30% change in laser power does change feature sizes. Thus, the main controlling parameter in DLP is power of the laser beam.

Calculated temperature profiles for scanning velocities of 0.1-1 mm/s were examined and no visually noticable asymmetry in temperature field with respect to centerline along the heating trajectory was observed. This suggestes that for noticable asymmetry of temerature profiles with respect to centerline to be present r/w_0 should be smaller than 2 examined here (i.e. $r/w_0<2$). Symmetry of temerature profiles, for example, suggests that for the moving laser spot speeds of 0.1-1 mm/s the resulting features in laser patterning process will be symmetric with respect to the centerline of the heating trajectory.

The model calculation shows that the locus of the hottest temperature is at negligible distance (behind) the instantaneous locus of the moving beam for both linear and curved trajectories. Both occurrence of maximum temperature at the center of heating spot and negligible asymmetry of temperature profiles are in agreement with the theoretical results obtained by Burgener and Reedy[25] for heating along straight line trajectories. They showed resulting temperature profiles are symmetric in the X and Y directions for slow movement of a heating spot. Burgener and Reedy[25] noticed that asymmetries in induced temperature profiles appear at heating spot velocities of more than 0.3D /w_0 (i.e. ~4.5 mm/s using parameters of our system). Beyond this velocity threshold, e.g. at 5 mm/s, asymmetry of induced temperature profile along the scanning path was also observed by us.

To compare the induced surface temperature for heating along different trajectories, the resulting peak temperatures are also compared. Peak temperatures are also of our concern as it can damage the substrate if it rises beyond a limit. The intention is a twofold comparison: (1) comparison of heating along a straight line with that of a curved trajectory; (2) comparison of various curved trajectories to one another. Figure 5-12 compares the peak temperature due to heating on circular-arc (quarter circle) with those of heating on the associated chord of the arc (representing heating on a straight line of proportional length). The temperatures are slightly lower for heating along the chord than that of heating on the associated quarter circle at the end point of the line and quarter circle due to accumulation of heating during the length of the trajectory (arc is longer than its associated arc). Figure 5-12 shows that with decreasing radius of curvature the difference in peak surface temperature is decreased for a constant speed and spot size. The maximum temperature change with radius is more pronounced as processing speed is increased. The results presented in Fig. 5-12 can be interpreted in terms of combined effect of heating time and accumulation of heat due to heating trajectory. The time needed to scan a quarter of a circle (and its associated chord) and thus the amount of energy transferred to the substrate is linearly proportional with the radius of curvature of the circular path. For example, the scanning time for a quarter circle of smallest radius in Fig. 5-12 (radius of curvature equal to 2 times beam radius) is 0.69 sec, whereas the scanning time for a quarter circle of largest radius in Fig. 5-12 (radius of curvature equal to 50 times beam radius) is 17 sec. Thus, the energy deposited on surface is more for higher radii of curvature. We also checked maximum temperatures for case of heating the surface with a laser beam of 0.6 μm waist and scanning speeds of 0.1-10mm/sec. The pattern is similar to those observed for a 44 μm beam but the differences are much less prominent compared to those presented in Fig. 5-12 (less than 2% differace among peak temperatures of all considered scanning speeds and radii of curvature).

Figure 5-13 shows dependence of maximum resulting temperature on radius of curvature of the heating trajectory for two heating velocities, i.e. 0.2 and 1 mm/s. It is observed that the peak temperature decreases sharply with decrease of heating trajectory's radius of curvature for highly curved trajectories, i.e. having radii of curvature less than ten times that of the Gaussian heat source radius, $r/w_0<10$. In contrast, the peak temperature induced would not change significantly (at most 6.5 K) with an increase in the radius of curvature of heating trajectory when the radius of curvature is more than ten times the Gaussian heat source radius ($r/w_0>10$). Thus, for example in laser patterning applications, the resulting feature size should not show sensitivity for mildly curved paths.

Effects of scanning speed and radius of curvature in making circular arcs and various types of junctions for patterning with a beam of 8 μm (2e-folding intensity), which is relevant to our experiments, radius is also considered. Figure 5-14 shows the effect of scanning speed on the maximum temperature (representing the resulting gaussian-looking temperature profile). Inspection of temperature profiles (not shown here) for different scanning speeds revealed that the temperature profiles do not intersect each other, i.e. the one that has higher peak temperature has broader waist at all temperature levels. Figure 5-14 shows, as physically expected, increasing scanning speed decreases the maximum temperature (and narrows down feature sizes). However, for speeds below centimeters per second the maximum temperature (and as result feature sizes) are practically constant.

In making angles the laser beam should change the scanning direction at the vertex. Because of inertia, mechanical movement actuators (micromanipulators) cannot provide any sudden change in components of velocity, any change in velocity is only possible at certain acceleration. It means that at least a component of speed of the scanning beam has to slow down near the angle point, which might cause broadening in feature sizes as described in Fig. 5-2. However, for this case, Fig. 5-14 shows that one should not expect any measurable change in peak temperature (and broadening of feature size) near vertex of angles, where the scanning speed (initailly 0.2 mm/sec) slow down by less than an order of magnitude. This expectation is agrees with what we see in our SEM images (see Figs. 5-7 and 5-9).

Since in making a cross the laser beam passes the intersection point twice, the question arise whether the feature size would be broader near the intersection point due to higher initial temperature at the intersection (due to first pass). Figure 5-6 shows that in experiments there is no broadening of feature size (line width) near the intersection point. Theoretical explanaition is that the laser induced temperature field is very local, e.g. on the order of 150 μm (e-folding diameter of the temperature profile) for a 30 mW laser beam, and lasts for a short period of time, on the order of a fraction of second for the above mentioned system (see Fig. 5-15). Thus, if the arms of the intersection are larger than 150 μm, there will be no boadening of feature size at the intersection (temperature has reduced to room temperature at the secong pass). It means that at the intersection point no broadening of feature size is expected. Also, in Figs. 5-5 and 5-9, which include cross-shaped patterns, no broadening of feature size (line width) near the intersection point is observed, as expected.

Effect of curvature was considered through examining theoretically calculated feature sizes (based on 498 K isotherms)[9] arcs of radii ranging from 30μm to 1 mm. In agreement with what we repoerted for the bigger laser beam, it was observed that feature sizes of largest arcs are slightly (~2%) larger than that of smallest arc. This expectation conform with Figs. 5-2, 5-8 and 5-9 where there was no measurable fieature size change on curvilinear features.

Summary and Conclusions

It is shown that DLP is capable of fabricating curvilnear features and various junction types. The effect of making certain geometrical patterns (crosses and angles) as well as the effect of heating trajectory's radius of curvature and heating spot's velocity on resulting surface temperature is considered. It is shown that 1 order of magnitude change in speed does not affect the feature sizes as much as a 30% change in laser power does change feature sizes. Thus, the main controlling parameter in DLP is power of the laser beam. No feature size broadening observed in making curvilinear and angular patterns; the induced surface temperature profiles and resulting features are symmetric with respect to centerline (unless large beam spots are used at very high curvature paths). In agreement with our experimental observations, within the range of parameters considered, there was theoretically no significant feature size change near vertex of angles, crosses and on curvilinear features. It is also shown that peak temperatures decrease at highly curved paths ($r/w_0<10$); this decrease is more pronounced as the scanning speed is increased.

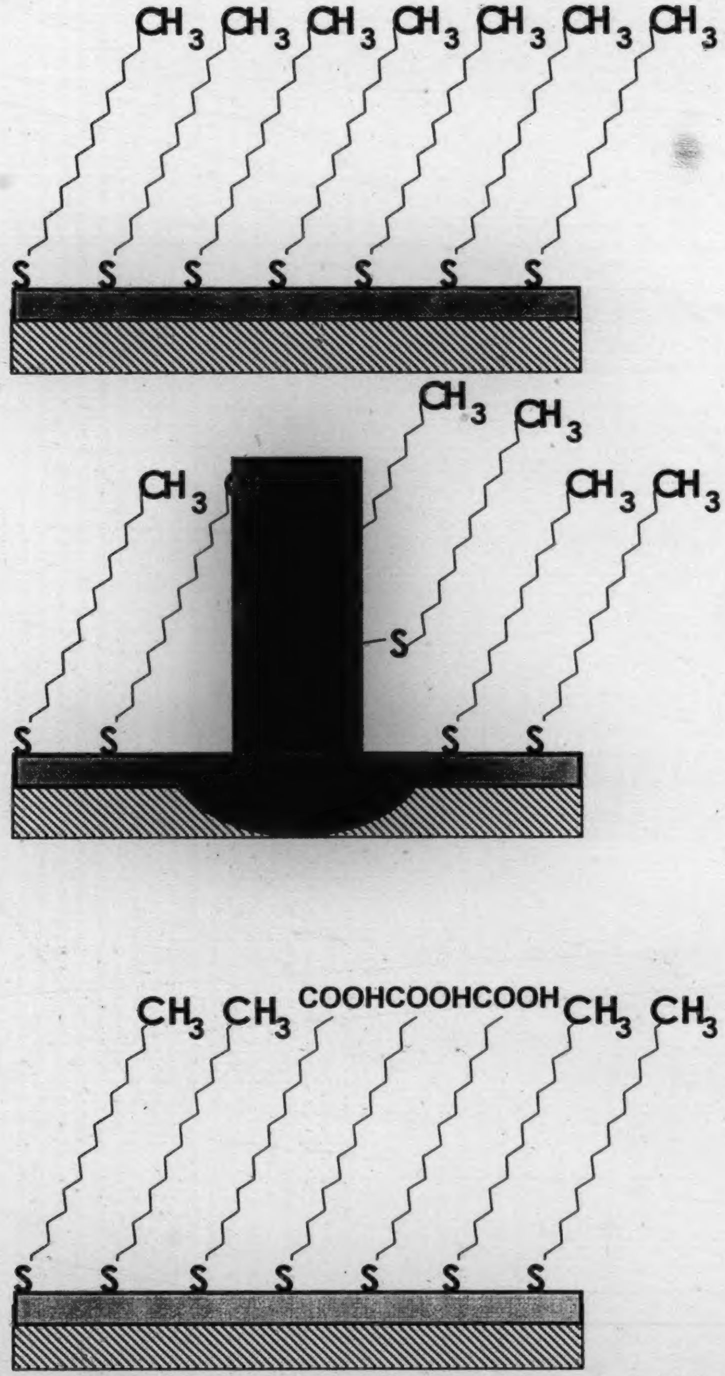
CH3 CH3 CH3 CH3 CH3 CH3 CH3
S S S S S S S
CH3 CH3
CH3 CH3 CH3 CH3
S S S S S
CH3 CH3 COOHCOOHCOOH CH3 CH3
S S S S S S S

Figure 5-1. Steps of direct laser patterning procedure: 1. Initial formation of a homogeneous SAM surface; 2. Subsequent removal of SAM at desired locations by laser heating; 3. Solution deposition of another SAM with different terminal group in the irradiated bare regions.

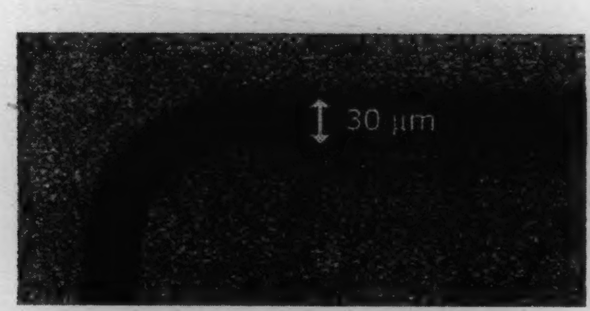

Figure 5-2. Liquid (dark region) delimited on a hydrophilic SAM (MHA) surrounded by a hydrophobic SAM (HDT) pictured under optical microscope. Such a pattern act as an open microchannel without physical walls.

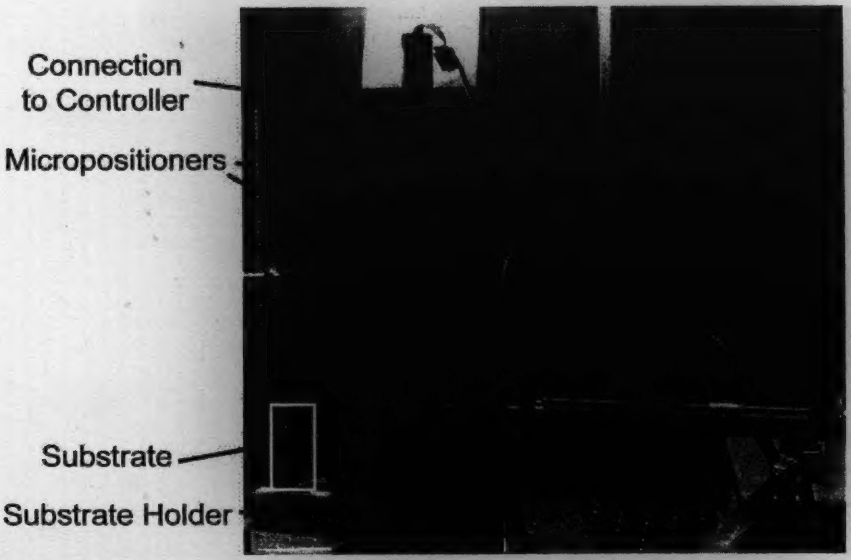
Connection to Controller
Micropositioners
Substrate
Substrate Holder

Figure 5-3. A substrate is placed in a sample holder, which is connected to two micropositioners that control the x and y movement of the substrate. The micropositioners are connected to a controller (not shown).

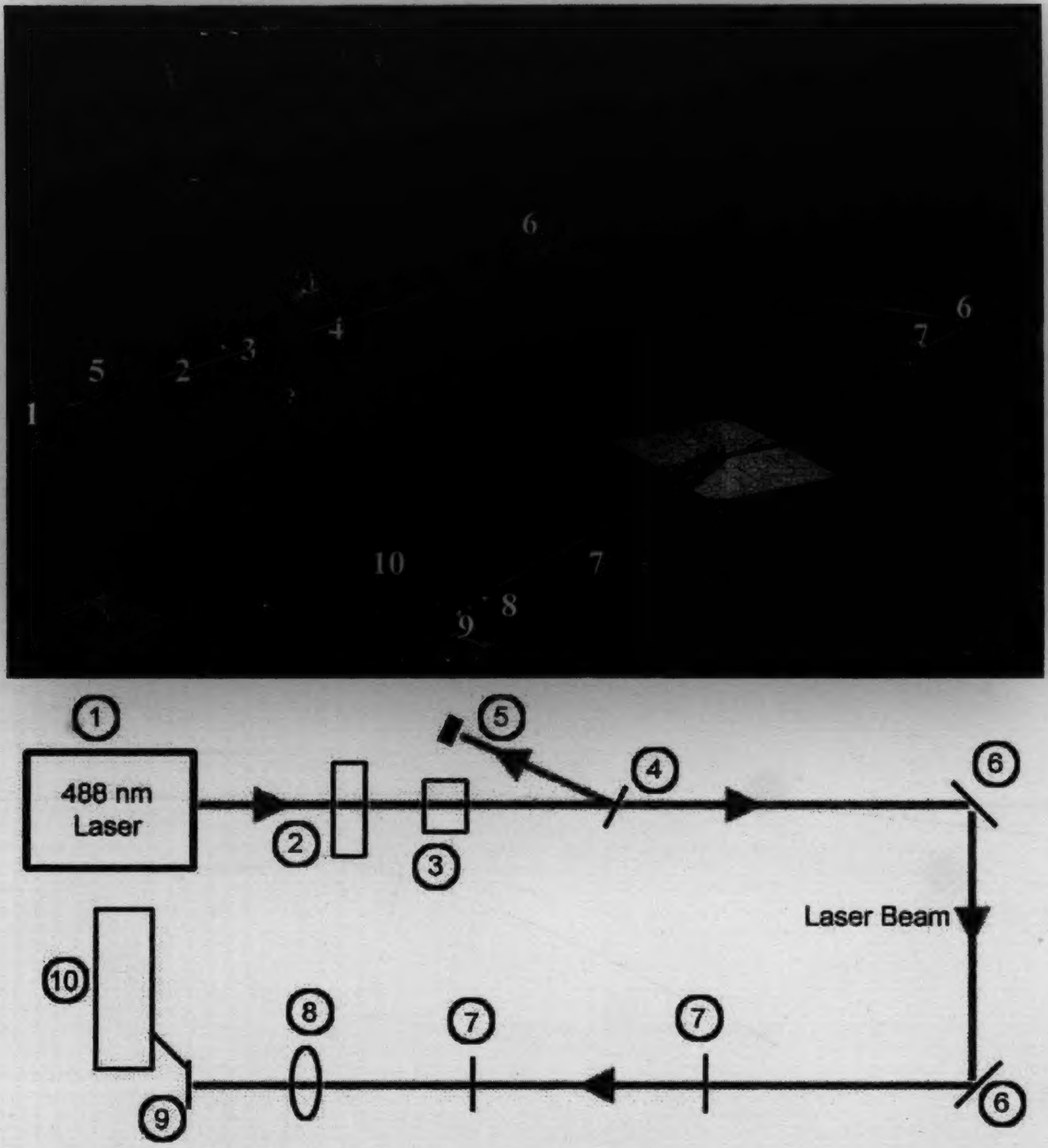
6
4
6
7
5
2
3
1
10
7
8
9
①
488 nm
Laser
⑤
④
⑥
②
③
Laser Beam
⑩
⑧
⑦
⑦
⑨
⑥

Figure 5-4. Actual image and schematic of optical setup for DLP system. An Argon ion laser (1) emits laser beam that goes through a Glan polarizer (2) and a half-wave plate (3). A wedge (4) splits ~4% of beam into power meter (5). The rest of the beam reflects off two mirrors (6) and goes through 2 apertures (7) for alignment purposes. The laser beam then is focused by a 10X microscope objective (8) on the sample (9). The motion of the substrate is controlled by the micropositioner setup (10).

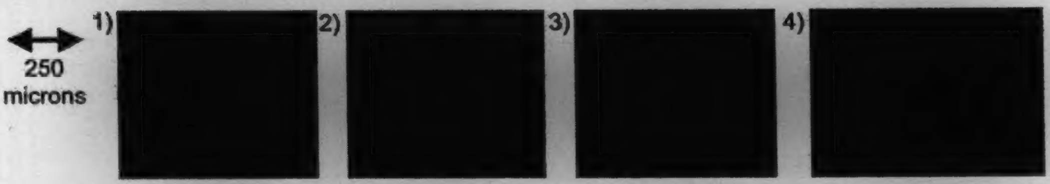

Figure 5-5. Light microscope images of features. Dark regions are liquid channels (Tridecane) on hydrophilic regions of the surface. All pictures were taken from part of the "U of A" pattern (see Fig. 5-9), which was made using 27 mW laser beam. The line width of features is ~30 microns.

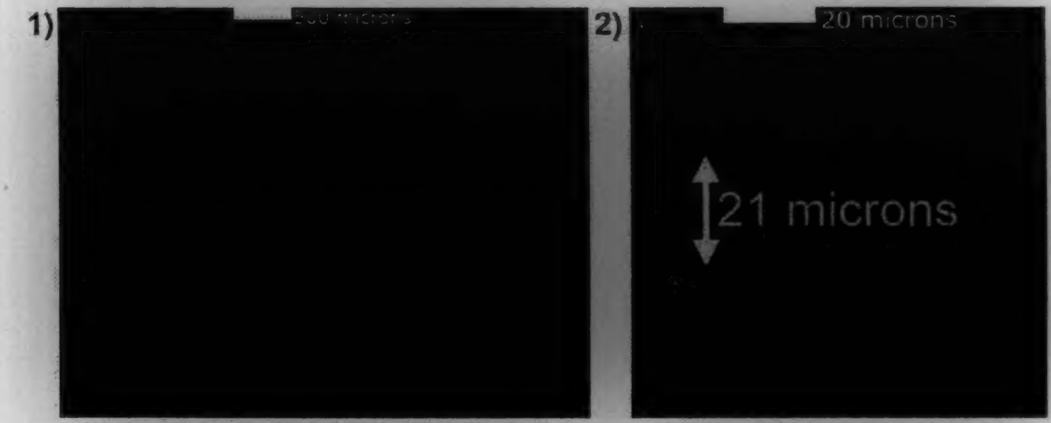
1)
2)
20 microns
21 microns

Figure 5-6. The SEM images of crosses and tee junctions. (1) shows crosses written with 18 mW laser beam on the left, and those written with 27 mW laser beam on the right. (2) a zoomed in image of the 18 mW cross.

10 microns
20 microns

Figure 5-7. The SEM image of a cusp angle written with a 18 mW laser beam.

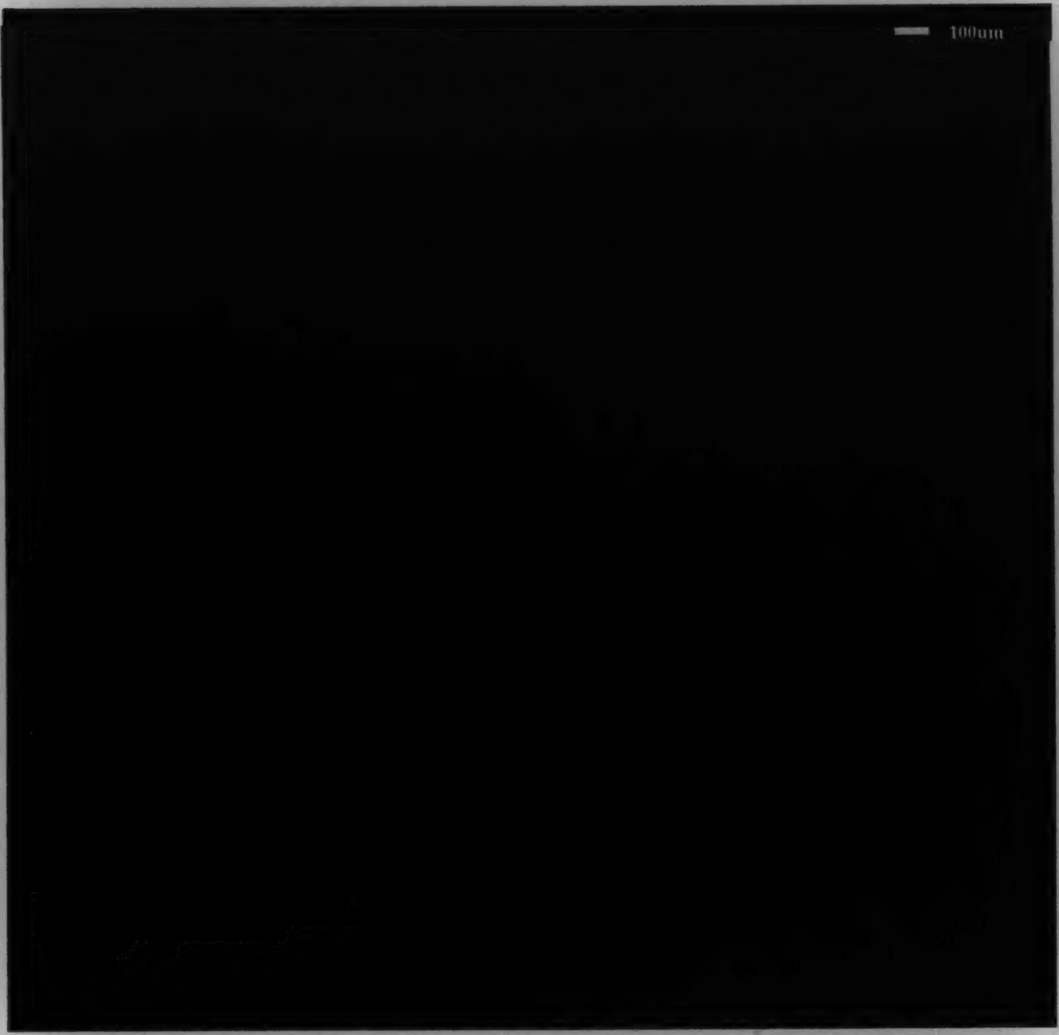

Figure 5-8. SEM images of circle features. The outer circle was written with a beam power of 18 mW, and the inner circle was written with a laser beam power of 27 mW.

Figure 5-9. SEM image of the letters "U of A" patterned as a hydrophilic MHA SAM on hydrophobic HAD SAM background.

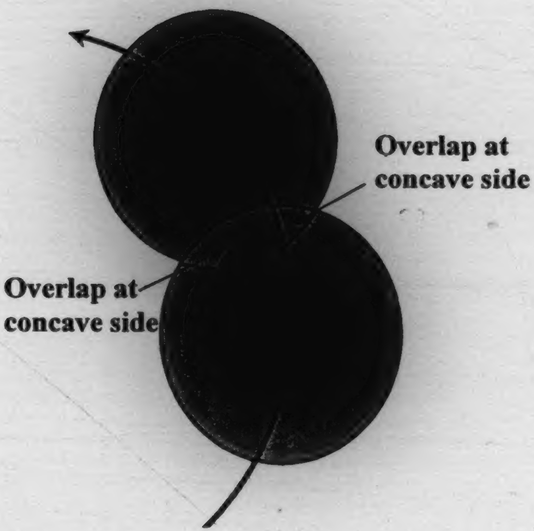
Overlap at concave side
Overlap at concave side

Figure 5-10. Heating on a circular curve. The overlap of hot regions at the concave side of the heating trajectory is more compared to the convex side of the heating trajectory.

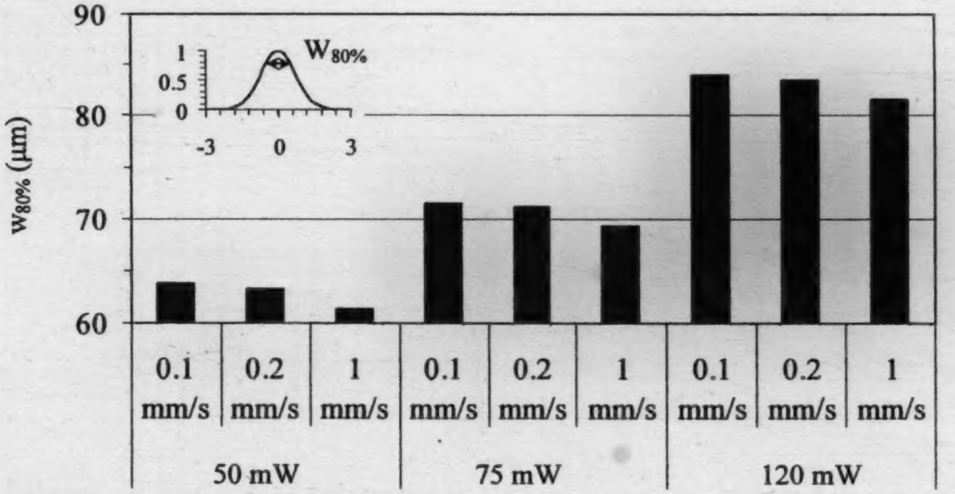

Figure 5-11 The width of the area that experience more than 80% of the maximum temperature ($w_{80\%}$) due to scanning laser beam moving on a circular-arc (radius 2 times the spot 2e-folding radius, $2w_0$). The figure shows the results after Laser beam had scanned a quarter of a circle. The inset on top left shows a dimensionless Gaussian profile to define $w_{80\%}$.

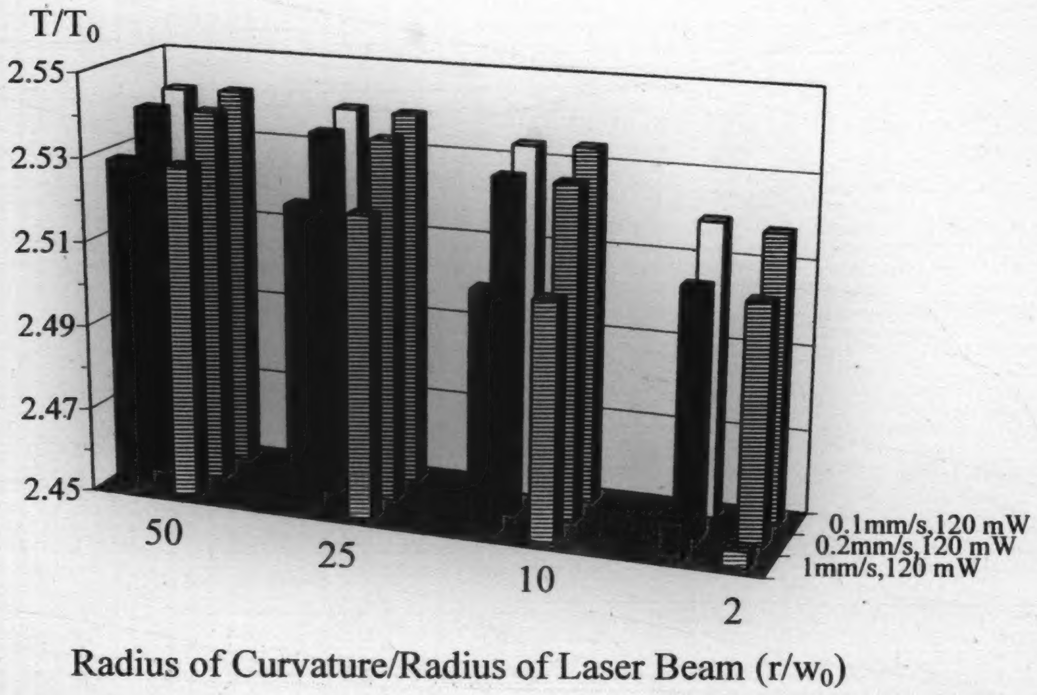

Figure 5-12. The effect of heating trajectory curvature, and speed of moving heat source on the maximum resulting temperature at the surface of the sample. The 120 mW Gaussian Laser beam scans a circular path (solid blocks) or its associated chord, representing heating along a straight line (hatched blocks). The figure shows the resulting peak temperature after spot had scanned a quarter of a circle for the case of the curvilinear trajectory.

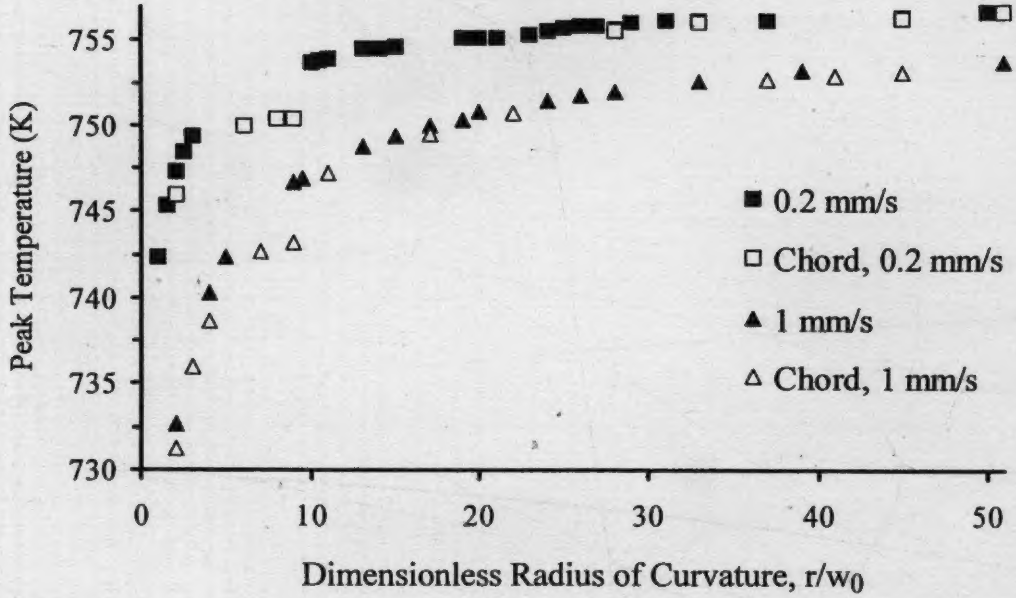

Figure 5-13. Maximum surface temperature versus radius of curvature of heating trajectory. The temperature fields are produced by scanning a 120 mW laser beam with a Gaussian spatial profile at constant speed on a circular-arc; the laser beam had scanned a quarter of circle.

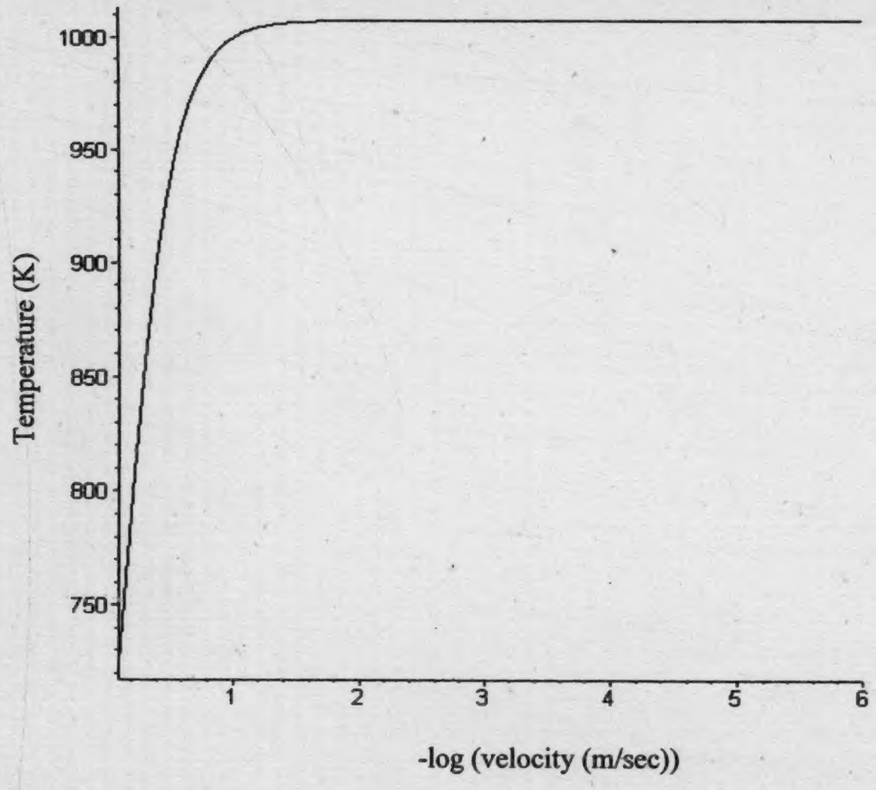

Figure 5-14. Variation of maximum surface temperature with scanning speed. The temperature fields are produced by scanning a 18 mW laser beam with a Gaussian spatial profile of 8 μm 2e-folding waist (focused using a 10X microscope objective) at constant speed of 0.2 mm/sec.

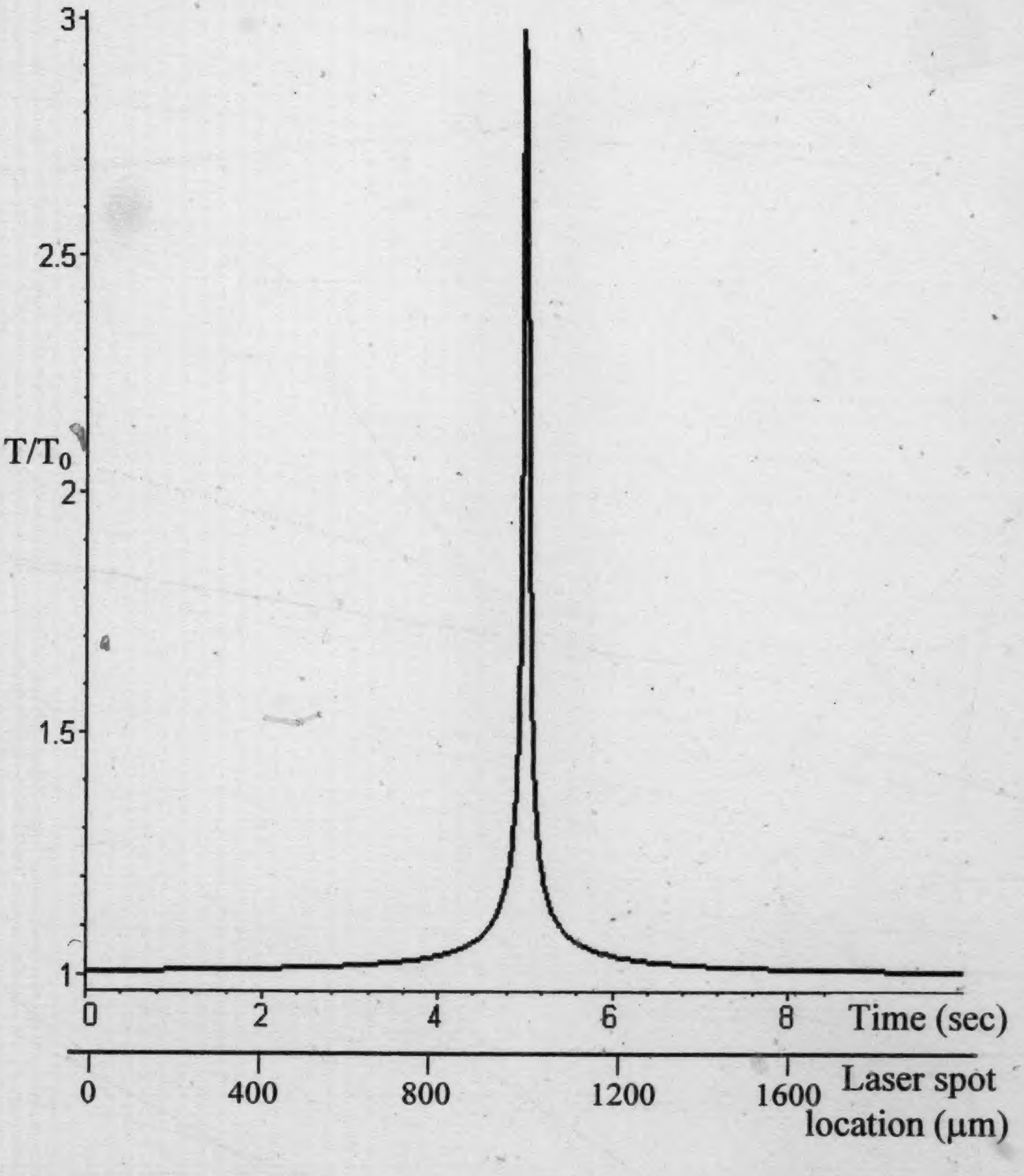

Figure 5-15. Temporal temperature profile induced at centerline of heating. It shows that the heating effect does not last for more than a fraction of second. The temperature field is produced by scanning a 30 mW Laser beam with a Gaussian spatial profile of 8 μm 2e-folding waist (focused using a 10X microscope objective) at constant speed of 0.2 mm/sec on a circular-arc.

References

(1) Dong, S.; Li, J. *Bioelctroch. Bioener.* **1997**, *42*, 7-13.

(2) Owen, J.I.; Niederhauser, T.L.; Wacaser, B.A.; Christenson, M.P.; Davis, R.C.; Linford, M.R. *LabChip* **2004**, *4*, 553-557.

(3) Schon, J.H.; Meng, H.; Bao, Z. *Nature* **2001**, *413*, 713-716.

(4) Nuzzo, R.G. *Proc. Natl. Acad. Sci.* **2001**, *98*, 4827-4829.

(5) Parviz, B.A.; Ryan, D.; Whitesides, G.M. *IEEE Trans. Adv. Packaging* **2003**, *26*, 233-241.

(6) Friebel, S.; Aizenberg, J.; Abad, S.; Wiltzius, P. *Appl. Phys. Lett.* **2000**, *77*, 2408-2410.

(7) Jackman, R.J.; Wilbur, J.L.; Whiteides, G.M. *Science* **1995**, *269*, 664-666.

(8) Piner, R.D.; Zhu, J.; Xu, F.; Hong, S.H.; Mirkin, C.A. *Science* **1999**, *283*, 661-663.

(9) Shadnam, M.R.; Kirkwood, S.E.; Fedosejevs, R.; Amirfazli, A. *Langmuir* **2004**, *20*, 2667-2676.

(10) Lahann, J.; Mitragotri, S.; Tran, T.; Kaido, H.; Sundaram, J.; Choi, I.S.; Hoffer, S.; Somorjai, G.A.; Langer, R. *Science* **2003**, *299*, 371-374.

(11) Campuzano, S.; Galvez, R.; Pedrero, M.; de Villena, F.J.M.; Pinarron, J.M. *Anal. Bioanal. Chem.* **2003**, *377*, 600-607.

(12) Chang, W.; Choi, M.; Kim, J.; Cho, S.; Whang, K. *Appl. Surf. Sci.* **2005**, *240*, 296-304.

(13) Banerjee, I.A.; Yu, L.; MacCuspie, R.I.; Matsui, H. *Nano Lett.* **2004**, *4*, 2437-2440.

(14) Lee, S.W.; Laibinis, P.E. *J. Am. Chem. Soc.* **2000**, *122*, 5395-5396.

(15) Chaudhury, M.K.; Whiesides, G.M. *Science*, **1992**, *256*, 1539-1541.

(16) Oh, S.K.; Nakagawa, M.; Ichimura, K. *J. Mat. Chem.*, **2002**, *12*, 2262-2269.

(17) Moody, J.E.; Hendel, R.H. *J. Appl. Phys.* **1982**, *53*, 4364-4371.

(18) Conde, J.C.; Lusquinos, F.; Gonzalez, P.; Leon, B.; Perez-Amor, M. *Vacuum* **2002**, *64* , 359-366.

(19) Shadnam, M.R.; Kirkwood, S.E.; Fedosejevs, R. and Amirfazli, A. *J. Phys. Chem. B* **2005**, *109*, 11996-12002.

(20) Klossika, J.J.; Gratzke, U.; Vicanek M.; Simmon, G. *Phys. Rev. B* **1996**, *54*, 10277.

(21) Tzou, D.Y. *Macro to Microscale Heat Transfer;* Tylor and Francis: Washington, 1997; pp. 279-280.

(22) Song, D.; Chen, G. *Appl. Phys. Lett.* **2004**, *84*, 687.

(23) Carslaw, H.S.; Jaeger, J.C. *Conduction of heat in solids*, Oxford University Press: London, 1959.

(24) Maple User Manual, 2004, Waterloo Maple Inc., Waterloo, Numerical Integration Section.

Chapter 6- Summary, Conclusions and Future Directions

Direct laser patterning (DLP) methodology for self-assembled monolayers (SAMs) on gold substrate was developed. In the DLP, a laser beam is scanned on surface and the resulting local high temperature triggers the endothermic SAM desorption to produce patterns. Experimental protocols were established and practical ranges of parameters (e.g. laser powers) were determined for the system studied. Subsequent studies were done to bring about an understanding of the underlying mechanisms of DLP to advance the fundamental knowledge and to predict the outcome of an experiment. It was observed how increase of laser power affects increase of feature sizes. The effect of the laser power, beam waist and temperature dependence of substrate conductivity on theoretical predictions was considered in a thermal model that originally relates feature sizes to temperature footprint of the laser beam. It was observed that the theoretical predictions for the patterning feature size is in good agreement with the experimental measurements and thus the thermal model could effectively be used to predict size of resulting patterns.

The pattern edges were examined using AES and SEM. It was observed that the edges are sharp at higher powers and somewhat blunt at lower powers. Kinetics of SAM desorption, represented by Eyring equation, was coupled with the temperature history each point experiences (using thermal model) into an original thermokinetics model to explain the observations. The thermokinetics model can theoretically predict surface coverage of SAM after laser irradiation. The developed thermo-kinetic model consistent with SEM images revealed that there exist a band of partial desorption near edges. The

SEM images and the thermokinetics model also showed that at very low powers, only partial desorption of SAM occurs. Surface coverage of SAMs at each point was coupled with knowledge of contact angle on mixed SAMs and it was shown that wetting of resulting patterned surfaces are predictable; wetting of patterned surfaces is important for applications of patterns as open channel microfluidics.

For the above mentioned thermo-kinetic model and for investigation of thermal stability of SAM, kinetics of SAM desorption into air was studied. Kinetics of SAM desorption into gaseous media was not considered in literature up to that point. It was shown that the desorption follows two consecutive first order regimes: a fast followed by a slow regime. The activation energies for both regimes were calculated and it was shown that desorption into air is slower than desorption into liquid media (probably, as theoretically expected, due to lack of strong solvation interactions). The results of the kinetic study were used in the thermokinetics model of laser desorption. Results of the fast desorption regime were relevant to laser desorption process as surface experiences high temperature in fraction of a second in the laser desorption process. Using the thermokinetics model, it was shown that slower SAM desorption in air makes the feature sizes shrink by ~20% in the laser patterning working range (compared to laser desorption in solvent).

Since curvilinear features are of interest in applications (e.g. microfluidics), laser patterning along curvilinear patterns were investigated. Curvilinear patterns and various junction types were successfully made using the direct laser patterning (DLP) methodology. Effect of heating trajectory's radius of curvature and heating spot's velocity on resulting surface temperature map is considered. It is shown that one order of magnitude change in speed does not affect the feature sizes as much as a 30% change in laser power does change feature sizes. Thus, the main controlling parameter in DLP is power of the laser beam. No feature size broadening is expected in making curvilinear patterns; the induced surface temperature profiles and resulting features are for the most part symmetric with respect to centerline (unless large beam spots are used at very high curvature paths). It was also shown that peak temperatures decrease at highly curved paths ($r/w_0<10$); this decrease is more pronounced as the scanning speed is increased. The results of these investigations have provided a firm experimental and theoretical basis for DLP.

Future Directions and Recommendations

In future, this project can be pursued in various directions. Immediate extensions of the project, at the methodology level, are attempts to make gradients of surface properties using DLP and making large patterns in a single pass process using elliptical laser beams. At fundamental level, relevant physical chemistry of SAMs can be pursued as sorption and exchange kinetics and energetics of various (fuctionalized) alkanethiols is not yet completely investigated. Also, effects of structural properties of the molecules, e.g. chain length, functional groups, can be related to energetics of sorption and exchange. At the application level, one can try to move liquid drops on resulting hydrophilic channels and come up with surface mass transfer strategies, which will take DLP closer to microfluidic applications.

In longer term, further advancement of capabilities of "Direct Laser Patterning" (DLP) of SAMs is one of possible directions. Capabilities of DLP can be expanded for SAM patterning on various substrates such as silicon and (potentially) polymers. The other possibility is patterning on gold-coated silicon wafers and polymers such as Polymethyl methacrylate (PMMA).

Applications of SAMs in making patterned surfaces, in general, and the DLP, in particular, are relatively new to the field and hence have many unsolved problems and areas for improvements. For example, not many wavelengths have been examined for DLP. Only 488 nm line of Argon laser and femtosecond pulses of Ti-Sapphire laser at 800 nm have been examined for DLP; and it was shown that the laser-SAM interaction is different in the two experiments [1,2]. Exploring capabilities of DLP, using laser systems with shorter wavelengths (i.e. <488 nm) and pulses lengths shorter and longer than femtosecond worth investigation. How such lasers interact with SAMs and which is the best for patterning for a specific application will be main questions to answer. The next step in each new interaction regime would be understanding of how the feature sizes in DLP are scaled with laser power, number of pulses, laser beam size (which can be examined through going in and out of focus) and scanning velocity (e.g. 0.01-100 mm/sec); the resulting patterned surfaces can be characterized and feature sizes can be measured using Scanning Electron Microscopy (SEM), Auger Electron Spectroscopy (AES) and Secondary Ion Mass Spectroscopy (SIMS). Finding the thresholds for changing different interaction regimes is also a question of interest.

Finding resonant energy transfer frequencies through absorption spectroscopy of SAMs will also be helpful. Finding such frequencies will enable direct and more efficient energy transfer to particular chemical bonds of interest and results in finer features in DLP. In this way, one can think of cutting the molecules at places other than the gold-sulfur bonds. This will open new horizons for chemical manipulation of SAMs and their functionalization, which have profound potential for modification of surface properties.

In further expansion of DLP applications, one can focus on tailoring fuctionalized patterned surfaces that are useful for biological applications. Fuctionalized patterned surfaces for neuronal and axonal guidance, development of bone cell growth matrices and immobilization of cells and compatible enzymes next to each other can be attempted.

For those biomedical purposes where an immediate exposure to biological species in solvent is needed or the surface cannot be exposed to gaseous media, extending the scope of DLP to patterning in solution media might be of interest.

References

(1) Kirkwood, S.E., Shadnam, M.R., Amirfazli, A., Fedosejevs, R. *J. Phys.*, in press.

(2) Shadnam, M.R., Kirkwood, S.E., Fedosejevs, R., Amirfazli, A. *Langmuir,* **2004**, *20*, 2667-2676.

Appendix 1- Details of Experimental Methods

Cleaning of Glassware

Glassware used for preparation of solutions and those used to keep samples were cleaned based on the following procedure. The glassware were cleaned using normal washing methods using soap-water solution until there was no visible dirt on or in them. They were thoroughly rinsed with water. Then, the glassware was kept under concentrated Chromosulfuric acid solution, which is mixture of concentrated Sulfuric acid and Chromium oxide (CrO_3), over night. The day after the glassware were removed from solution and rinsed with deionized water followed by 200 proof ethanol and let dry in oven or under a heat lamp.

Sample Preparation

Samples were made through sequential sputtering. Titanium was used as adhesion layer to bind a gold film on a Soda Lime glass. The rate of deposition for gold and titanium was determined to be 1.3 Å/s and 0.3 Å/s, respectively. The final thicknesses were finally checked using both contact and optical profilometery after etching.

Calibration of Laser Power

A Gentech power meter measured incident power on surface of sample. The measurement was done well out of focus after the lens or microscope objective (not to damage the sensor). Additionally, a semi-conductor Thorlab power meter measured sum of both back and front reflections from the wedge (see Fig. A1-1). Laser power was set at a fixed level. After 10 min (to let possible fluctuations of laser power settle) readings from both sensors were recorded. The laser was then blocked and zero reading of the Gentech power meter was recorded after 1 min (to let the Gen tech power meter settle). The same procedure was used for other laser power levels of interest. A chart of sensor recordings were created as result (see Table A1-1 as a sample). Having the resulting chart in hand one can determine incident laser powers from Thorlab readings.

Focusing of Laser Beam

The microscope objective that the laser beam went through had to be focused properly such that the focused beam would impact the substrate. To focus the beam properly, the optical focus setup shown in Fig. A1-2 was used. To focus the microscope objective, white light was used to light up the surface of the substrate. This light passed through the microscope objective in the opposite direction to laser beam and then reflected off of two mirrors into a CCD camera. The CCD camera was connected to a to visualize the beam. The microscope objective was moved by a micropositioner until an image of the substrate in the CCD was seen and was in focus. The microscope objective was then moved 0.132 mm towards the substrate by the micropositioner to compensate for divergence of the laser beam. Once this was finished, the microscope objective was in focus and DLP was begun.

Wherever lens was used to focus the beam, position of focal plane was calculated and manually adjusted. Since the Rayleigh range is large, spot size is not as sensitive to positioning of the lens compared to that in case of focusing by microscope objective. For verification, the position lens was changed about the calculated position (in and out of focus) during the scanning. Numbers reported as feature size were the minimum along the line, which are essentially relevant to true focus. However, not much sensitivity was observed in terms of feature size in those experiments.

Table A1-1. Power calibration chart

Power Measured on the Thorlab Powermeter (mW)	Zero Voltage of the Gentech Powermeter (mV)	Measured Voltage of the Gentech Powermeter (mV)
9.09 ± 0.02	0.02	12.63
1.05± 0.02	-0.07	1.30

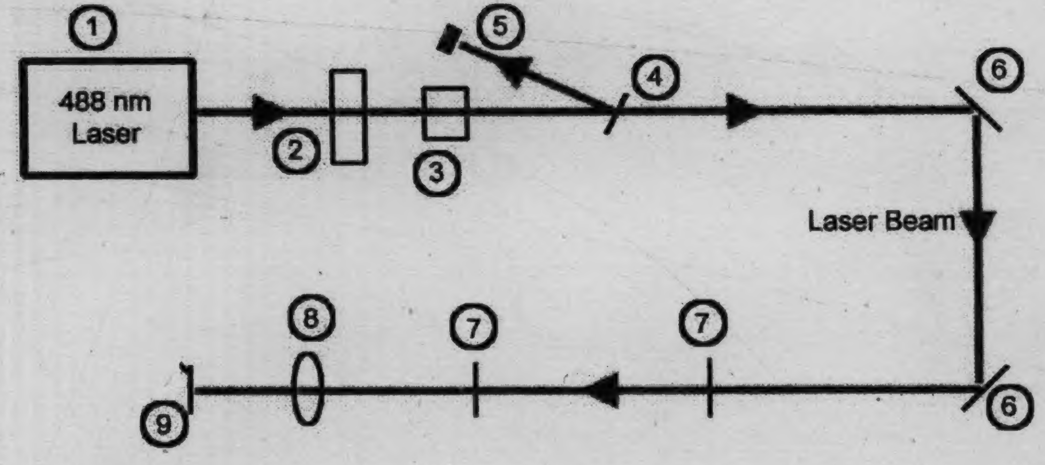

Figure A1-1. Optical setup for calibration of laser power for DLP. The 488 nm laser (1) emits a laser beam that goes through a Glan polarizer (2) and then another polarizer (3). The beam then hits a wedge (4) that partially splits the beam into the Thorlab power meter (5). The rest of the beam travels to and reflects off two mirrors (6) and then through 2 apertures (7). The laser then gets focused (8) and hits the Gentech power meter (9).

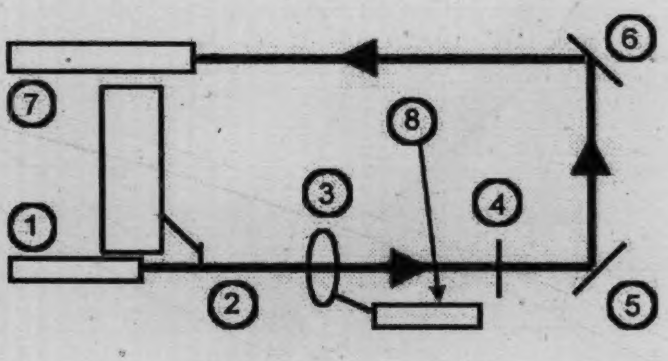

Figure A1-2. Focus setup for DLP system. White light from fiberoptics (1) light up the edge of the substrate (2). This light went through the microscope objective (3) in the backwards direction, then went through an aperture (4), reflected off of a flip-up mirror (5), reflected off another mirror (5) into a CCD camera (7). A micropositioner (8) then moved the microscope objective up to the point the image from the CCD camera was in focus. The micropositioner is finally used to adjust position of objective for divergence compensation.

Appendix 2- Details of the Thermo-kinetic Model

This appendix provides the original computer code used for calculation of coverage of the original Self Assembled Monolayer (SAM) after laser irradiation. The code is based on formulas presented in Chapter 3 and couples heat transfer equation and kinetics of SAM desorption represented by Eyring equation. The code was written for Maple software version 8. Units for all parameters are in System International (SI).

Maple Code

```
> v:=200e-6;w010:=2.274e-6;a:=.44;
```

$$v := 0.000200$$

$$w010 := 0.000002274$$

$$a := 0.44$$

```
> z:=0;
```

$$z := 0$$

```
> d:=3.3e-7;
```

$$d := 3.3\ 10^{-7}$$

```
> k0:=.6692910958;k1:=0.000680231222125081;
```

$$k0 := 0.6692910958$$

$$k1 := 0.000680231222125081$$

```
> kt0:=.872;
```

$$kt0 := 0.872$$

```
> T0:=298;
```

$$T0 := 298$$

```
> r:=w0/2;
```

$$r := \frac{w0}{2}$$

```
> X:=x/r;Y:=y/r;Z:=z/r;V:=v/r;sigma:=r^2/4/d;
```

$$X := \frac{2\,x}{w0}$$

$$Y := \frac{2\,y}{w0}$$

$$Z := 0$$

$$V := \frac{0.000400}{w0}$$

$$\sigma := 1.893939394\,10^{5}\,w0^{2}$$

```
> f:=exp(-
((X+V*sigma*u^2)^2/(u^2+1)+Y^2/(u^2+1)+Z^2/u^2))/(u^2+1);
```

$$f := \frac{e^{\left(-\frac{\left(\frac{2\,x}{w0}+75.75757576\,w0\,u^{2}\right)^{2}}{u^{2}+1}-\frac{4\,y^{2}}{w0^{2}\,(u^{2}+1)}\right)}}{u^{2}+1}$$

```
> theta:=p/r*a/Pi^(3/2)/kt0*int(f,u=0..infinity);
```

$$\theta := \frac{1.009174312\,p}{w0\,\pi^{(3/2)}}\int_{0}^{\infty}\frac{e^{\left(-\frac{\left(\frac{2\,x}{w0}+75.75757576\,w0\,u^{2}\right)^{2}}{u^{2}+1}-\frac{4\,y^{2}}{w0^{2}\,(u^{2}+1)}\right)}}{u^{2}+1}\,du$$

```
> plot(subs(p=.1,y=yy*1e-6,w0=w010,theta),yy=-100..100);
```

```
> EapR:=30.5*4184/8.315;
```

$$EapR := 15347.20385$$

```
> temp:=simplify(subs(p=.030,w0=12.5*w010,1/2/k1*(-
2*k0+2*(k0^2+2*k1*theta*kt0+k1^2*T0^2+2*k1*k0*T0)^(1/2))));
```

$$temp = -983.9170475 + 0.01470088357\,\mathrm{sqrt}\Bigg(7.603839999\;10^{9} + 2.269160431\;10^{9} \int_{0.}^{Float(\infty)} \frac{1}{u^{2}+1.}\exp\bigg(-\frac{1}{u^{2}+1.}(1.000000000\;10^{-15}\,(4.950613759\;10^{24}\,x^{2} + 3.030303030\;10^{17}\,x\,u^{2} + 4.637170713\;10^{9}\,u^{4} + 4.950613760\;10^{24}\,y^{2}))\bigg)\,du\Bigg)$$

```
> kbph:=1.380e-23/6.626e-34;
```

$$kbph := 2.082704497\;10^{10}$$

```
> for coun from 0.0 to 1.4 by 0.1 do
> evalf(coun*10),evalf(exp(-kbph*int(subs(y=coun*1e-
5,x=v*tim,temp)*exp(-EapR/subs(y=coun*1e-
5,x=v*tim,temp)),tim=-150..150)));
> od;
```

Appendix 3- Curvilinear Calculations

This appendix provides the original computer code used for calculation of surface temperature profile after laser irradiation on a circular trajectory. The code is based on formulas presented in Chapter 5. The code was written for Maple software version 8. Units for all parameters are in System International (SI).

Maple Code

Definition of linear dependence of conductivity with temperature

```
> k:=k0+k1*t;
```

$$k := k0 + k1\,t$$

```
> solve(theta=int(k/kts,t=Ts..T),T);
```

$$\frac{1}{2\,k1}\left(-2\,k0 + 2\sqrt{k0^2 + 2\,k1\,\theta\,kts + k1^2\,Ts^2 + 2\,k1\,k0\,Ts}\right),\ \frac{-2\,k0 - 2\sqrt{k0^2 + 2\,k1\,\theta\,kts + k1^2\,Ts^2 + 2\,k1\,k0\,Ts}}{2\,k1}$$

```
> k1:=0.000680231222125081;
```

$$k1 := 0.000680231222125081$$

```
> k0:=solve(subs(t=298,k)=.872,k0);
```

$$k0 := 0.6692910958$$

```
> kts:=.872;Ts:=298;
```

$$kts := 0.872$$

$$Ts := 298$$

Definition of heating path

```
> X(t):=R*cos(w*tp); Y(t):=R*sin(w*tp);
```

$$X(t) := R\cos(w\,tp)$$

$$Y(t) := R\sin(w\,tp)$$

```
> Q:=P*exp(-((xp-X(t))^2+(yp-
Y(t))^2)/2/r^2)/2/Pi/r^2*Dirac(zp);
```

$$Q := \frac{1}{2}\frac{1}{\pi r^2}\left(P\, e^{\left(-\frac{1}{2}\frac{(xp - R\cos(w\,tp))^2 + (yp - R\sin(w\,tp))^2}{r^2}\right)}\, \mathit{Dirac}(zp)\right)$$

Derivation of the integrand

```
> inte:=Q/Cp*exp(-((x-xp)^2+(y-yp)^2+(z-zp)^2)/4/d/(t-
tp))/4/(Pi*d*(t-tp))^(3/2);
```

$$inte := \frac{1}{8}\frac{1}{\pi r^2\, Cp\, (\pi\, d\, (t - tp))^{(3/2)}}\left(P\, e^{\left(-\frac{1}{2}\frac{(xp - R\cos(w\,tp))^2 + (yp - R\sin(w\,tp))^2}{r^2}\right)}\, \mathit{Dirac}(zp)\, e^{\left(-\frac{(x - xp)^2 + (y - yp)^2 + (z - zp)^2}{4\, d\, (t - tp)}\right)}\right)$$

Spatial integrations

```
> int(int(inte, zp=-infinity..infinity), yp=-
infinity..infinity);
```

$$\mathit{PIECEWISE}\Bigg(\qquad \Bigg|$$

$$\frac{1}{4}\frac{1}{\pi^2 r^2 \mathit{Cp}\, d\,(t-tp)\sqrt{d\,(t-tp)}\sqrt{\frac{2\,d\,t-2\,d\,tp+r^2}{r^2\,d\,(t-tp)}}}$$

$$\Bigg(\exp\Bigg($$

$$-\frac{1}{4}\frac{1}{d\,r^2\,(t-tp)\,(2\,d\,t-2\,d\,tp+r^2)}\Big($$

$$-8\,R\cos(w\,tp)\,xp\,d^2\,t^2-4\,x\,xp\,r^2\,d\,t+x^2\,r^4$$

$$-4\,R\sin(w\,tp)\,d\,t\,y\,r^2+4\,x\,xp\,r^2\,d\,tp+xp^2\,r^4$$

$$+z^2\,r^4-8\,xp^2\,d^2\,t\,tp+4\,xp^2\,d\,r^2\,t-4\,xp^2\,d\,r^2\,tp$$

$$+2\,x^2\,r^2\,d\,t-2\,x^2\,r^2\,d\,tp+2\,y^2\,r^2\,d\,t-2\,y^2\,r^2\,d\,tp$$

$$+2\,z^2\,r^2\,d\,t-2\,z^2\,r^2\,d\,tp+4\,xp^2\,d^2\,t^2$$

$$+4\,xp^2\,d^2\,tp^2-2\,x\,xp\,r^4+4\,R^2\cos(w\,tp)^2\,d^2\,t^2$$

$$+4\,R^2\cos(w\,tp)^2\,d^2\,tp^2$$

$$+16\,R\cos(w\,tp)\,xp\,d^2\,t\,tp$$

$$-8\,R\cos(w\,tp)\,xp\,d^2\,tp^2-4\,R\cos(w\,tp)\,xp\,d\,r^2\,t$$

$$+4\,R\cos(w\,tp)\,xp\,d\,r^2\,tp-8\,R^2\cos(w\,tp)^2\,d^2\,t\,tp$$

$$+2\,R^2\cos(w\,tp)^2\,d\,r^2\,t-2\,R^2\cos(w\,tp)^2\,d\,r^2\,tp$$

$$+2\,R^2\sin(w\,tp)^2\,d\,r^2\,t-2\,R^2\sin(w\,tp)^2\,d\,r^2\,tp$$

$$\left.\left.\left.+4\,R\sin(w\,tp)\,d\,tp\,y\,r^2\right)\right)P\right),$$

$$\left.csgn\left(\frac{1}{2\,r^2}+\frac{1}{4\,d\,(t-tp)}\right)=1\right],$$

$$\left.[\infty,\ otherwise]\right)$$

```
> int(1/4*exp(-1/4*(-8*R*cos(w*tp)*xp*d^2*t^2-
4*x*xp*r^2*d*t+x^2*r^4-
4*R*sin(w*tp)*d*t*y*r^2+4*x*xp*r^2*d*tp+xp^2*r^4+z^2*r^4-
8*xp^2*d^2*t*tp+4*xp^2*d*r^2*t-
4*xp^2*d*r^2*tp+2*x^2*r^2*d*t-2*x^2*r^2*d*tp+2*y^2*r^2*d*t-
2*y^2*r^2*d*tp+2*z^2*r^2*d*t-
2*z^2*r^2*d*tp+4*xp^2*d^2*t^2+4*xp^2*d^2*tp^2-
2*x*xp*r^4+4*R^2*cos(w*tp)^2*d^2*t^2+4*R^2*cos(w*tp)^2*d^2*
tp^2+16*R*cos(w*tp)*xp*d^2*t*tp-8*R*cos(w*tp)*xp*d^2*tp^2-
4*R*cos(w*tp)*xp*d*r^2*t+4*R*cos(w*tp)*xp*d*r^2*tp-
8*R^2*cos(w*tp)^2*d^2*t*tp+2*R^2*cos(w*tp)^2*d*r^2*t-
2*R^2*cos(w*tp)^2*d*r^2*tp+2*R^2*sin(w*tp)^2*d*r^2*t-
2*R^2*sin(w*tp)^2*d*r^2*tp+4*R*sin(w*tp)*d*tp*y*r^2)/d/r^2/
(t-tp)/(2*d*t-2*d*tp+r^2))*P/Pi^2/r^2/Cp/d/(t-tp)/(d*(t-
tp))^(1/2)/((2*d*t-2*d*tp+r^2)/r^2/d/(t-tp))^(1/2),xp=-
infinity..infinity);
```

$$PIECEWISE\Bigg($$

$$\Bigg[$$

$$\frac{1}{2}\frac{1}{\pi^{(3/2)}\,Cp\,\sqrt{d\,(t-tp)}\,(2\,d\,t-2\,d\,tp+r^{2})}\Bigg(\exp$$

$$\Bigg($$

$$-\frac{1}{4}\frac{1}{d\,(t-tp)\,(2\,d\,t-2\,d\,tp+r^{2})}(z^{2}\,r^{2}$$

$$-4\,R\sin(w\,tp)\,d\,t\,y-2\,x^{2}\,d\,tp+2\,x^{2}\,d\,t$$

$$+4\,R\sin(w\,tp)\,d\,tp\,y-2\,R^{2}\sin(w\,tp)^{2}\,d\,tp$$

$$+2\,R^{2}\cos(w\,tp)^{2}\,d\,t+2\,y^{2}\,d\,t$$

$$-2\,R^{2}\cos(w\,tp)^{2}\,d\,tp+2\,R^{2}\sin(w\,tp)^{2}\,d\,t$$

$$+4\,x\,R\cos(w\,tp)\,tp\,d-2\,y^{2}\,d\,tp-2\,z^{2}\,d\,tp$$

$$-4\,x\,R\cos(w\,tp)\,t\,d+2\,z^{2}\,d\,t)\Bigg)\,P\Bigg),$$

$$csgn\Bigg($$

$$\frac{r^2}{4\,d\,(t-tp)\,(2\,d\,t-2\,d\,tp+r^2)}$$

$$+\frac{d\,t^2}{r^2\,(t-tp)\,(2\,d\,t-2\,d\,tp+r^2)}$$

$$-\frac{2\,d\,t\,tp}{r^2\,(t-tp)\,(2\,d\,t-2\,d\,tp+r^2)}$$

$$+\frac{t}{(t-tp)\,(2\,d\,t-2\,d\,tp+r^2)}$$

$$-\frac{tp}{(t-tp)\,(2\,d\,t-2\,d\,tp+r^2)}$$

$$\left.+\frac{d\,tp^2}{r^2\,(t-tp)\,(2\,d\,t-2\,d\,tp+r^2)}\right) = 1\Bigg],$$

$$\left.[\infty,\ otherwise]\right)$$

Calculation of temperature before Kirchhoff transformation

```
> lintemp:=int(1/2*exp(-1/4*(z^2*r^2-4*R*sin(w*tp)*d*t*y-
2*x^2*d*tp+2*x^2*d*t+4*R*sin(w*tp)*d*tp*y-
2*R^2*sin(w*tp)^2*d*tp+2*R^2*cos(w*tp)^2*d*t+2*y^2*d*t-
2*R^2*cos(w*tp)^2*d*tp+2*R^2*sin(w*tp)^2*d*t+4*x*R*cos(w*tp
)*tp*d-2*y^2*d*tp-2*z^2*d*tp-
4*x*R*cos(w*tp)*t*d+2*z^2*d*t)/d/(t-tp)/(2*d*t-
2*d*tp+r^2))*P/Pi^(3/2)/Cp/(d*(t-tp))^(1/2)/(2*d*t-
2*d*tp+r^2),tp=0..t);
```

$$lintemp := \int_0^{t} \frac{1}{2} \frac{1}{\pi^{(3/2)}\, Cp \sqrt{d\,(t - tp)}\,(2\,d\,t - 2\,d\,tp + r^2)}$$

$$\left(\exp\left(\right.\right.$$

$$-\frac{1}{4} \frac{1}{d\,(t - tp)\,(2\,d\,t - 2\,d\,tp + r^2)} (z^2\, r^2$$

$$- 4\,R\sin(w\,tp)\,d\,t\,y - 2\,x^2\,d\,tp + 2\,x^2\,d\,t$$

$$+ 4\,R\sin(w\,tp)\,d\,tp\,y - 2\,R^2\sin(w\,tp)^2\,d\,tp$$

$$+ 2\,R^2\cos(w\,tp)^2\,d\,t + 2\,y^2\,d\,t$$

$$- 2\,R^2\cos(w\,tp)^2\,d\,tp + 2\,R^2\sin(w\,tp)^2\,d\,t$$

$$+ 4\,x\,R\cos(w\,tp)\,tp\,d - 2\,y^2\,d\,tp - 2\,z^2\,d\,tp$$

$$\left.\left. - 4\,x\,R\cos(w\,tp)\,t\,d + 2\,z^2\,d\,t) \right) P \right) dtp$$

```
> Cp:=kts/d;
```

$$Cp := \frac{0.872}{d}$$

Numerical values

```
> w010:=8e-6;a:=.44;d:=3.3e-7;z:=0;P:=p*a;t:=R*Pi/v/2;
```

$$w010 := 0.000008$$

$$a := 0.44$$

$$d := 3.3\; 10^{-7}$$

$$z := 0$$

$$P := 0.44\,p$$

$$t := \frac{R\,\pi}{2\,\nu}$$

```
> lintemp;
```

$$\int_{0}^{\frac{0.00008880000000}{\pi\,\nu}} \left(8.325688075\;10^{-8}\,\exp\left(\right.\right.$$

$$-\left(7.575757575\;10^{5} \left(\right.\right.$$

$$-5.8608\;10^{-11}\cos\left(\frac{2.000000000}{\pi}\right) tp\,x + 6.6\;10^{-7}\,y^{2}\,tp$$

$$-\frac{5.860800000\;10^{-11}\,x^{2}}{\pi\,\nu}$$

$$+1.3010976\;10^{-15}\sin\left(\frac{2.000000000}{\pi}\right)^{2} tp$$

$$+1.3010976\;10^{-15}\cos\left(\frac{2.000000000}{\pi}\right)^{2} tp$$

$$-5.8608\;10^{-11}\sin\left(\frac{2.000000000}{\pi}\right) tp\,y$$

$$- \frac{1.155374669\ 10^{-19} \cos\left(\frac{2.000000000}{\pi}\right)^{2}}{\pi\,\nu}$$

$$- \frac{1.155374669\ 10^{-19} \sin\left(\frac{2.000000000}{\pi}\right)^{2}}{\pi\,\nu}$$

$$- \frac{5.860800000\ 10^{-11}\ y^{2}}{\pi\,\nu} + 6.6\ 10^{-7}\ x^{2}\ tp$$

$$+ \frac{5.204390400\ 10^{-15} \sin\left(\frac{2.000000000}{\pi}\right) y}{\pi\,\nu}$$

$$\left. + \frac{5.204390400\ 10^{-15} \cos\left(\frac{2.000000000}{\pi}\right) x}{\pi\,\nu} \right)\right) \Bigg/$$

$$\left(\left(tp - \frac{0.00008880000000}{\pi\,\nu} \right) \left(\right.\right.$$

$$\left.\left.\left. \frac{5.860800000\ 10^{-11}}{\pi\,\nu} - 6.6\ 10^{-7}\ tp + r^{2} \right)\right)\right) p \Bigg) \Bigg/$$

$$\left(\pi^{(3/2)}\sqrt{-3.3\ 10^{-7}\ tp+\frac{2.930400000\ 10^{-11}}{\pi\,\nu}}\right.$$

$$\left.\left(\frac{5.860800000\ 10^{-11}}{\pi\,\nu}-6.6\ 10^{-7}\ tp+r^{2}\right)\right)\right)\,dtp$$

```
> evalf(lintemp);
```

$$\int_{0.}^{30.}\left(1.794223633\ 10^{-9}\exp\left(\right.\right.$$

$$-\frac{1}{(tp-30.)\,(0.00001980049284-6.6\ 10^{-7}\ tp)}$$

$$(7.575757575\ 10^{5}\ (-1.980000000\ 10^{-9}$$

$$-1.089443012\ 10^{-8}\ tp\ x+6.6\ 10^{-7}\ y^{2}\ tp$$

$$-0.00001980\ x^{2}+6.600000000\ 10^{-11}\ tp$$

$$-7.453280648\ 10^{-9}\ tp\ y-0.00001980\ y^{2}$$

$$+6.6\ 10^{-7}\ x^{2}\ tp+2.235984194\ 10^{-7}\ y$$

$$\left.\left.+3.268329035\ 10^{-7}\ x))\right)\right)\Bigg/\left(\right.$$

$$\sqrt{-3.3\ 10^{-7}\ tp+0.00000990\ (0.00001980049284}$$

$$\left.\overline{-6.6\ 10^{-7}\ tp)}\right)\,dtp$$

Derivation of temperature after the Kirchhoff transformation

```
> nonlintemp:=1/2/k1*(-
2*k0+2*(k0^2+2*k1*lintemp*kts+k1^2*Ts^2+2*k1*k0*Ts)^(1/2));
```

$nonlintemp := -983.9170475$

$$+1470.088357\,\mathrm{sqrt}\Bigg($$

$$0.7603839999$$

$$+0.001186323251 \int_0^{\frac{R\pi}{2\nu}} \Bigg(8.325688075\ 10^{-8}\,\mathrm{exp}\Bigg|$$

$$-\Bigg(7.575757575\ 10^{5} \Bigg($$

$$-\frac{6.600000000\ 10^{-7}\,R^2 \sin(w\,tp)\,\pi\,y}{\nu} - 6.6\ 10^{-7}\,x^2\,tp$$

$$+\frac{3.300000000\ 10^{-7}\,x^2\,R\,\pi}{\nu}$$

$$+0.00000132\,R \sin(w\,tp)\,tp\,y$$

$$-6.6\ 10^{-7}\,R^2 \sin(w\,tp)^2\,tp$$

$$+\frac{3.300000000\ 10^{-7}\,R^3 \cos(w\,tp)^2\,\pi}{\nu}$$

$$+\frac{3.300000000\ 10^{-7}\ y^{2}\ R\,\pi}{\nu}$$

$$-\ 6.6\ 10^{-7}\ R^{2}\cos(w\ tp)^{2}\ tp$$

$$+\frac{3.300000000\ 10^{-7}\ R^{3}\sin(w\ tp)^{2}\ \pi}{\nu}$$

$$+\ 0.00000132\ x\ R\cos(w\ tp)\ tp\ -\ 6.6\ 10^{-7}\ y^{2}\ tp$$

$$-\frac{6.600000000\ 10^{-7}\ x\ R^{2}\cos(w\ tp)\ \pi}{\nu}\ \big)\big)\Big/\Big(\Big($$

$$\frac{R\,\pi}{2\,\nu}-tp\Big)\Big(\frac{3.300000000\ 10^{-7}\ R\,\pi}{\nu}-6.6\ 10^{-7}\ tp$$

$$+\,r^{2}\big)\big)\big)\ p\ \Big)\Big/\Big(\ \pi^{(3/2)}$$

$$\sqrt{\frac{1.650000000\ 10^{-7}\ R\,\pi}{\nu}-3.3\ 10^{-7}\ tp}$$

$$\Big(\frac{3.300000000\ 10^{-7}\ R\,\pi}{\nu}-6.6\ 10^{-7}\ tp+r^{2}\Big)\Big)\ dtp$$

$$\Bigg)$$

```
> r:=w010;
                              r := 0.000008
> evalf(subs(y=2,x=v*t,nonlintemp));
                               297.9999995
> plot3d(nonlintemp,x=-.6e-3..0.6e-3,y=-.6e-3..0.6e-3);
```

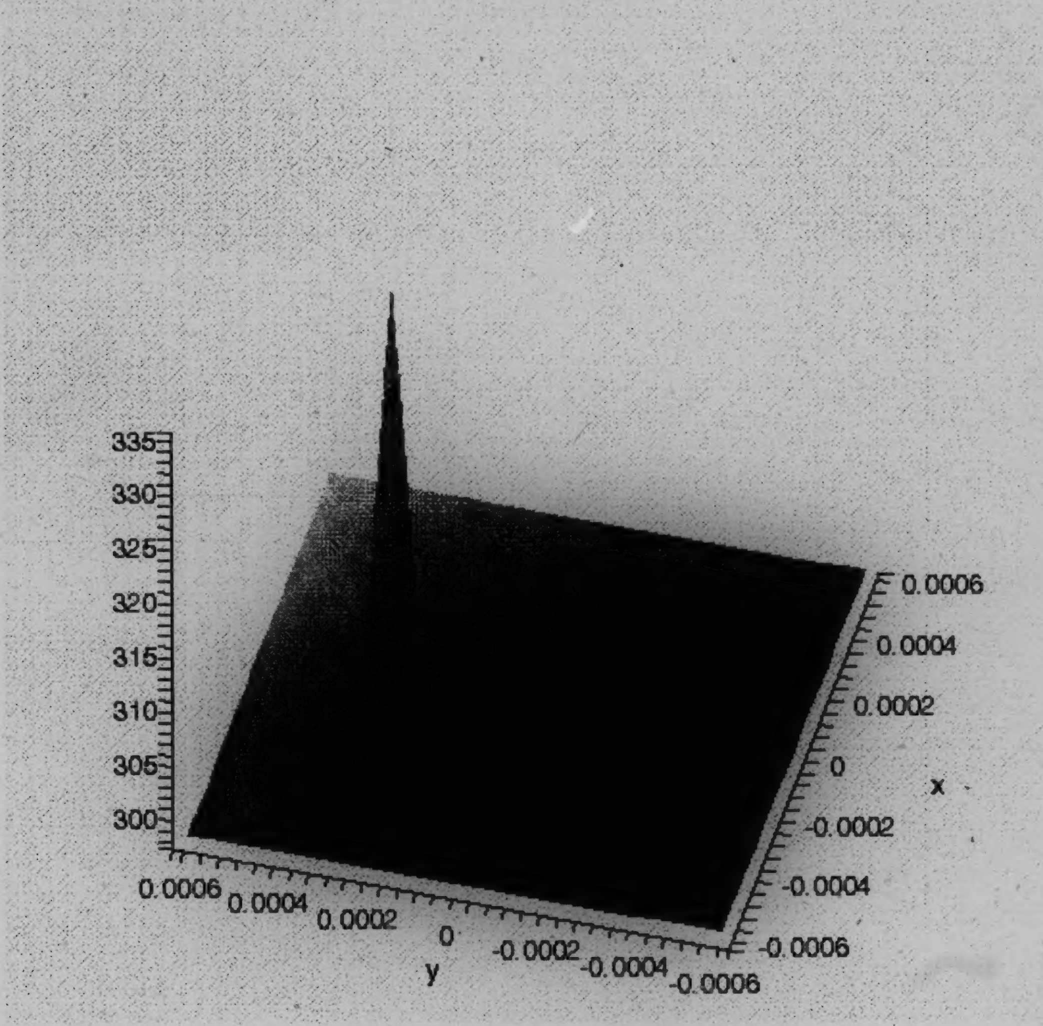

Appendix 4- Other Experimental Results

Figure A4-1 shows a number of microfluidics that has been created using Direct Laser Pattering (DLP). The liquid used in the figures are Tridecane. For such preparation of images a liquid with low surface tension and low vapor pressure is needed.

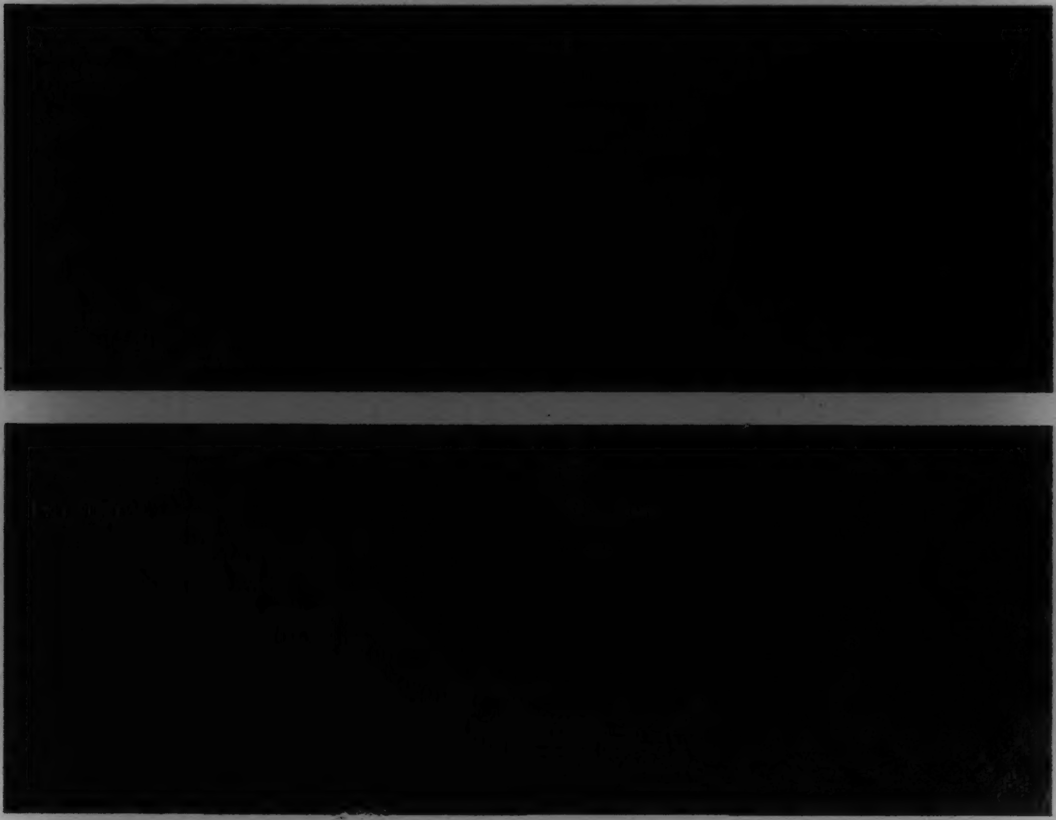

Fig. A4-1 (Continued on the next page)

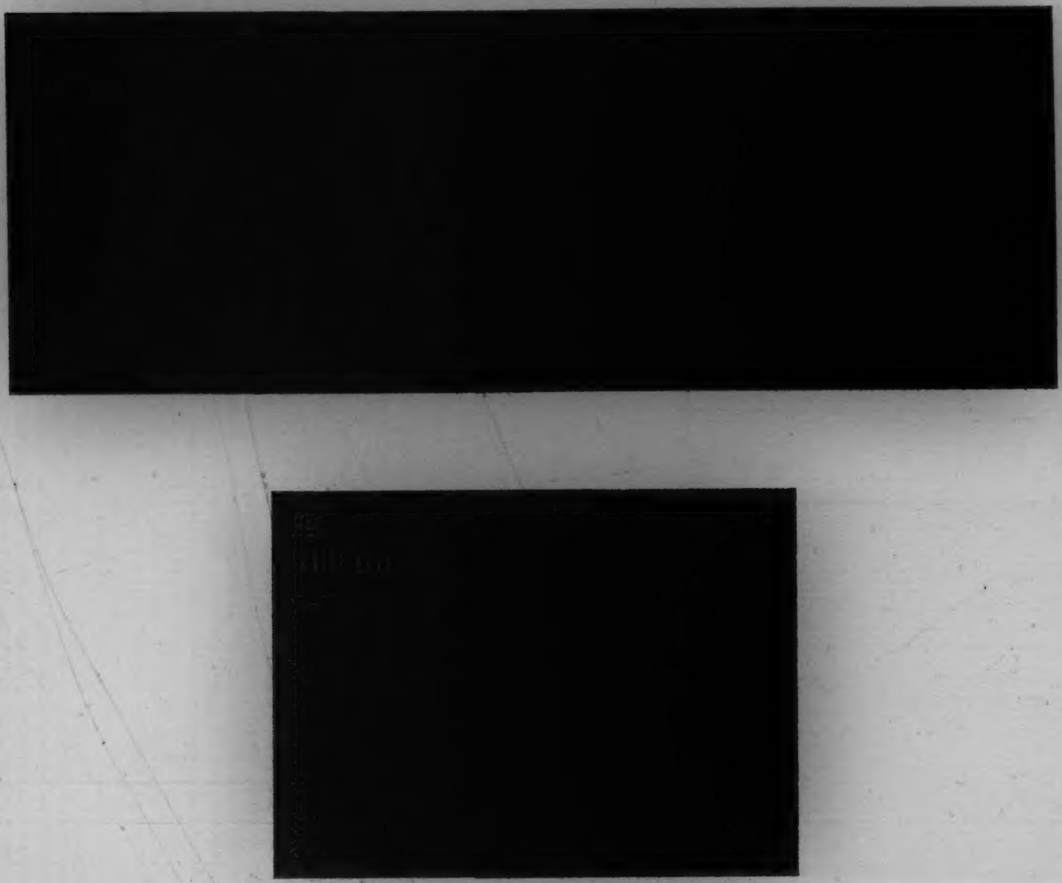

Figure A4-1. Liquid confinement on a number of patterned surfaces created with DLP under optical microscope: (a) is a cross, (b-f) show various angles and (g) show a circular arc.

Appendix 5- Kinetic Plots

Semilogarithmic plots of desorption data show that the reaction follows a first order kinetics (see Fig. A5-1). In first order kinetics the rate of desorption is proportional to the surface concentration of SAMs. Figure A5-1 shows that data from higher temperature experiment follow a linear trend more closely than those at lower temperatures as judged by the correlation coefficient. The linear correlation coefficient is higher at higher temperatures. We also examined possibility of a second order desorption, i.e. the rate of desorption is proportional to square of surface concentration of SAMs. Linearity of graph of inverse of products versus time is characteristic of a second order reaction. Therefore, graphs of inverse of surface coverage versus time were constructed (see Fig. A5-2). The linearity at higher temperatures, i.e. 653 K and 513 K, is poor, but it improves at lower temperatures, i.e. 433 K and 383 K. Considering Fig. A5-1 and Fig. A5-2, one can conclude that SAM desorption in air is better represented by a first order reaction compared to a second order kinetics.

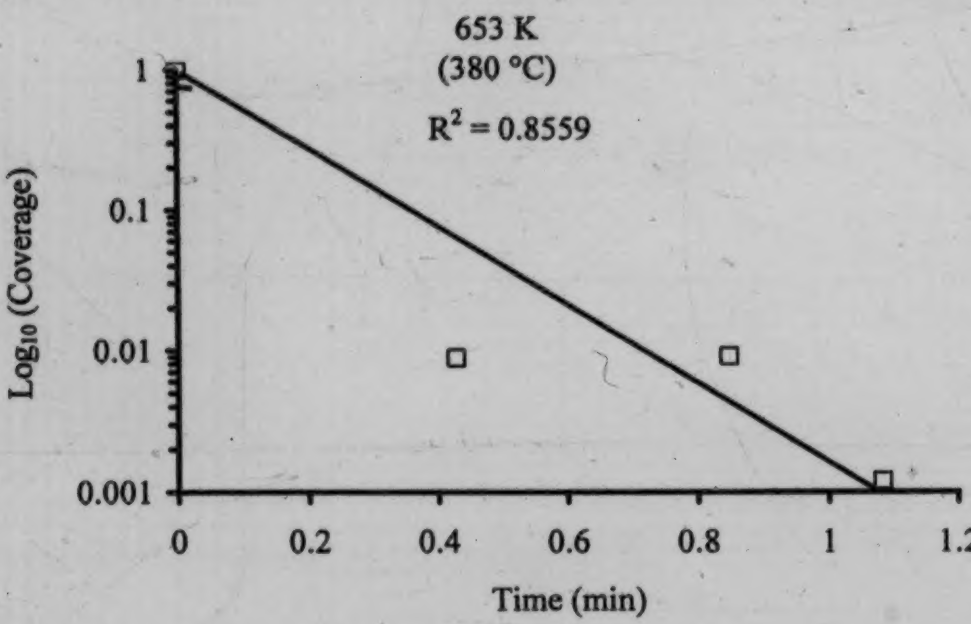

(a)

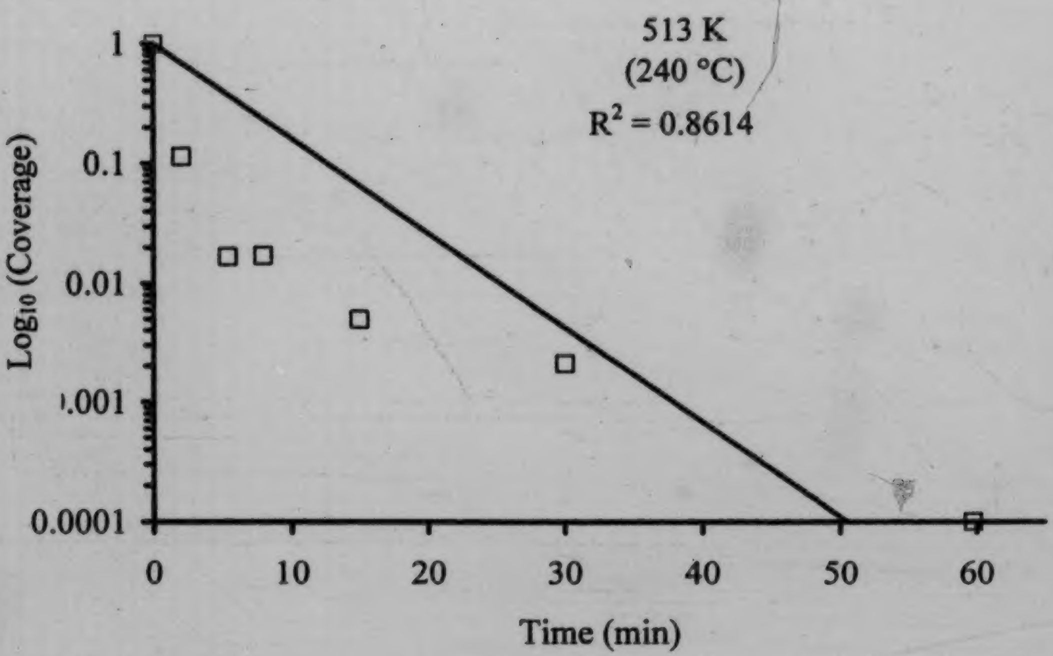

(b)

Fig. A5-1 (Continued in next page)

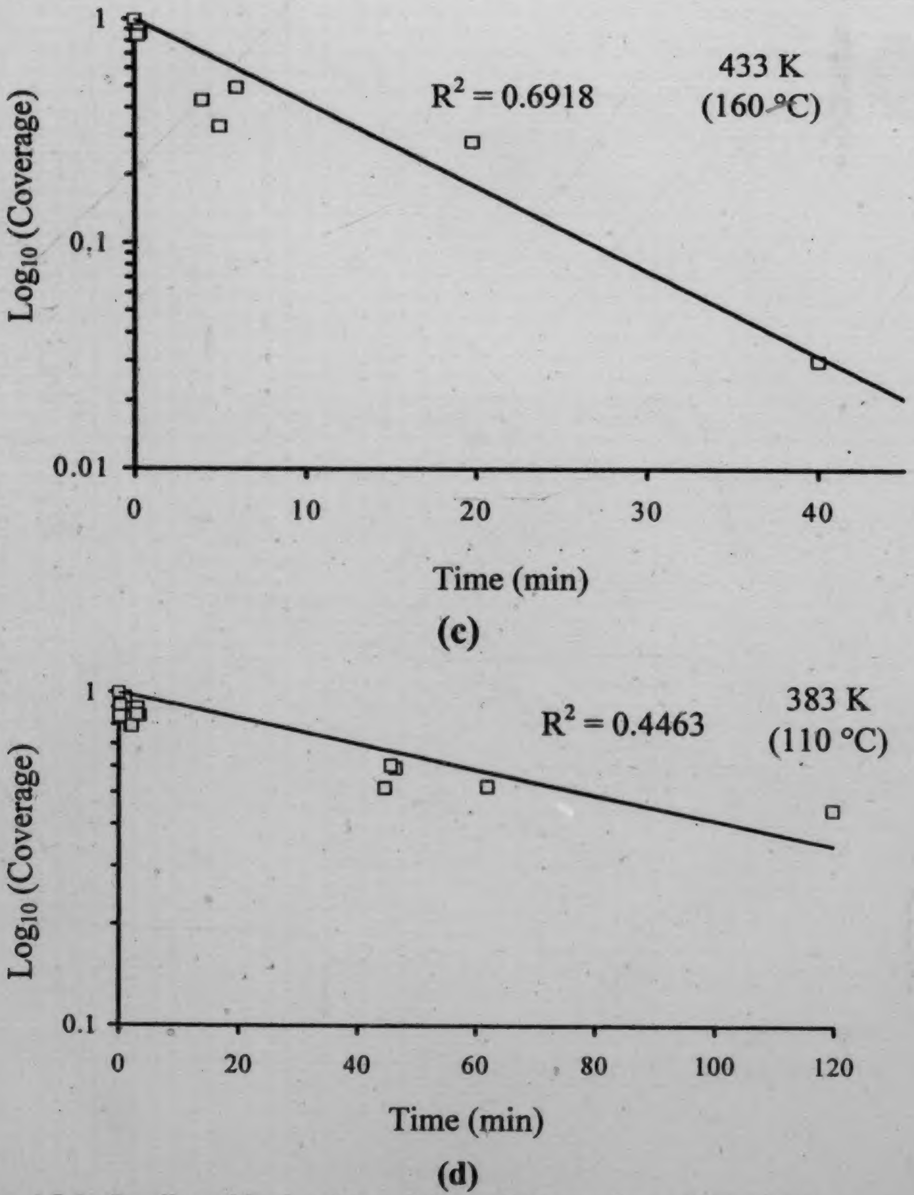

Figure A5-1. Semilogarithmic plots of thermal desorption of HDT SAMs from gold surface at (a) 653 K (=380 °C), (b) 513 K (=240 °C), (c) 433 K (=160 °C) and (d) 383 K (=110 °C). The lines are best-fitted curves.

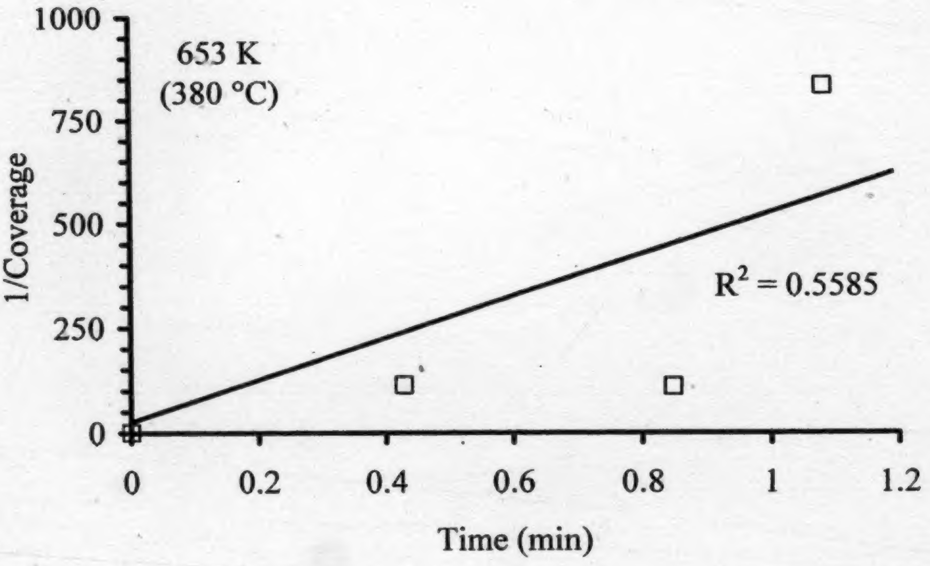

(a)

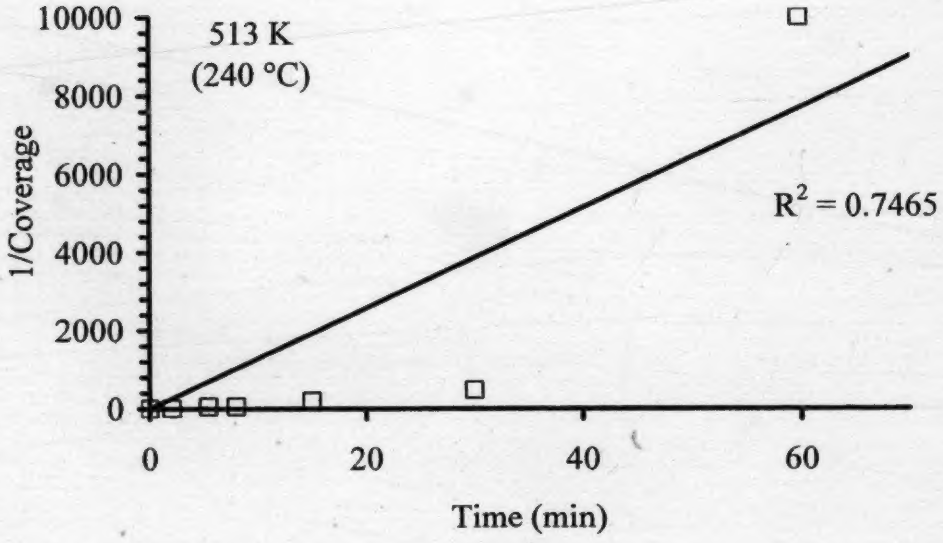

(b)

Fig. A5-2 (Continued in next page)

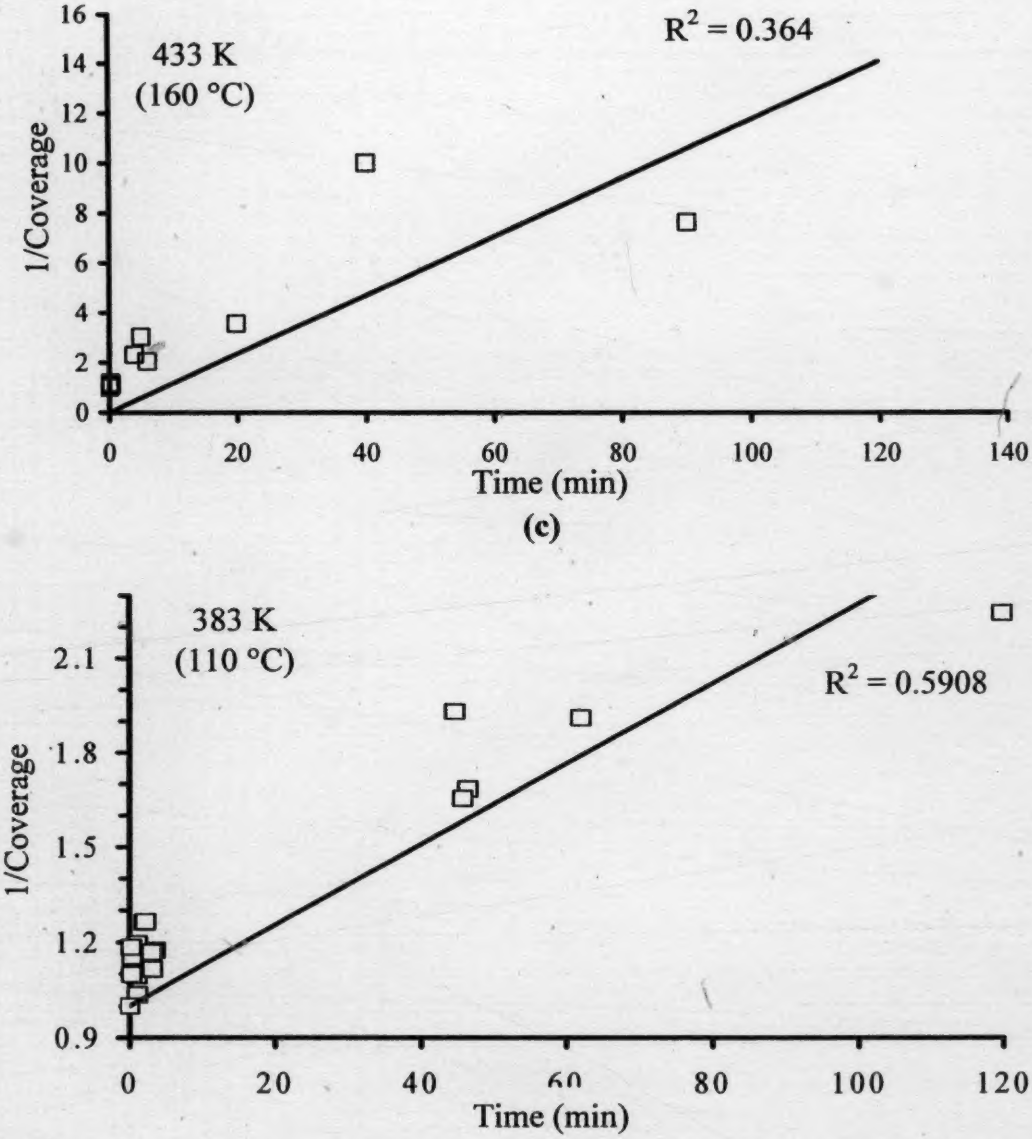

(c)

(d)

Figure A5-2. Thermal desorption profile of HDT SAMs from gold surface as inverse of coverage versus time at (a) 653 K (=380 °C), (b) 513 K (=240 °C), (c) 433 K (=160 °C) and (d) 383 K (=110 °C). The lines are best-fitted curves.